UNIVERSITY OF ZAGREB
FACULTY OF MECHANICAL ENGINEERING
AND NAVAL ARCHITECTURE

BACHELOR THESIS

Mihael Plut

0035177184

Zagreb, 2013

UNIVERSITY OF ZAGREB
FACULTY OF MECHANICAL ENGINEERING
AND NAVAL ARCHITECTURE

BACHELOR THESIS

Mentor:

Doc. dr. sc. Hrvoje Kozmar, dipl. ing.

Student:

Mihael Plut

Zagreb, 2013

Declaration

The author wishes to declare that, except for commonly understood ideas, or where specific reference is made to the work of other authors, the contents of this science report is my own original work and include nothing which is the outcome of work done in collaboration. The work has not been previously submitted, in part or in whole, to any other institutions for any research or any other investigation, and the results correspond to reality.

Mihael Plut

SVEUČILIŠTE U ZAGREBU
FAKULTET STROJARSTVA I BRODOGRADNJE
Središnje povjerenstvo za završne i diplomske ispite
Povjerenstvo za završne ispite studija strojarstva za smjerove:
procesno-energetski, konstrukcijski, brodostrojarski i inženjersko modeliranje i računalne simulacije

Sveučilište u Zagrebu Fakultet strojarstva i brodogradnje	
Datum 06 -09- 2013	Prilog
Klasa: 602 - 04/13 - 6/4	
Ur.broj: 15-1703-13-290	

ZAVRŠNI ZADATAK

Student: **Mihael PLUT** Mat. br.: 0035177184

Naslov: **Experiments on flow and turbulence in the climatic wind tunnel**

Opis zadatka:

Climatic wind tunnel is a specially designed facility that allows for experimental simulations of the thermally stratified atmospheric boundary layer flows including precipitation, as well as their effects on engineering structures. As the new climatic wind tunnel of the Centre of Excellence in Telc, Czech Republic, is currently in the final construction phase, prior to testing on particular structures it is required to investigate flow and turbulence characteristics in an empty wind-tunnel test section, i.e. without structural experimental models.

In this work it is necessary to provide:
1) Full design details of the new climatic wind tunnel of the Centre of Excellence in Telc, Czech Republic,
2) Technical details of the measuring equipment to be used for flow and turbulence characterization in an empty wind-tunnel test section,
3) Experimental setup,
4) Results and discussion,
5) Conclusions.

It is advised to list references used in this work, as well as to acknowledge help and support possibly received during the course of this study.

Zadatak zadan: 15. travnja 2013.

Rok predaje rada: Rujan 2013.

Zadatak zadao: Doc. dr. sc. Hrvoje Kozmar

Predsjednik Povjerenstva: Prof. dr. sc. Igor Balen

Referada za diplomske i završne ispite

Obrazac DS - 3A/PDS - 3A

Acknowledgements

This thesis would not have been possible without the support of many people. First of all I would like to thank my mentor Prof. Hrvoje Kozmar for suggesting this thesis in the first place and for being there for me all the way through to completing of this thesis.

I would like to thank to Prof. Stanislav Pospíšil for giving me the opportunity to write my thesis at the Centre of Excellence Telč and especially for his efforts in assuring an easy transition in the Czech Republic. I wish to express my gratitude to my supervisor Prof. Sergey Kuznetsov who was abundantly helpful and offered invaluable support and guidance at carrying out the experiments and by writing of the report. Also I would like to thank Dr. Radomil Král and, Mr. Arsenii Trush whose knowledge and assistance this study was of immense help.

Great thanks goes to the technicians at the CET for making the experiments possible with their craftsmanship and to all of the employees at the CET for understanding and helping me leap over the language barrier.

Special thanks also to all my graduate friends, for making it much easier to do all my academic duties from a distance. Not forgetting, I would like to thank to my best friends who have always been there.

Last but definitely not least, I wish to express my love and gratitude to my beloved family; for their understanding and endless love, through the duration of my studies.

Contents

List of symbols 8

Table of figures 10

List of tables 13

Abstract 14

Sažetak 15

1. INTRODUCTION 16

2. CHARACTERISTICS OF THE ATMOSPHERIC WIND 18

2.1. Mean velocity characteristics 23

2.2. Turbulence characteristics 27

2.2.1. Turbulence intensity 28

2.2.3. Integral length scale of turbulence 28

2.2.4 Power spectral density of velocity fluctuations 29

2.2.5 Turbulent Reynolds stress 32

3. WIND-TUNNEL DESIGN 34

3.1. Aerodynamic section 36

3.2. Climatic section 40

3.3. Fan 42

3.4. Heat exchanger 43

3.5. Traversing system 43

4. MEASUREMENT INSTRUMENTS 45

4.1. Manometer 45

4.2. Pitot-static tube 46

4.3. Pressure transducer 48

4.4. Hot-wire anemometer 49

5. EXPERIMENTAL SETUP 57

5.1. Coordinate system 57

5.2. Velocity and turbulence measurements 57

6. RESULTS AND DISCUSSION 61

6.1. Empty wind-tunnel test section 61

6.2. Wind-tunnel simulation of the atmospheric boundary layer flow 71

6.3. Boundary layer simulation using a surface grid 76

7. CONCLUSION 86

Bibliography 87

List of symbols

A	Cross-sectional area of structural member
c	Integration constant, coefficient of Pitot tube, flow velocity coefficient
d	Diameter
E	Output voltage
f	Frequency; also a reduced frequency defined is nL/V in descriptions of the atmospheric boundary layer
F_c	Coriolis force
f_m	Value of f for which $nS_u(z,n)$ is a maximum
g	Gravitation acceleration
h	Height
I_u , I_v , I_w	Turbulence inCnsity in the x -, y -, z - direction, respectively
I_w	Current intensity
k	Wave number
k_w	Wave number of the eddy
L_t	Integral length scale of longitudinal turbulence
${}^xL_u$	Integral length scale of longitudinal turbulence in x - direction
n	Frequency component of gusting. Also distance normal to isobars is $1/t$
p	Pressure
p_0	Stagnation pressure, total pressure, atmospheric pressure
p_s	Static pressure
p_t	Total pressure
p_∞	Pressure unaffected by body, static pressure
Δp	Pressure difference
P_r	Reference pressure
R_w	Resistance
q	Dynamic or wind pressure is $\frac{1}{2}\rho V^2$
q_r	Reference dynamic pressure is $\frac{1}{2}\rho V_r^2$
rms	Root mean square value
$S_u(z,u)$	Power spectral density of velocity fluctuations in the longitudinal direction
t	Time is $1/f$ or $1/n$
T	Absolute temperature; averaging time

T_0	Absolute reference temperature
ΔT_0	Change in absolute reference temperature
U	Wheatstone bridge voltage
u'	Fluctuating component of longitudinal wind speed
u_*	Friction velocity
$\bar{u}$	Mean velocity component in longitudinal direction, mean velocity
$\bar{u}(z)$	Mean *u*-component at height *z*
v'	Fluctuating component of lateral wind speed
v	Instantaneous component of lateral wind speed
$\bar{v}$	Mean lateral wind speed
v_0	Reference wind speed
v_r	Reference wind speed
$\bar{v}(z)$	Mean wind speed at height *z*
w	Instantaneous vertical component of wind speed
w'	Fluctuating vertical component of wind speed
$\bar{w}$	Mean vertical wind speed
x	Distance in longitudinal direction
y	Distance in lateral direction
z	Distance in vertical direction
z_0	Aerodynamic surface roughness length
z_r	Reference height used for the power law boundary layer approximation
α	Exponent in power law approximation boundary layer
γ_m	Specific liquid weight
γ_f	Specific flow weight
δ	Boundary layer thickness in the wind tunnel
ϕ	Angle of latitude
ϕ_{conv}	Convection heat flow
κ	Von Kármán constant
μ	Viscosity of air
ν	Kinematic viscosity of air is μ/ρ
ρ	Density of air
τ	Surface shear stress

Table of figures

Figure 1.1 Boundary layer wind tunnel, Closed circuit, Colorado State University [1] 17
Figure 1.2 Boundary layer wind tunnel, Open circuit, Colorado State University [1] 17
Figure 2.1 Orders of magnitude in space and time for different patterns of motion in the atmosphere [3] 18
Figure 2.2 Direction of pressure gradient force [2] 19
Figure 2.3 Schematic of the atmospheric boundary layer [2] 20
Figure 2.4 Equilibrium of forces in the atmospheric boundary layer [3] 20
Figure 2.5 Ekman spiral in the atmospheric boundary layer [3] 21
Figure 2.6 Schematic atmospheric boundary-layer structure for aerodynamically rough flow [5] 22
Figure 2.7 Atmospheric boundary layer wind velocities measured in the atmosphere [3] 23
Figure 2.8 Power-law exponent α in dependence on aerodynamic surface roughness length z_0 [11] 24
Figure 2.9 Aerodynamic surface roughness length z_0 in dependence on different terrains [10] 25
Figure 2.10 Simplified illustration of the aerodynamic surface roughness length z_0 [4] 26
Figure 2.11 Schematic representation of the energy power spectrum of velocity fluctuations [5] 30
Figure 2.12 Power spectrum of velocity fluctuations experimental results and empiric curve [14] 31
Figure 2.13 Reynolds stress in the atmospheric boundary layer [9] 33
Figure 3.1 Centre of Excellence Telč 34
Figure 3.2 Scheme of the Wind-tunnel 35
Figure 3.3 Scheme of the aerodynamic section 36
Figure 3.4 Honeycomb 36
Figure 3.5 Turntable with the structure model in place 37
Figure 3.6 Basic principles of the ABL wind-tunnel simulation using the Counihan method [18] 38
Figure 3.7 The barrier, the vortex generator spires, roughness fetch 38
Figure 3.8 Castellated barrier wall, all dimensions in mm 39
Figure 3.9 Roughness elements, all dimensions in mm 39
Figure 3.10 Grid as a turbulence generator 40

Figure 3.11 Scheme of the climatic section 40
Figure 3.12 Climatic section with the Infra-Red Lamps 41
Figure 3.13 Climatic section with water sprinklers 42
Figure 3.14 Fan 43
Figure 3.15 Traverse system 44
Figure 4.1 U-manometer scheme [19] 45
Figure 4.2 Schematic view of the static Pitot tube 47
Figure 4.3 Scanivalve DSA 3217 49
Figure 4.4 : Miniature wires, Gold-plated wires, Fibre-film or Film-sensors [20] 50
Figure 4.5 One-, two- and three-dimensional sensors [20] 50
Figure 4.6 Hot-wire design [20] 51
Figure 4.7 Schematic view of the constant temperature anemometry electric circle [20] 53
Figure 4.8 Measuring chain of the constant temperature anemometry [20] 54
Figure 4.9 Calibration curve of the constant temperature anemometry probe 1 55
Figure 4.10 Calibration curve of the constant temperature anemometry probe 2 56
Figure 5.1 Aerodynamic section coordinate system 57
Figure 5.2 Test matrix coordinate system, measures in mm 58
Figure 5.3 Positions of the examined crossections in a empty section 59
Figure 6.1 Overview of the empty section velocity distribution 62
Figure 6.2 Overview of the empty section turbulence intensity 63
Figure 6.3 Velocity distribution for an empty section, position x = 0 m 64
Figure 6.4 Turbulenc intensity distribution for an empty section, position x = 0 m 64
Figure 6.5 Velocity distribution for an empty section, position x = 2 m 65
Figure 6.6 Turbulence intensity distribution for an empty section, position x = 2 m 65
Figure 6.7 Velocity distribution for an empty section, position x = 4 m 66
Figure 6.8 Turbulence intensity distribution for an empty section, position x = 4 m 66
Figure 6.9 Velocity distribution for an empty section, position x = 6 m 67
Figure 6.10 Turbulence intensity distribution for an empty section, position x = 6 m 67
Figure 6.11 Velocity distribution for an empty section, position x = 8 m 68
Figure 6.12 Turbulence intensity distribution for an empty section, position x = 8 m 68
Figure 6.13 Velocity distribution for an empty section, position x = 9.3 m 69
Figure 6.14 Turbulence intensity distribution for an empty section, position x = 9.3 m 69
Figure 6.15 u velocity profile in the y-z plane along the test section 70
Figure 6.16 Velocity (left) and turbulence distribution (right) ABL simulation 72

Figure 6.17 Velocity distribution in the ABL simulation, section x = 0 m 73
Figure 6.18 Turbulence intensity distribution in the ABL simulation, section x = 0 m 73
Figure 6.19 Velocity distribution in theABL simulation, x = 1.5 m upwind from the turntable center 74
Figure 6.20 Turbulence intensity distribution in the ABL simulation, x = 1.5 m upwind from the turntable center 74
Figure 6.21 Velocity profile at y = 0 75
Figure 6.22 Turbulence intensity in longitudinal direction at y = 0 75
Figure 6.23 Velocity (left) and turbulence distribution (right) for grid placed on the wind tunnel floor at height 1cm 77
Figure 6.24 Velocity distribution, grid height 1 cm, x = 1 m downwind from turntable center ... 78
Figure 6.25 Turbulence intensity distribution, grid height 1 cm, x = 1 m downwind from turntable center 78
Figure 6.26 Velocity distribution, grid height 1 cm, x = 0 m at the turntable center 79
Figure 6.27 Turbulence intensity distribution, grid height 1 cm, x = 0 m at the turntable center. 79
Figure 6.28 Velocity distribution, grid height 1 cm, x = 1 m upwind from the turntable center . 80
Figure 6.29 Turbulence intensity distribution, grid height 1 cm, x = 1 m upwind from the turntable center 80
Figure 6.30 Velocity (left) and turbulence distribution (right) for grid placed on the wind tunnel floor at height 5 cm 81
Figure 6.31 Velocity distribution, grid height 5 cm, x = 1 m downwind from the turntable center 82
Figure 6.32 Turbulence intensity distribution, grid height 5 cm, section x = 1 m downwind from the turntable center 82
Figure 6.33 Velocity distribution, grid height 5 cm, x = 0 m at the turntable center 83
Figure 6.34 Turbulence intensity distribution, grid height 5cm, x = 0 m at the turntable center.. 83
Figure 6.35 Velocity distribution, grid height 5 cm, x = 1 m upwind from turntable center 84
Figure 6.36 Turbulence intensity distribution, grid height 5 cm, section x = 1 m upwind from turntable center 84

List of tables

Table 5.1 Experimental setup configurations overview 60

Abstract

An extensive set of experiments was carried out in the newly developed Vincenc Strouhal climatic wind tunnel in the Czech Republic in order to characterize flow and turbulence in this facility. This wind tunnel is capable of simulating atmospheric boundary layer flow, cold, solar radiation, rain, icing and a uniform flow with low turbulence. The tests performed in an empty wind-tunnel test section include velocity mapping at different longitudinal positions of the test section in order to investigate flow and turbulence uniformity. The atmospheric boundary layer flow simulated using the Counihan experimental hardware is reasonably uniform in the lateral direction. This indicates that the surface roughness can be successfully applied in creating and sustaining uniform turbulent flow conditions in the wind-tunnel test section. Velocity profile corresponds well to the commonly used power-law with an exponent α equal to 0.28, while the results for turbulence intensity are within the recommended ESDU74031 values for the simulated urban type terrain.

Sažetak

Ovaj rad je rezultat opsežnih ispitivanja izvedenih u Centru izvrsnosti Telč, u Češkoj Republici, u novo izgrađenom klimatskom zračnom tunelu Vincenc Strouhal. Tunel ima mogućnost simuliranja atmosferskog zračnog sloja, sunčevog zračenja, hlađenja i grijanja, nastanka mraza te ujednačenog strujanje niske turbulencije. Cilj istraživanja je bio ispitati i opisati strujanje zraka u tunelu. Prvi korak je ispitivanje polja brzine i turbulencije uzduž prazne mjerne sekcije tunela kako bi se ispitala uniformnost profila strujanja. Brzina strujanja je mjerena korištenjem užarene žice. Mjerenja su izvedena korištenjem dvije mjerne sonde, jedne na mjernom mjestu, presjeku, te druge na stropu , simetrali zračnog tunela. Također je korištena temperaturna korekcija koju je mjerio jedan termo-par. Izmjerena su polja brzine i turbulencije na više presjeka uzduž longitudinalnog smjera mjerne sekcije.

Drugi korak je ispitivanje formiranja simuliranog atmosferskog zračnog sloja u tunelu. Granični sloj je genereiran korištenjem Counihanove metode, gdje iskustva pokazuju da se eksperimentalni rezultati dobiveni u zračnom tunelu dobro podudaraju s rezultatima mjerenja iz prirode. Na izlazu iz sapnice i ulazu u mjernu sekciju zračnog tunela postavljena je nazubljena barijera. Strujanjem zraka preko barijere nastaju vrtlozi s horizontalnom osi vrtnje. Nizvodno od barijere smješteni su generatori vrtloga, koji potiču nastajanje vrtloga s vertikalnom osi vrtnje. Izborom odgovarajuće visine i gustoće elemenata podne hrapavosti modelira se struktura donjeg dijela graničnog sloja. Dodatno ispitan je i utjecaj metalne žičane mreže položene na pod tunela na generiranje graničnog sloja.

Rezultati mjerenja u praznoj mjernoj sekciji pokazuju ubrzanje strujanja duž mjerne sekcije, od ulaza do okretnog stola gdje se smještaju strukturni modeli za ispitivanje. Ubrzanjem strujanje postiže i do 10 % veće brzine strujanja na različitim presjecima uzduž mjerne sekcije. Mogući razlog tome je da mjerna sekcija u ovome trenutku nema postupno proširenje zidova ili pomicanje stropa u svrhu smanjenja gradijenta tlaka u mjernoj sekciji. Nadalje, zbog formiranja graničnog sloja na podu, zidovima te stropu zračnog tunela dolazi do značajnog ubrzanja središnjeg dijela toka.

Analiza strukture modeliranog atmosferskog graničnog sloja i promjene strukture strujanja na dva presjeka mjerne sekcije, tj. na centru okretnog ispitnog stola (x = 0 m) te uzvodno od centra ispitnog stola (x = 1,5 m), pokazala je da se korištenjem generatora turbulencije i elemenata podne hrapavosti može poboljšati uniformnost strujanja u usporedbi sa strujanjem u praznoj mjernoj sekciji. Profil brzine se nalazi unutar preporučenih $\pm$15% iznosa prema međunarodnom standardu ESDU74031 te odgovara eksponentu zakona potencije α = 0.28. Simulirani granični sloj odgovara profilu strujanja u urbanim sredinama.

1. INTRODUCTION

A new climatic wind tunnel has been built recently in Telč, Czech Republic, at the Centre of Excellence Telč. As with every new wind tunnel, the first step is the detailed mapping of turbulent flow characteristics. In the next step, commonly the characteristics of the boundary layer simulation are being investigated prior to proceeding with test on engineering structures, air pollution dispersion, wind energy and urban micrometeorology. This type of wind tunnel has been commonly used in the field of wind engineering.

The atmospheric boundary layer (ABL) is the region of air which is greatly influenced by the Earth's surface roughness. For structural design purposes, it is important to understand the atmospheric boundary layer and the turbulent flow characteristics associated with it. Although computer modeling has come a long way in trying to model the ABL, there are still many unexplained complexities associated with the flow. Therefore, wind tunnel simulation remains an important research tool in the field of environmental aerodynamics and wind engineering.
Within the last 30 years wind tunnels have evolved as an indispensable aid to the practice of civil engineering. Major applications to civil engineering are through wind-tunnel tests for wind effects on structures. Another important class of civil- engineering applications in which wind-tunnel investigations contribute valuable information is treatment of wind-related environmental problems. The boundary layer wind-tunnel (BLWT) concept introduced in 1958 [1] which is still in general use today. The benefits of BLWT tests on structures were not fully realized until new concepts and capabilities for data-acquisition systems were developed. Uniqueness of this facility is derived from the long test section which allows for development of thick turbulent boundary layers, heating and cooling capabilities for creating thermally stratified boundary layers and a flexible ceiling for adjustment of pressure along the test-section length.
There are two main types of a BLWT wind-tunnel, i.e. closed circuit wind-tunnels and open circuit wind-tunnels. The closed-circuit BLWT as shown in Fig 1.1 provide flow free from external disturbances and laboratory space free from disturbing air currents. However, open circuit BLWTs similar to the facility shown in Fig. 1.2 have been constructed throughout the world since about 1965 and more are under construction. Major advantages of the open-circuit BLWT are lower construction costs and a requirement of less laboratory space than for a closed-circuit BLWT with the same test-section length.

The scope of this thesis is to perform wind profile measurements in an empty test section. In addition, it is attempted to simulate the boundary layer flow by using the commonly accepted Counihan method.

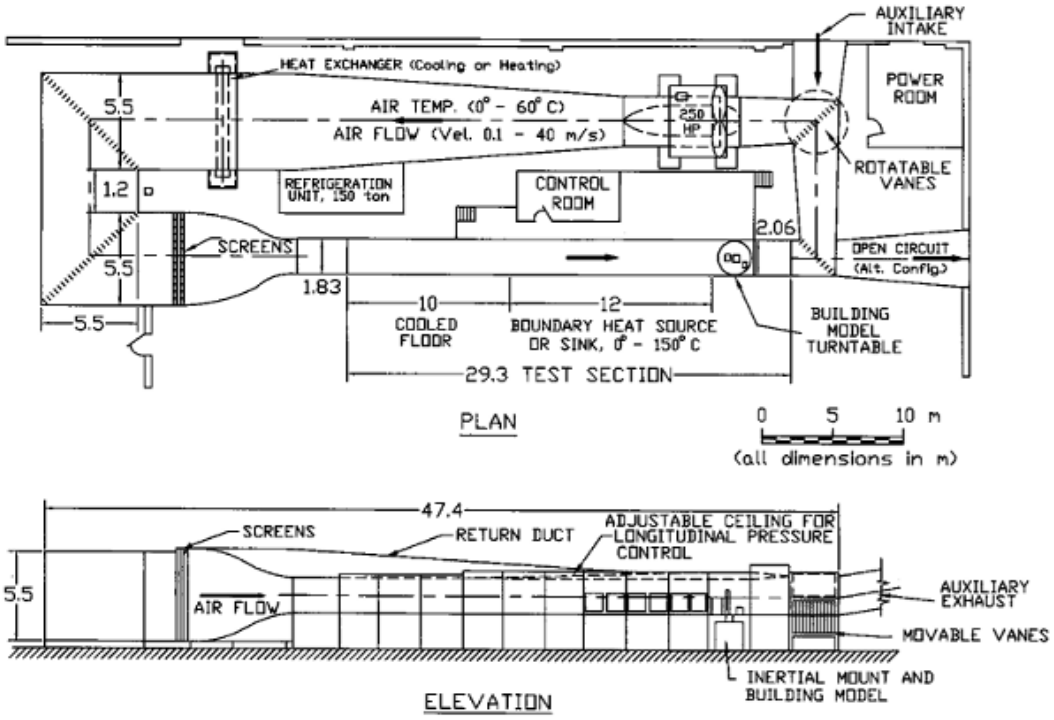

Figure 1.1 Boundary layer wind tunnel, Closed circuit, Colorado State University [1]

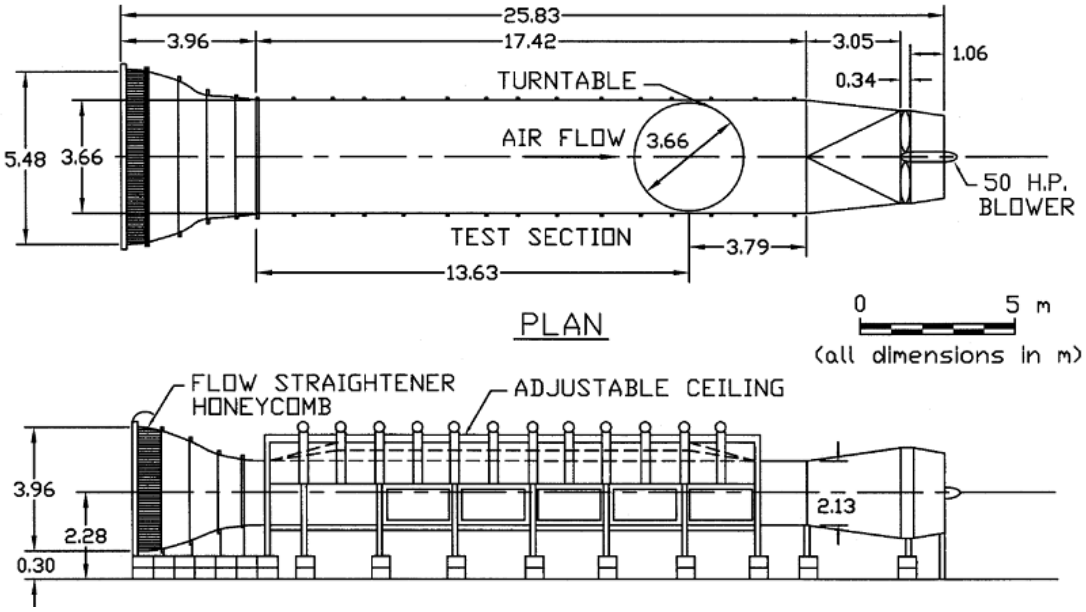

Figure 1.2 Boundary layer wind tunnel, Open circuit, Colorado State University [1]

2. CHARACTERISTICS OF THE ATMOSPHERIC WIND

Wind is fundamentally caused by heat radiated by the sun. Radiation, thermodynamic, and mechanical phenomena transform the thermal energy imparted to the atmosphere into mechanical energy associated with air motion, giving rise to various types of wind [2]. Atmospheric motion usually takes place in such a way that different patterns of motion are mutually independent both in time and in space. Fig. 2.1 shows that the patterns of atmospheric motion range from turbulence (vortices of air in the range of a few meters with a characteristic lifetime of some minutes) to local weather systems and large planetary waves, which may circumvent the entire globe and have a lifetime of several days. These phenomena are referred to as microscale, convective scale and macroscale, respectively [3].

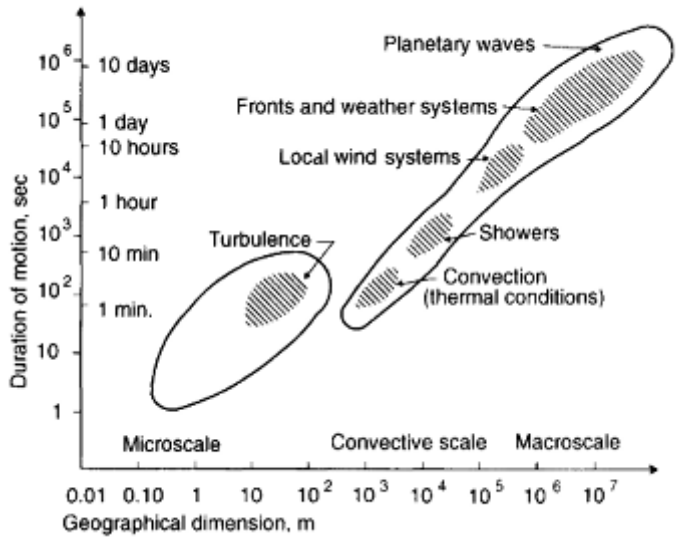

Figure 2.1 Orders of magnitude in space and time for different patterns of motion in the atmosphere [3]

The motion of an elementary air mass is determined by forces that include a vertical buoyancy force. Depending upon the temperature difference between the air mass and the ambient air, the buoyancy force acts upwards (causing an updraft), downwards, or is zero. These three cases correspond to unstable, stable, or neutral atmospheric stratification, respectively. The horizontal motion of air is determined by the horizontal pressure forces, Coriolis force and the force of friction [2].

The horizontal pressure gradient force due to the spatial variation of the horizontal pressure force is normal to the lines of constant pressure, called isobars, and is directed from high-pressure to low-pressure regions (Fig. 2.2). The net force per unit mass exerted by the horizontal pressure gradient is:

$$P = (1/\rho)\mathrm{d}p/\mathrm{dn}. \qquad (2.1)$$

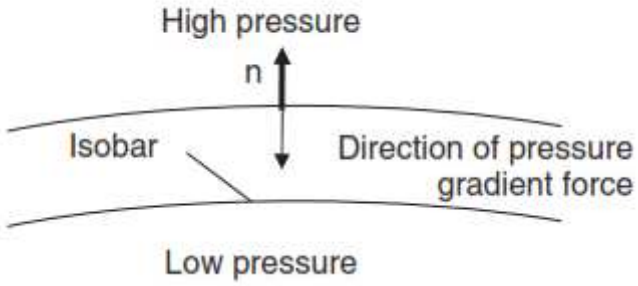

Figure 2.2 Direction of pressure gradient force [2]

If defined with respect to an absolute frame of reference, the motion of a particle not subjected to the action of an external force will follow a straight line. To an observer on the rotating Earth, however, the path described by the particle will appear curved. The deviation of the particle with respect to a straight line fixed with respect to the rotating Earth may be attributed to an apparent force, the Coriolis force:

$$F_c = mfv, \qquad (2.2)$$

where m is the mass of the particle, $f = 2\omega \sin \phi$ is the Coriolis parameter, $\omega = 0.7272 \times 10^{-4}$s is the angular velocity vector of the Earth, ϕ is the angle of latitude, and v is the velocity vector of the particle referenced to a coordinate system fixed with respect to the Earth. The force Fc is normal to the direction of the particle motion, and is directed according to the vector multiplication rule.

The surface of the Earth exerts upon the moving air a horizontal drag force that retards the flow. This force decreases with height and becomes negligible above a height δ known as a gradient height. The atmospheric layer between the Earth's surface and the gradient height is called the atmospheric boundary layer. The wind velocity at height δ is called the gradient velocity, and the atmosphere above this height is called the free atmosphere and the wind is geostrophic (Fig. 2.3).

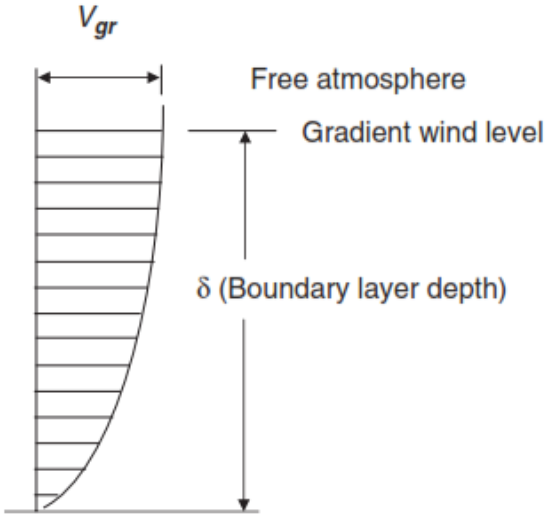

Figure 2.3 Schematic of the atmospheric boundary layer [2]

The equilibrium of forces in the boundary layer is illustrated in Fig. 2.4. The state of equilibrium corresponds to a wind direction which crosses the isobars. There is equilibrium between the force due to the pressure gradient, the Coriolis force and the friction generated. The wind direction continues to change down through the boundary layer and the wind speed gradually decreases to zero, as reported Fig. 2.5. The turn is typically 20°, but it may vary between approximately 10° and 45° depending on ground roughness and atmospheric stability [3].

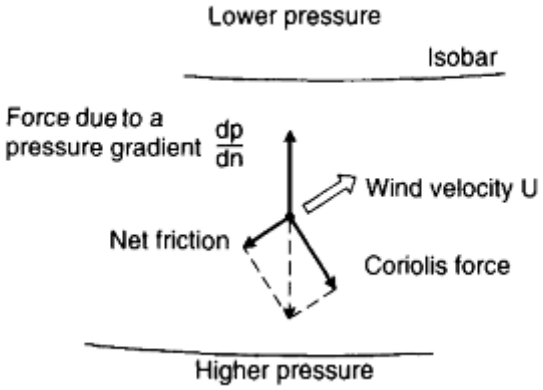

Figure 2.4 Equilibrium of forces in the atmospheric boundary layer [3]

The friction force, which retards the wind flow and vanishes at the gradient height, decreases as the height above the surface increases. Therefore, the velocity increases with height (Fig 2.5).
The Coriolis force, which is proportional to the velocity, also increases with height. The combined effect of the Coriolis force and the friction force is such that the angle between the

direction of motion and the isobars increases from zero at the gradient height to its largest value at the Earth's surface. The wind velocity in the boundary layer height can therefore be represented by the Ekman spiral [2] (Fig. 2.5).

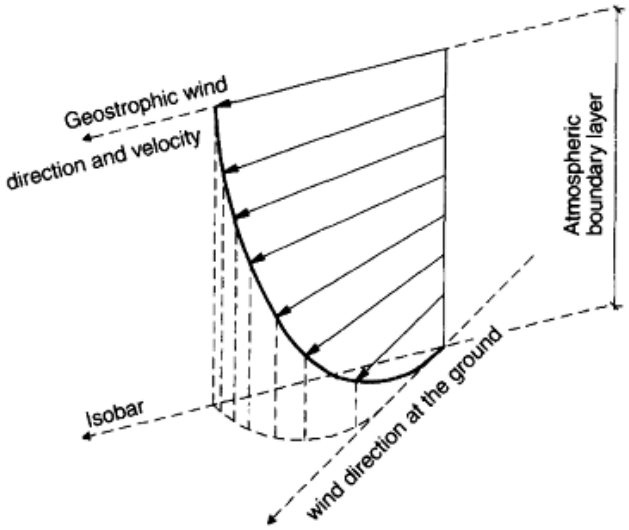

Figure 2.5 Ekman spiral in the atmospheric boundary layer [3]

In the area of civil engineering most commonly the ABL is examined, the turbulent boundary layer which is characterized by the flows velocity and the surface roughness of the Earth. Heights up to 600 m can be considered as a mean boundary layer thickness according to [4].

The structure of the atmospheric boundary layer shows many similarities to the two-dimensional turbulent boundary layer generated in a wind-tunnel, whereas both have a distinctive inner region and outer region (Fig. 2.6). In the outer region, the flow shows small dependence on the nature of the surface. In the atmosphere, the Coriolis force due to the Earth's rotation becomes more important. This region is sometimes referred to as the Ekman layer, as Ekman (1905) first studied the rotation effects on boundary-layer flow over the ocean. The flow in the inner layer (also known as the wall or surface layer) is mainly dependent on surface characteristics and is only slightly affected by rotation. The transition between the inner and outer layers is not abrupt, as it is characterized by an overlap region. The influence of the surface can be observed in the interfacial sublayer, which is the layer of air within and just above the roughness elements comprising the land or sea surface. In this layer, molecular diffusion is an important process where heat and mass are exchanged between the surface and the air [5]. The interfacial layer thickness is defined as the zero-plane displacement.

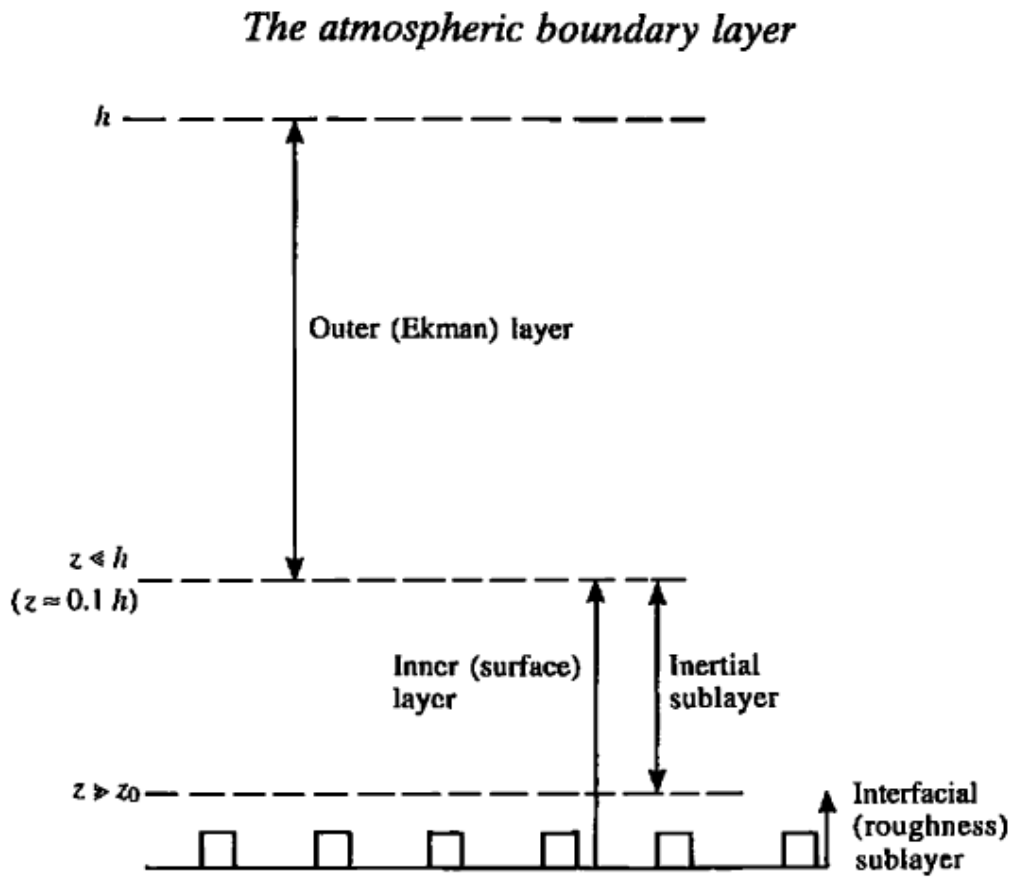

Figure 2.6 Schematic atmospheric boundary-layer structure for aerodynamically rough flow [5]

In simulating the ABL flow, it is important to accurately describe the ABL and its characteristics. The relevant wind characteristics, as given in Simiu and Scanlan [6], include the following:

- The variation of the mean wind speed with height.
- The variation of turbulence intensities and integral length scales with height.
- The spectra and cross-spectra of turbulence in the along-wind, cross-wind, and vertical directions.

2.1. Mean velocity characteristics

The flow in the ABL is strongly turbulent, as presented in Fig. 2.7. The absolute velocity (u, v, w) is represented as the sum of the mean velocities $\bar{u}, \bar{v}, \bar{w}$ and the fluctuating components u', v', w' as in the following terms:

x – longitudinal direction $u = \bar{u} + u'$,

y – lateral direction $v = \bar{v} + v'$,

z – vertical direction $w = \bar{w} + w'$.

This procedure is commonly known as Reynolds averaging, where the mean value in the x-direction is equal to:

$$\bar{u} = \frac{1}{T} \int_{-T/2}^{T/2} u(t - T)\mathrm{d}t\,, \qquad (2.3)$$

where T is acquisition time. The ABL flow is three dimensional, where the $\bar{u} >> \bar{v}$ and $\bar{u} >> \bar{w}$, and therefore the $\bar{v}$ and $\bar{w}$ velocity components can be neglected when analyzing the experimental results in a wind-tunnel.

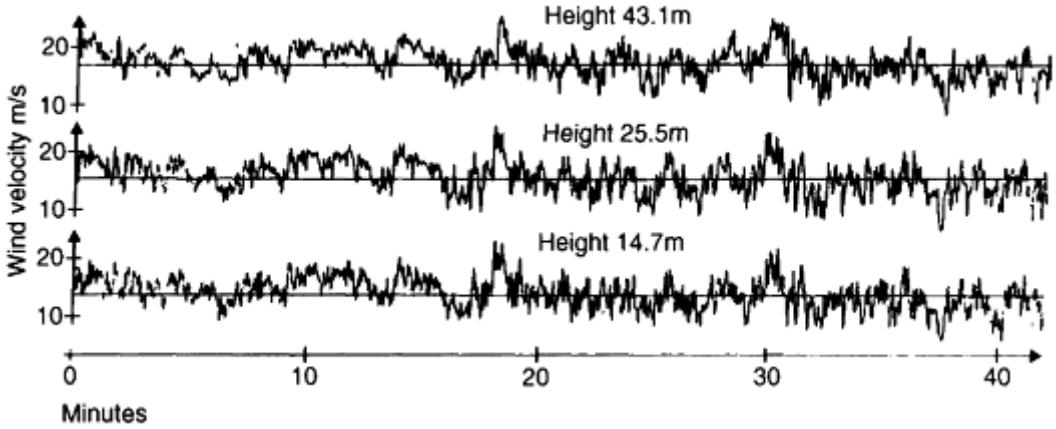

Figure 2.7 Atmospheric boundary layer wind velocities measured in the atmosphere [3]

As the air flows across a long homogenous surface (longer than 5-10 km), an equilibrium boundary layer is developed. There are many ways of defining the vertical velocity distribution of the longitudinal velocity, *u*. According to Stevenson [7] the parabolic law:

$$\frac{\bar{u}}{\bar{u}_{\mathrm{ref}}} = \sqrt{\left(\frac{z+22}{z_{\mathrm{ref}}+22}\right)}. \qquad (2.4)$$

However, it does not apply to the lower 10 m of the vertical wind profile. A more suitable empirical model for mean gust wind speed profiles utilized a power law model of the following form [8]:

$$\frac{\bar{u}}{\bar{u}_{\mathrm{ref}}} = \left(\frac{z}{z_{\mathrm{ref}}}\right)^{\alpha}. \qquad (2.5)$$

.

The longitudinal velocity $\bar{u}$ (z) is the time averaged velocity at a distance z above the surface. The velocity distribution is generally normalized against at a meteorological standard height of z_{ref} = 10 m above the surface. The exponent of the power law α is a function of the terrain roughness (Fig 2.8). While an improvement of the Stevenson's parabolic law, this model is also not analytically correct for the measured velocities in the lower 10 m of the ABL. Nonetheless, it is still widely used due to its simplicity [9].

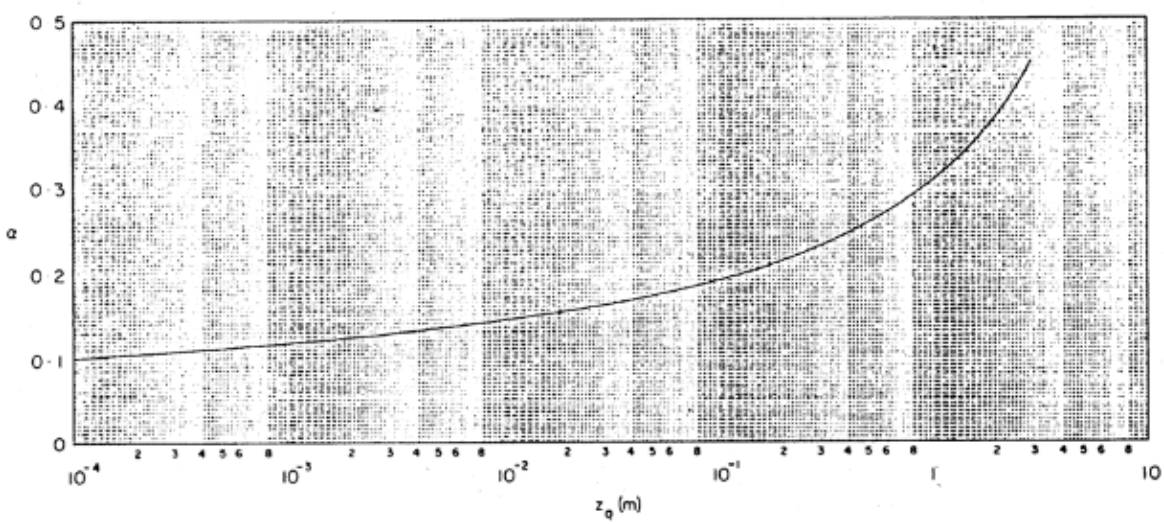

Figure 2.8 Power-law exponent α in dependence on aerodynamic surface roughness length z_0 [10]

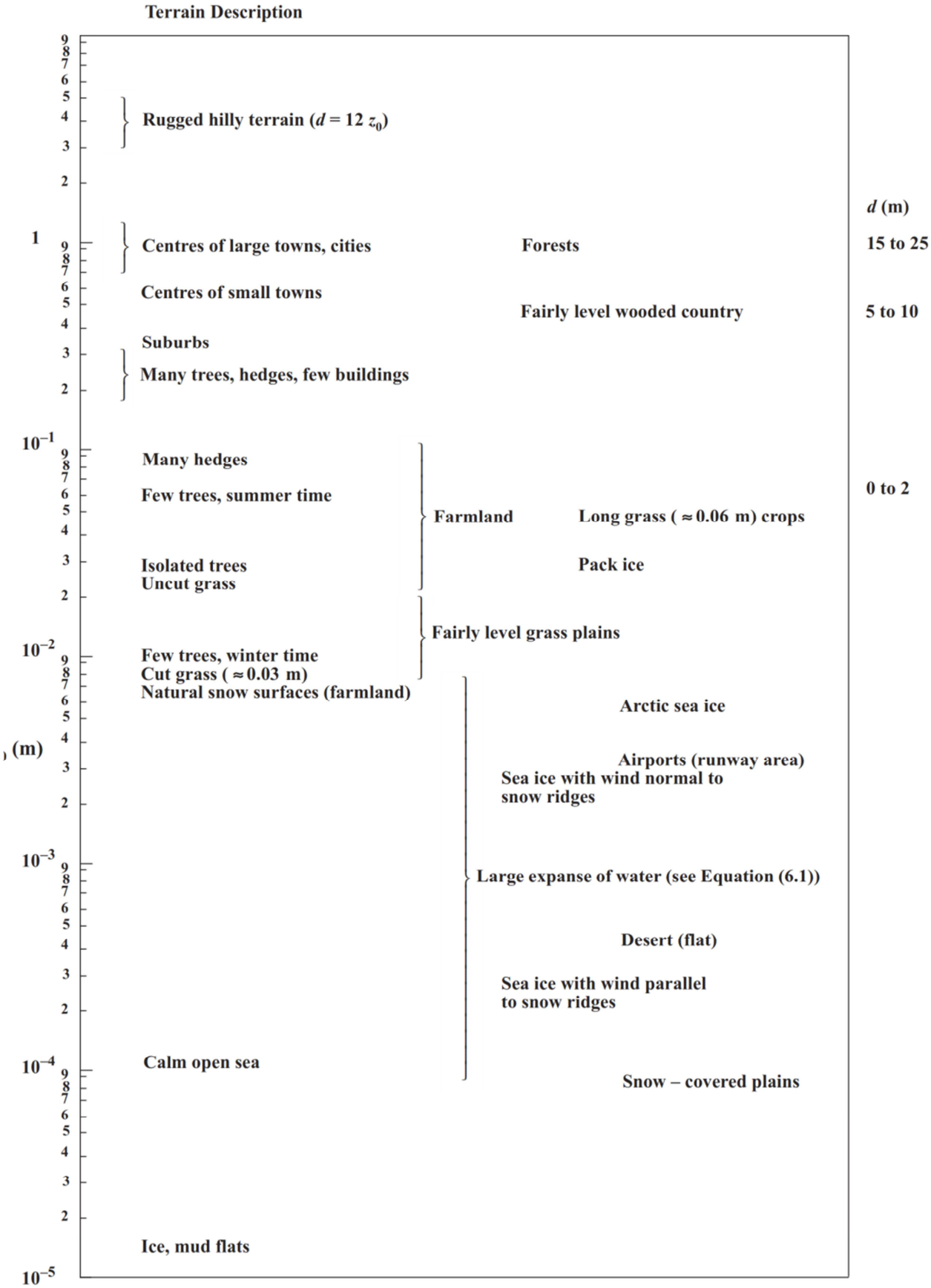

Figure 2.9 Aerodynamic surface roughness length z_0 in dependence on different terrains [10]

Sutton [11] developed a more suitable representation of the mean velocity profile that is applicable to the lower than 10 m heights and the inertial sublayer. Within this region, the descriptions for the outer and inner layer scaling are valid simultaneously. Sutton's mean velocity profile follows a logarithmic relation as follows:

$$\bar{u} = \frac{1}{\kappa} u_* ln\left(\frac{z-z_d}{z_0}\right); \kappa = 0.4, \qquad (2.6)$$

where κ is the von Kármán constant which is based on experiments in wind-tunnels and in the atmosphere. Equation (2.6) is commonly known as the logarithmic law-model. This law takes into account the zero plane displacement z_d when considering large roughness elements. Equation (2.6) also includes two other important parameters: the aerodynamic surface roughness length z_0 and the friction velocity u_*.

The aerodynamic surface roughness length z_0 (Fig. 2.10) is defined as the height above the ground where the wind speed becomes zero due to the effects of vegetation or obstacles. Typical roughness heights defined by Simiu and Scanlan [6] are the following:

1. Urban: $2 \text{ m} < z_0 < 3 \text{ m}$
2. Suburban: $0.2 \text{ m} < z_0 < 1.2 \text{ m}$
3. Rural: $0.001 \text{ m} < z_0 < 0.2 \text{ m}$
4. Smooth: $0.001 \text{ m} < z_0 < 0.006 \text{ m}$

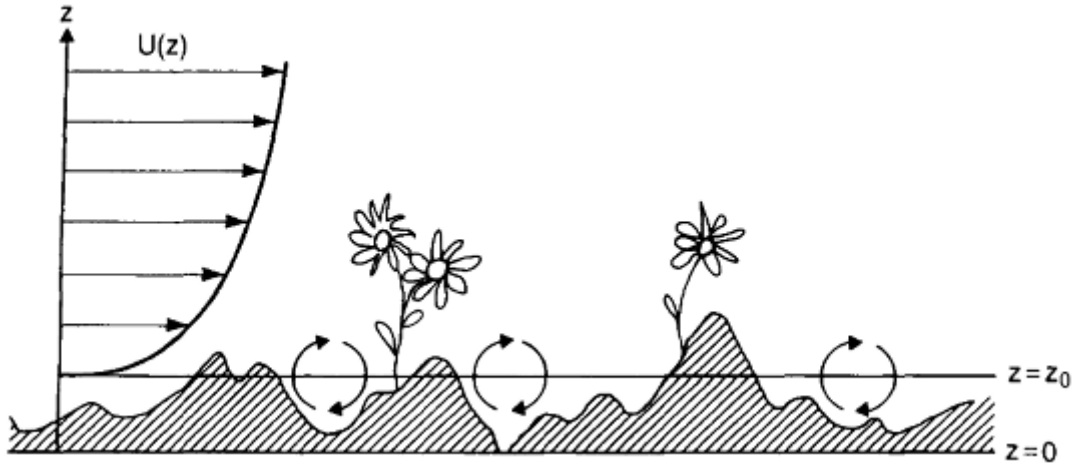

Figure 2.10 Simplified illustration of the aerodynamic surface roughness length z_0 [3]

The friction velocity is defined as the square root of the wall shear stress divided by the ambient density,

$$u_* = \sqrt{\frac{\tau_w}{\rho}}, \tag{2.7}$$

and the wall shear stress τ_w, is defined by,

$$\tau_w = \mu \left(\frac{d\bar{u}}{dy}\right)_{y=0}. \tag{2.8}$$

The Reynolds stress (- $\rho\overline{u'w'}$) is maximum at the zero-plane displacement, and is the surface sheer stress transferred through the surface layer. The definition of friction velocity at the zero plane displacement can therefore be extended to the following equation:

$$u_* = \sqrt{-\overline{u'w'}}. \tag{2.9}$$

2.2. Turbulence characteristics

The airflow within the ABL is extremely turbulent. The data about the atmospheric turbulence properties are very important in wind engineering and the three main reasons for that are [12]:

- Rigid constructions are exposed to unstationary loads due to the wind turbulence.
- Vibrations are emphasized in the flexible constructions resonance field due to wind pulsations.
- The constructions aerodynamic response is in direct correlation with the turbulence structure.

The relevant characteristic parameters of atmospheric turbulence are turbulence intensity, integral length scale of turbulence, Reynolds stress and power spectral density of velocity fluctuations.

2.2.1. Turbulence intensity

Turbulence intensity is the one of the main parameters used to describe atmospheric turbulence. If the $u'(z)$ is the fluctuation of the mean velocity, $\bar{u}$ in the longitudinal direction at height z the turbulence intensity yields to:

$$I_u = \frac{\sqrt{u'^2(z)}}{\bar{u}_{\mathrm{ref}}}, \qquad (2.10)$$

where the $\bar{u}_{\mathrm{ref}}$ is the mean velocity value in the longitudinal direction, usually at the boundary layer thickness height, measuring point height or at the examined model height. The same is valid for the lateral and vertical directions:

$$I_v(z) = \frac{\sqrt{v'^2(z)}}{\bar{v}_{\mathrm{ref}}}, I_w(z) = \frac{\sqrt{w'^2(z)}}{\bar{w}_{\mathrm{ref}}}. \qquad (2.11)$$

According to the measurements in the atmosphere the relations I_v/I_u and I_w/I_u are constant close to the ground surface and according to Counihan [4]:

$$\frac{I_v}{I_u} = 0.75 \text{ and } \frac{I_v}{I_u} = 0.50.$$

2.2.3. Integral length scale of turbulence

Turbulent velocity fluctuations may be considered as result from the passage of a sequence of eddies, each characterized by a periodic motion of circular frequency $\omega = 2\pi f$, where f is frequency, or by a wave number $k=2\pi/\lambda$, where λ is wave length. The wave length represents a magnitude of the eddy size. The total kinetic energy of the turbulent motion may, correspondingly, be regarded as a sum of contributions of all eddies in the flow. The integral length scale is a quantity of the average eddy size at a given position. There are in total nine integral length scales (three eddy dimensions with three wind flow velocity fluctuations directions). $L_{u,x}$, $L_{u,y}$ and $L_{u,z}$ represent the average eddy size in the longitudinal, lateral and vertical direction caused by the wind velocity fluctuations in the longitudinal direction. According to Sockel [13], the mathematical expression for $L_{u,x}$ yields to:

$$L_{u,x} = \int_0^\infty R_{u,x}\,(\Delta x)\mathrm{d}\Delta x, \qquad (2.12)$$

$$R_{u,x}(\Delta x) = \frac{\overline{u_1'(t)\cdot u_2'(t)}}{\sqrt{\overline{u_1'^2}}\cdot\sqrt{\overline{u_2'^2}}}\ , \qquad (2.13)$$

where the indices 1 and 2 denote two different positions in space. The turbulence length scales are possible to define by the use of the Taylor's frozen turbulence hypothesis (the wind fluctuations are moving at the mean velocity of the main current). Then it follows:

,

$$R_{u,x}(\Delta x) = \frac{\overline{u_1'(t)\cdot u_1'(t-\Delta t)}}{\overline{u_1'^2}} = R_{u,x}(\Delta t);\ \Delta t = \frac{\Delta x}{u}, \qquad (2.14)$$

$$L_{u,x} = \bar{u}\int_0^\infty R_{u,x}\,(\Delta t)\mathrm{d}\Delta t. \qquad (2.15)$$

2.2.4 Power spectral density of velocity fluctuations

A function that describes the distribution of turbulence with time is called the spectral density function, usually called power spectrum. It is defined so that the contribution to the mean velocity variance (or square of the standard deviation) in the range of frequencies from *f* to *f*+d*f*, is given by $S_u(f)\cdot\mathrm{d}f$, where *Su(f)* is the spectral density function for *u*(*t*). Then, integrating over all frequencies,

$$\sigma_u^2 = \int_0^\infty S_u(f)\mathrm{d}f, \qquad (2.16)$$

where $\sigma_u = \sqrt{\overline{u'}}$. (2.17)

Lower frequencies indicate larger-scale motions, eddies, while higher frequencies indicate small-scale motions. With the air flow over a rough surface a structure of eddies of specific size is formed, which are then dissipated in smaller eddies. This size dissipation transfers the kinetic energy from the larger eddies to smaller. This process is called the cascade energy transport. Eddies containing the most energy are not the largest. Actually eddies somewhat smaller than the largest eddies carry more energy. The maximum energy is contained in the middle of the spectrum inertial subrange where the dominant forces are the inertial forces. In that area the law of Kolmogorov is valid,

$$S_u(f) \approx k_w^{\frac{-3}{5}}, \qquad (2.18)$$

where k_w is the wave number of the eddy. The area of highest frequencies and the smallest eddies is called the dissipation zone. In that area the transformation of the kinetic energy into heat is dominant. The dissipation zone is usually not examined in the field of wind engineering. A scheme of the velocity power spectrum is given in Fig 2.11.

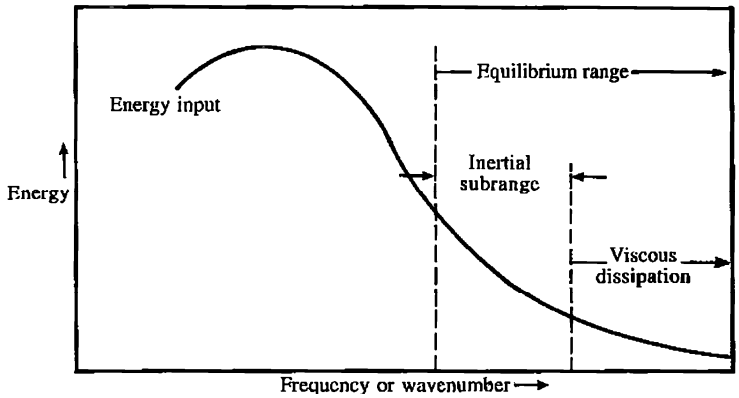

Figure 2.11 Schematic representation of the energy power spectrum of velocity fluctuations [5]

An example of the power spectrum by Davenport [14]:

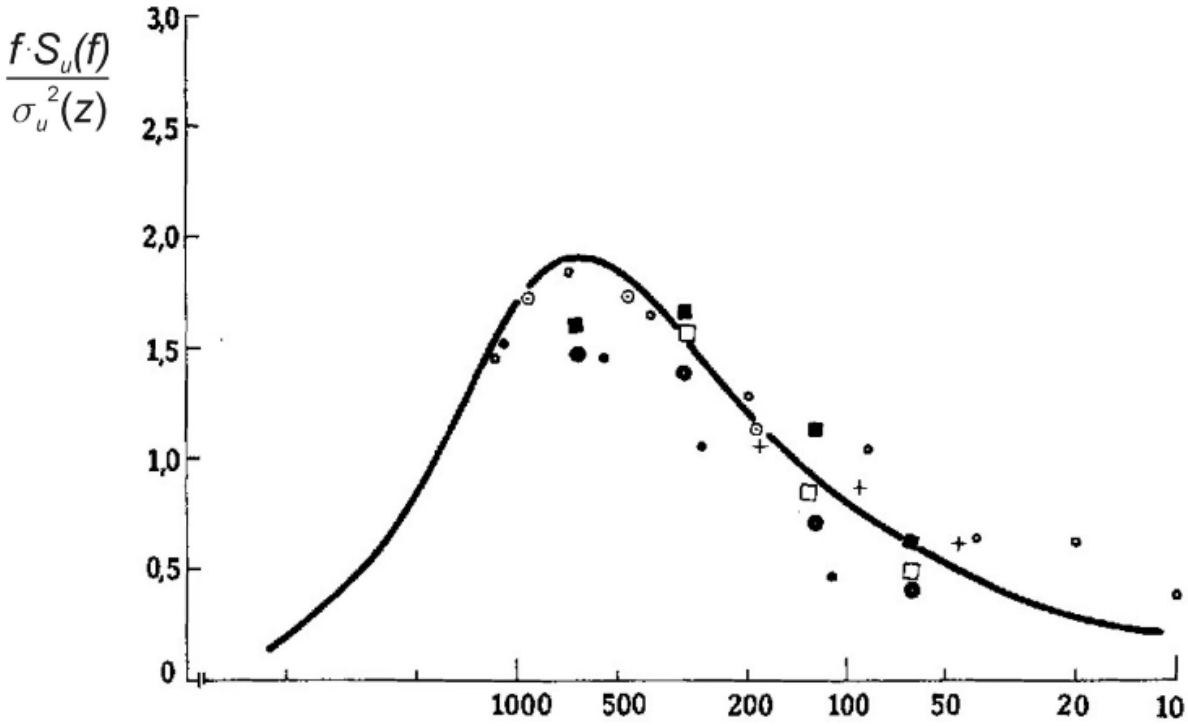

Figure 2.12 Power spectrum of velocity fluctuations experimental results and empiric curve [14]

Based on comparison of theoretical research results and experimental results, Pröpper [15] realized that the Kolmogorov's energy distribution term represents a good match with the results in the atmosphere,

$$\frac{f \cdot S_u(f)}{\sigma_u^2} = \frac{4 \cdot X_u}{\left(1 + 70{,}78 \cdot {X_u}^2\right)^{5/6}}. \quad (2.19)$$

With the X_u, nondimensional frequency,

$$X_u = \frac{f \cdot L_{u,x}(z)}{\bar{u}(z)}, \quad (2.20)$$

and the integral length scale,

$$L_{u,x} = \frac{0.146 \cdot \bar{u}(z)}{f_m}, \qquad (2.21)$$

where f_m is frequency with the maximum *f·Su(f),* determined through measurements.

2.2.5 Turbulent Reynolds stress

Friction forces develop predominantly close to the Earth's surface and they transfer in the upper layers of the boundary layer through the shear stress. The shear stress consists of viscous and turbulent shear stress, also called Reynolds stress,

$$\tau = \mu \frac{\partial \cdot \bar{u}}{\partial z} - \rho \overline{u'w'}. \qquad (2.22)$$

The viscous term's $\mu \frac{\partial \cdot \bar{u}}{\partial z}$ maximum is at the surface, it decreases with height and it is negligible in the inertial sublayer in comparison with the Reynolds stress term $-\rho \overline{u'w'}$. The magnitude of the Reynolds stress is zero at the surface and increases height with (Fig. 2.13). Within the surface layer the Reynolds stress is usually constant [10]. In the Ekman layer the stress reduces with height and becomes zero at the boundary layer thickness height. In the wind engineering, mostly Reynolds shear is examined. It is defined by the following correlations $\overline{u'v'}, \overline{v'w'}, \overline{u'w'}$ which are equal to zero if the turbulence is considered to be isotropic. Within the ABL the turbulence is anisotropic where the the $\overline{v'w'}, \overline{u'w'}$ can be neglected according to the ESDU [10]. Therefore, Reynolds stress can be defined as,

$$\tau = -\rho \overline{u'w'} = \rho u_\tau^2 (1 - z/\delta)^2. \qquad (2.23)$$

From the Earth's surface and up to 300 m, according to the ESDU [10],

$$\frac{-\overline{u'w'}}{\sigma_u \sigma_w} \approx \frac{u_\tau^2 \left(1 - 2\frac{z}{\delta}\right)}{\sigma_u \left(\frac{\sigma_w}{\sigma_u}\right) \sigma_u} = \frac{1 - 2\frac{z}{\delta}}{\left(\frac{\sigma_u}{\sigma_\tau}\right)^2 \left(\frac{\sigma_w}{\sigma_u}\right)}, \tag{2.24}$$

where the $\frac{\sigma_w}{\sigma_u} \approx 0.55$, $\frac{\sigma_u}{\sigma_\tau}$ is defined using (2.25), under condition that the ABL is in the state of equilibrium,

$$I_u = \frac{\sigma_u}{\sigma_\tau} \frac{u_\tau}{v_\infty}. \tag{2.25}$$

The sign of the $\rho\overline{u'w'}$ stress is defined according to Schlichting and Gersten [16]: "A fluid particle which is moving vertically up (in the positive direction) where the w' is coming from area with lower velocity $\bar{u}$. The particle contains its velocity and causes a negative pulsation u' in the upper layer and vice versa. Therefore the values of Reynolds stress $\rho\overline{u'w'}$, are negative."

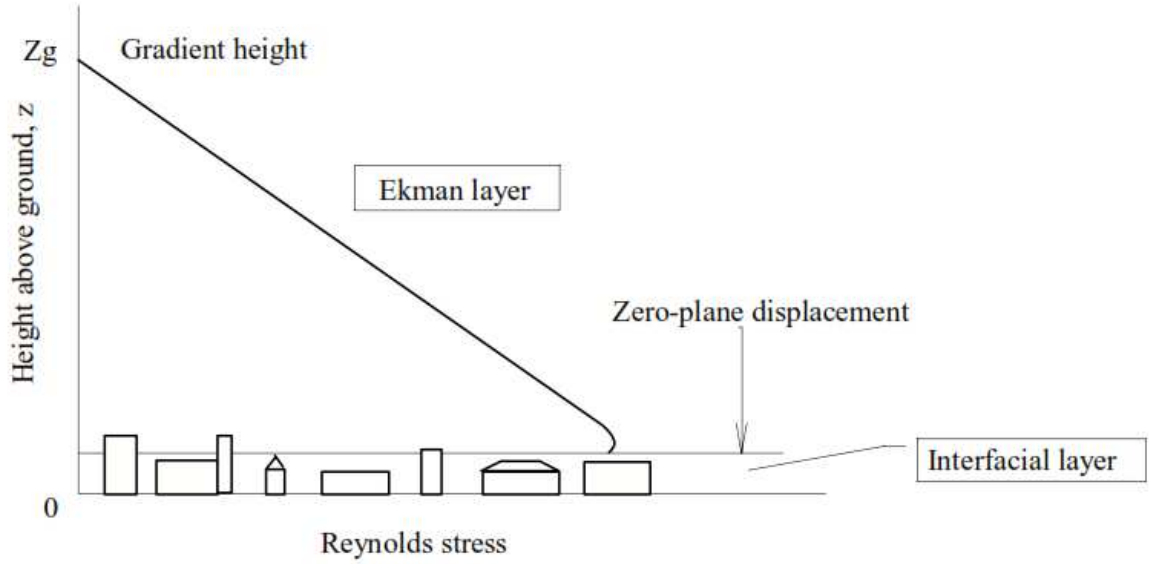

Figure 2.13 Reynolds stress in the atmospheric boundary layer [9]

3. WIND-TUNNEL DESIGN

In 2009 the Institute of Theoretical and Applied Mechanics (ITAM) of Czech Academy of Science introduced the new ARCCHIP "Centre of Excellence Telč" (CET) for research on materials and structures, particularly historical materials and structures. CET is equipped with a unique infrastructure carefully designed and manufactured with a respect to obtaining fundamental knowledge and verifying the application and innovation potential of newly developed technologies in the domain of diagnostics, life cycle extension, preventive protection and conservation. The CET infrastructure consists of a new climatic wind-tunnel of environmentally and economically optimized size for research on structural materials and technologies, equipped with locally-developed measuring and simulation tools. The scientific objective of the climatic wind-tunnel is to create models of the interactions between solid bodies and the surrounding environment, utilizing the findings obtained by numerical and experimental modeling of the influence of wind on structures, including monuments, and taking into account the influence of other weather factors, e.g. cyclic changes in temperature and exposure to rain. A further objective is to obtain new findings and knowledge by means of long-term sustainable monitoring and modeling of the behavior of real structures exposed to long-term weather effects and susceptible to vibrations and to damage caused by high-cycle fatigue. The scientific projects lead to outputs in the form of proposals for dealing with the aeroelastic and aerodynamic behavior of structures, models and proposals for measures to provide a more comfortable environment in housing estates and in the neighborhood of transportation infrastructure. Knowledge is acquired based on simulations of the effect on buildings, historic objects and monuments of the most important climatic parameters, e.g. wind, temperature, solar radiation, rain and humidity.

Figure 3.1 Centre of Excellence Telč

The wind-tunnel design (Fig 3.2) was constrained by the need to provide a simulation of an atmospheric boundary layer, cold, solar radiation, rain, icing and alternatively a uniform flow with low turbulence.

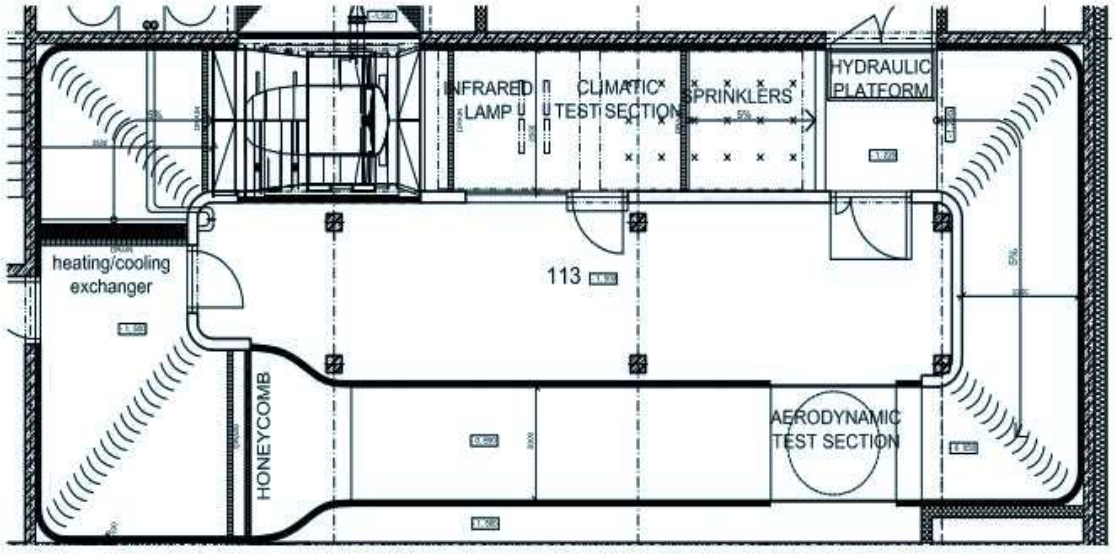

Figure 3.2 Scheme of the Wind-tunnel

The wind-tunnel is of the closed-circuit type with the fan placed in the outlet of the test sections, which means that the static pressure in the examining sections is below the atmospheric pressure. The wind-tunnel consists of an inlet section, an aerodynamic section, a climatic section, a return section, and a fan section. The wind-tunnel has thermal insulation and the climatic section floor has a drainage system.

The operation of the wind-tunnel is controlled from the control room which is surrounded by the tunnel structures, providing easy monitoring of the tunnel functions and the personal engaged in and around the tunnel through a series of built-in windows and cameras. The control room is equipped with high processing computers and equipment used for control and measuring purposes. Via an analog and digital signal bus system it is easy to establish connections between equipment in the wind-tunnel and the control room.

3.1. Aerodynamic section

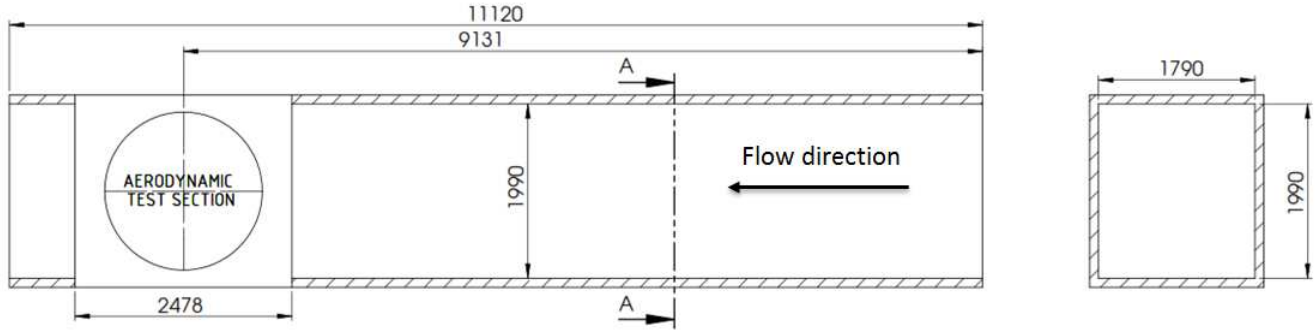

Figure 3.3 Scheme of the aerodynamic section

The aerodynamic section (Fig. 3.3) consists of the contraction and the test section. The contraction with a honeycomb has a ratio of 2.7:1. Its form is determined by a classical calculation of the potential flow. The honeycomb (Fig. 3.4) is 60 mm long and its basic element is a regular hexagon with a longest diagonal 6 mm. It serves to improve flow uniformity and reduce turbulence at the inlet of the test section. The test section has a rectangular cross-sectional area which is 1.8 m high and 2 m wide and it allows the air flow speed range from 0.8 m/s up to 28 m/s. The total length of the test section, including the part for boundary layer development, is 11.0 m.

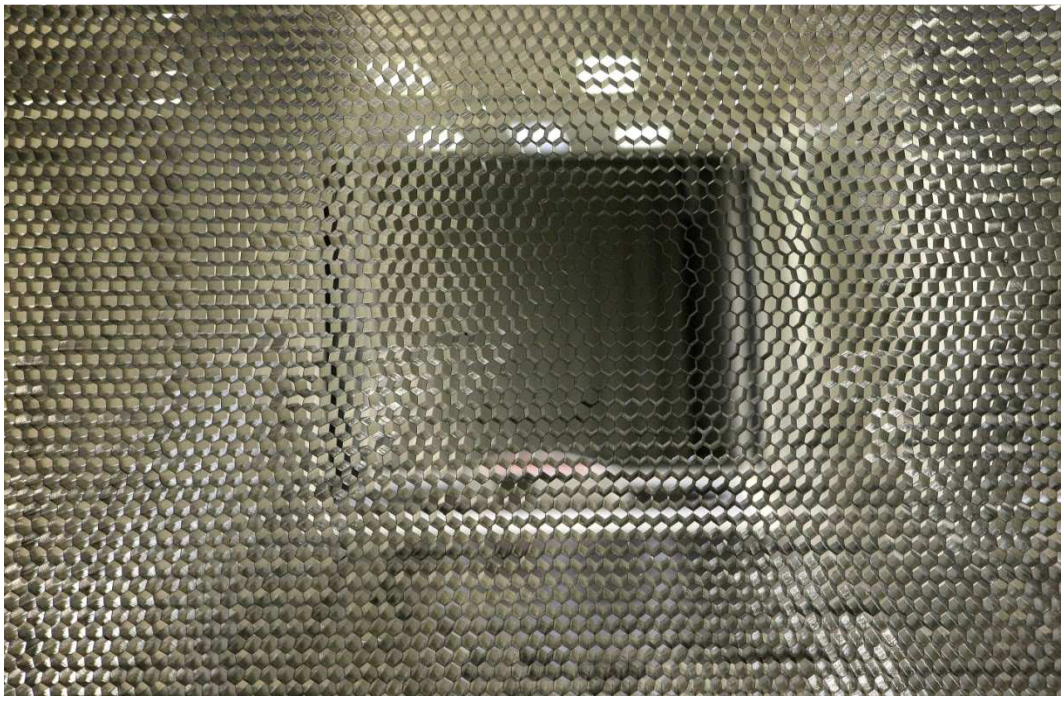

Figure 3.4 Honeycomb

The first 1.5 m of the aerodynamic section is a “flow-processing part”, [14], [17], [1] where it is possible to install flow-processing devices, such as spires, grids, barriers, etc. Further downstream, the next 7.0 m of aerodynamic section have roughness elements fetch for modeling and sustaining the ABL simulation. When no flow-processing devices are used, the walls, ceiling and floor of the flow-processing part are leveled with the rest of the aerodynamic section.

At the test section a vertically sliding door gives adequate access for installing models. The walls are equipped with a number of glass windows that make possible to observe experiments. A manually-controlled turntable is installed at the downstream position (Fig. 3.5).

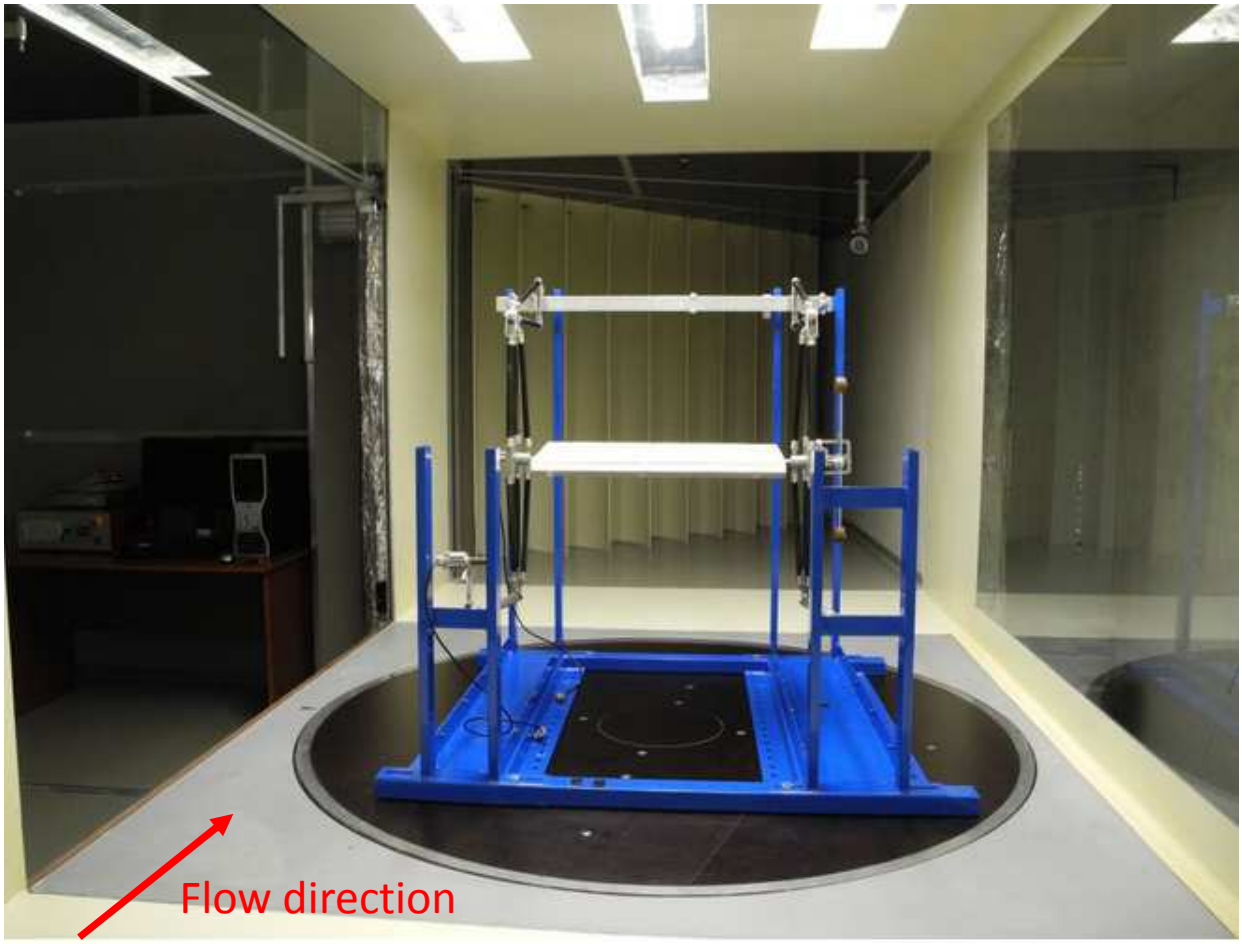

Figure 3.5 Turntable with the structure model in place

The test section continues into the return section. The return section has a rectangular cross-section with guiding vanes and connects the downstream end of the test section into a 180° turn, which gradually widens to the climatic section.

One of the commonly applied methods for the ABL simulation is the Counihan method. Accordingly the castellated barrier, vortex generators and floor roughness was used. The basic principles of this method are presented in Fig. 3.6.

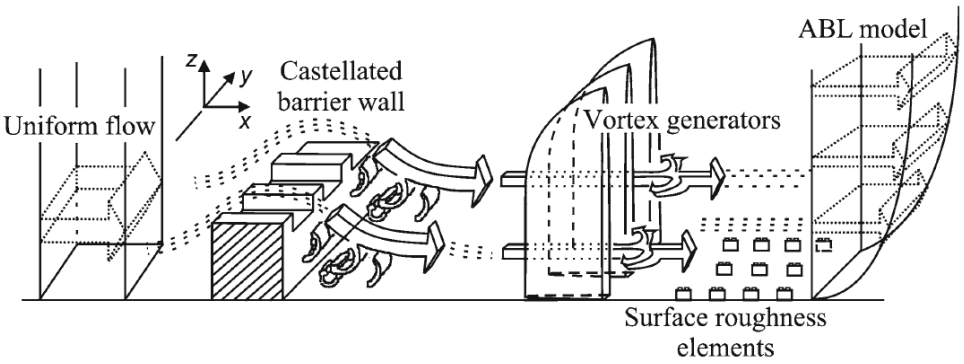

Figure 3.6 Basic principles of the ABL wind-tunnel simulation using the Counihan method [18]

The uniform flow coming out of the nozzle streams over the castellated barrier wall, which introduces large eddies and mean shear in the wake of the barrier. Vortices with vertical axes of rotation develop around vortex generators. Surface roughness elements provide the sustained formation of boundary layer structures downstream from vortex generators. The barrier used is shown together with the spire vortex generators in Fig. 3.7. and in detail in Fig. 3.8.

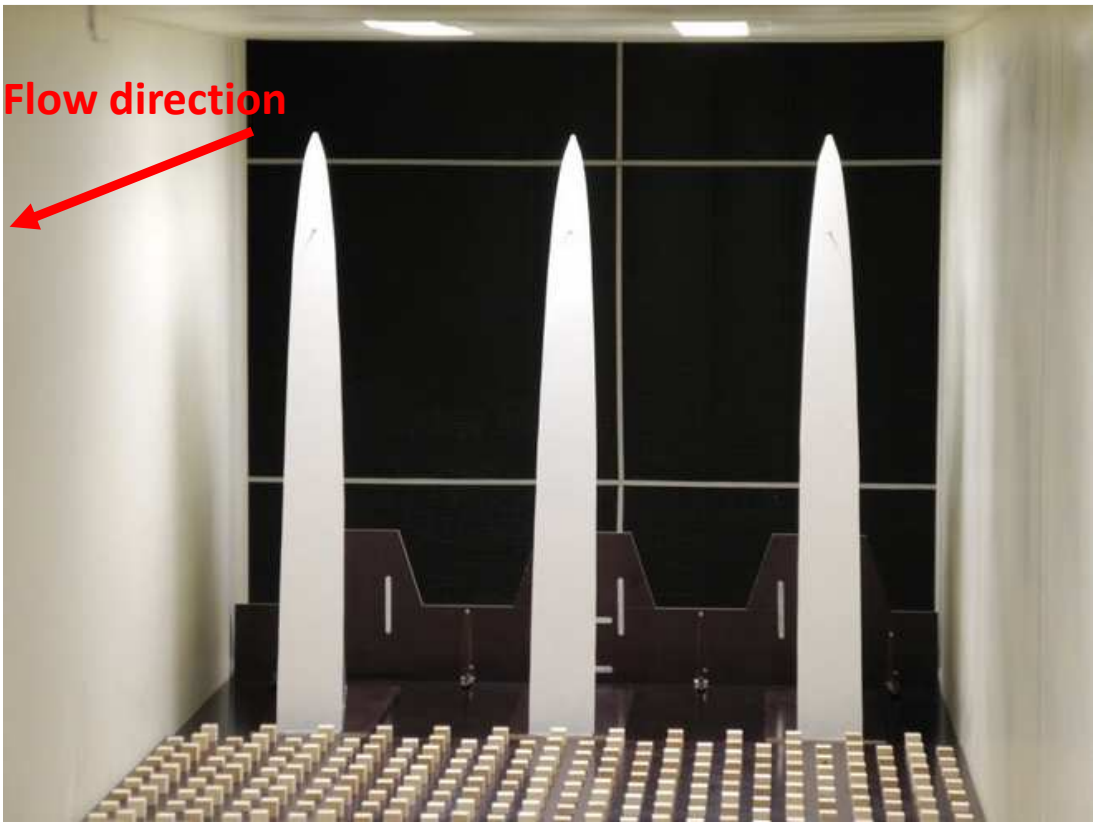

Figure 3.7 The barrier, the vortex generator spires, roughness fetch

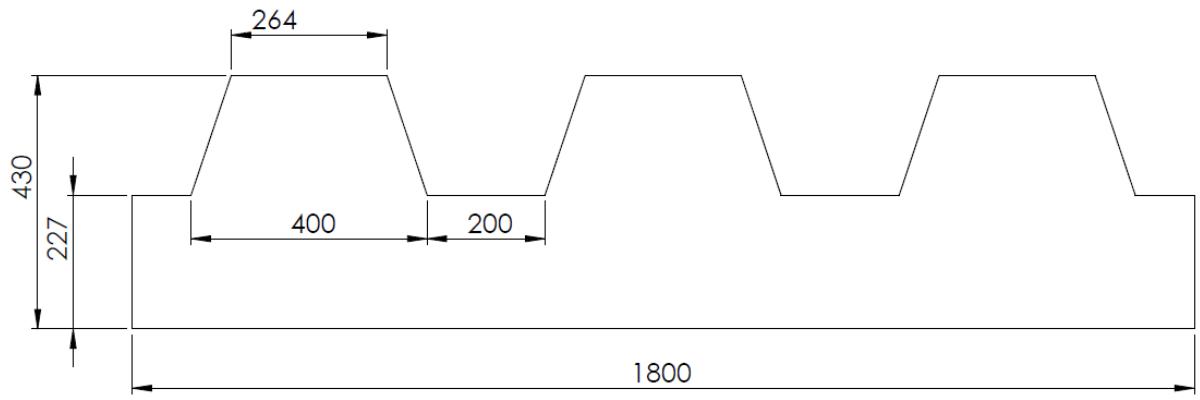

Figure 3.8 Castellated barrier wall, all dimensions in mm

Wooden cubes in a staggered pattern were used to create surface roughness (Fig. 3.9). Also, a new technique for generating the ABL simulation was tested in order to investigate if it could be used for future experiments. This method incorporates the use of a grid made out of 3 mm steel wire diameter. The grid is mounted at a height of 5 cm and spreads along the whole width of the wind tunnel (2 m) and all the way from the contraction downwind (8 m). An arrangement of the grid applied in the test is presented in Fig. 3.10.

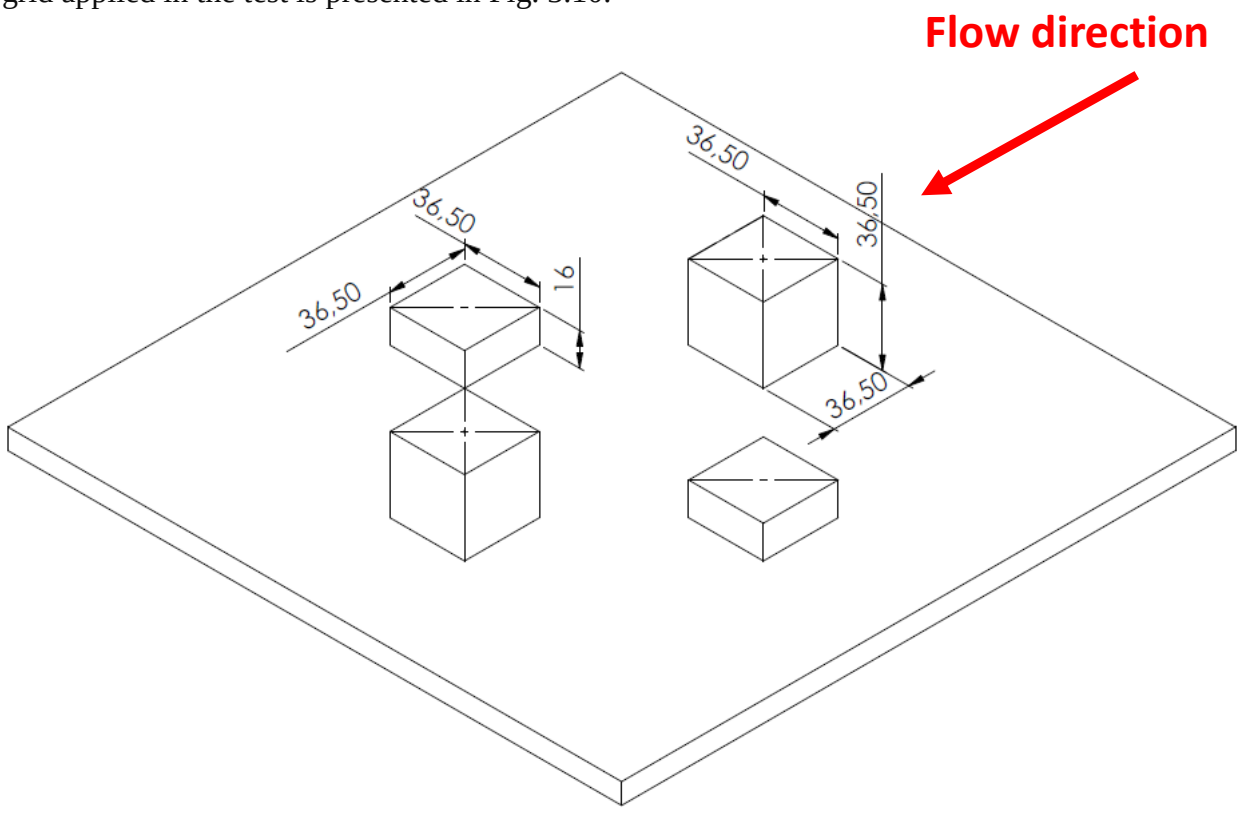

Figure 3.9 Roughness elements, all dimensions in mm

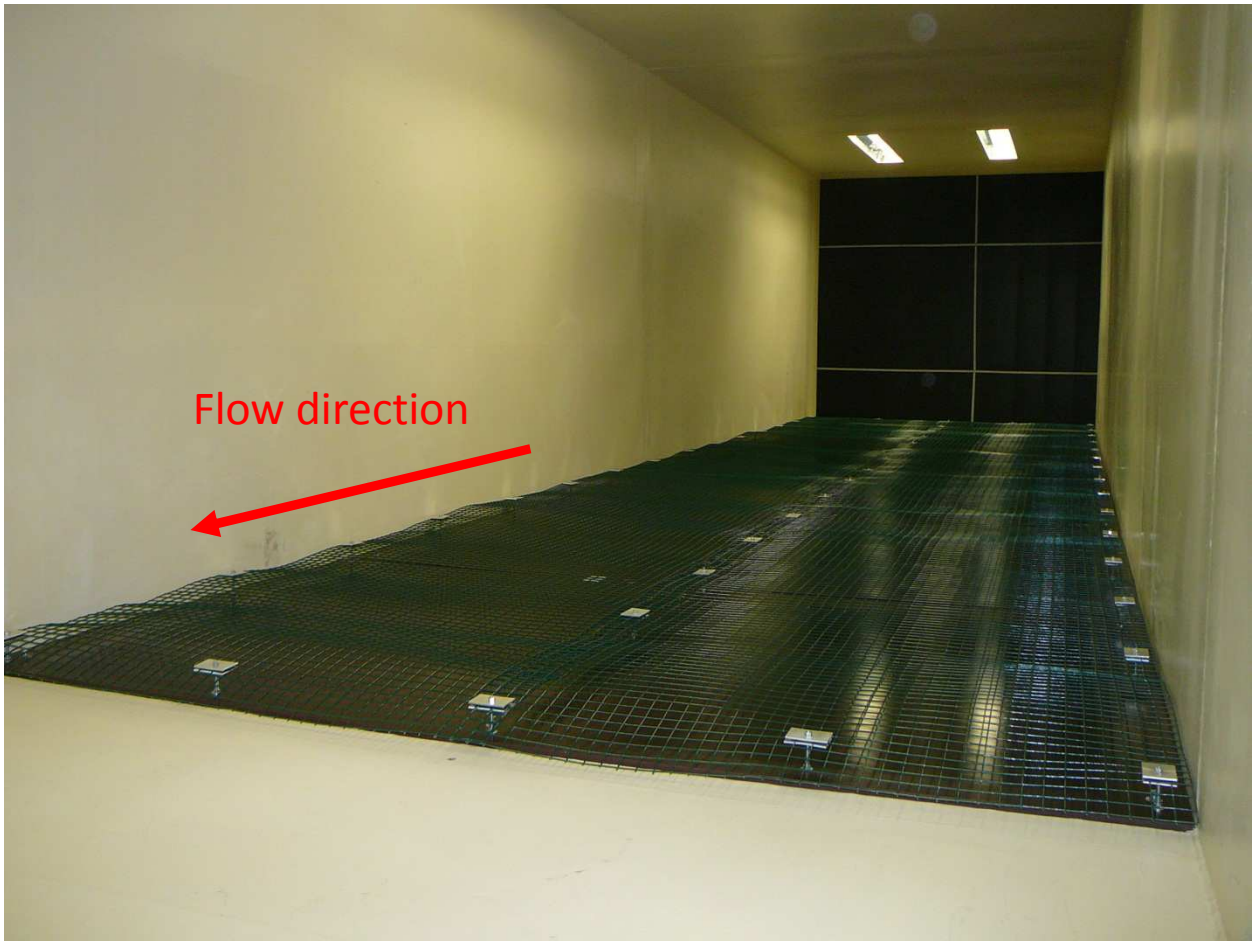

Figure 3.10 Grid as a turbulence generator

3.2. Climatic section

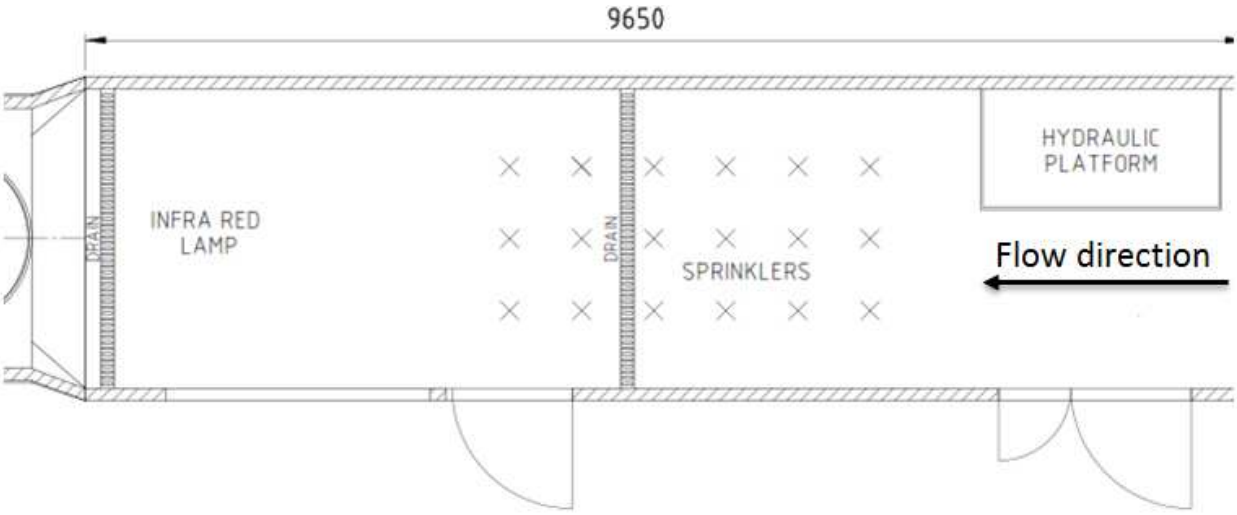

Figure 3.11 Scheme of the climatic section

The climatic section (Fig. 3.11) has a rectangular 2.5 m wide, 4 m high and 9 m long cross-section with a sudden widening at the outlet of the return section. The cross-section can be adjusted by a vertically moveable ceiling. It also enables the placing of the system for solar radiation simulation (Fig. 3.12). The capabilities of the four infrared lamps are: maximal power 8 kW, and maximal incidence 20° to the floor, the maximal intensity of solar radiation is 1.4 kW/m^2. The power and radiation intensity is regulated in full extent and, if needed, only one lamp can be in operation. The rain simulation system is located at the return section exit and consists of an array of up to twelve sprinklers of various size as needed to provide adequate coverage of testing structural models (Fig. 3.13). Raindrops diameter ranges from 0.1 to 9 mm with a possibility to create cloud droplets. Intensity of rainfall is over 50 mm per hour. The system is designed for 15 m/s at 20°C but will operate as low as –5°C to perform freezing rain tests.

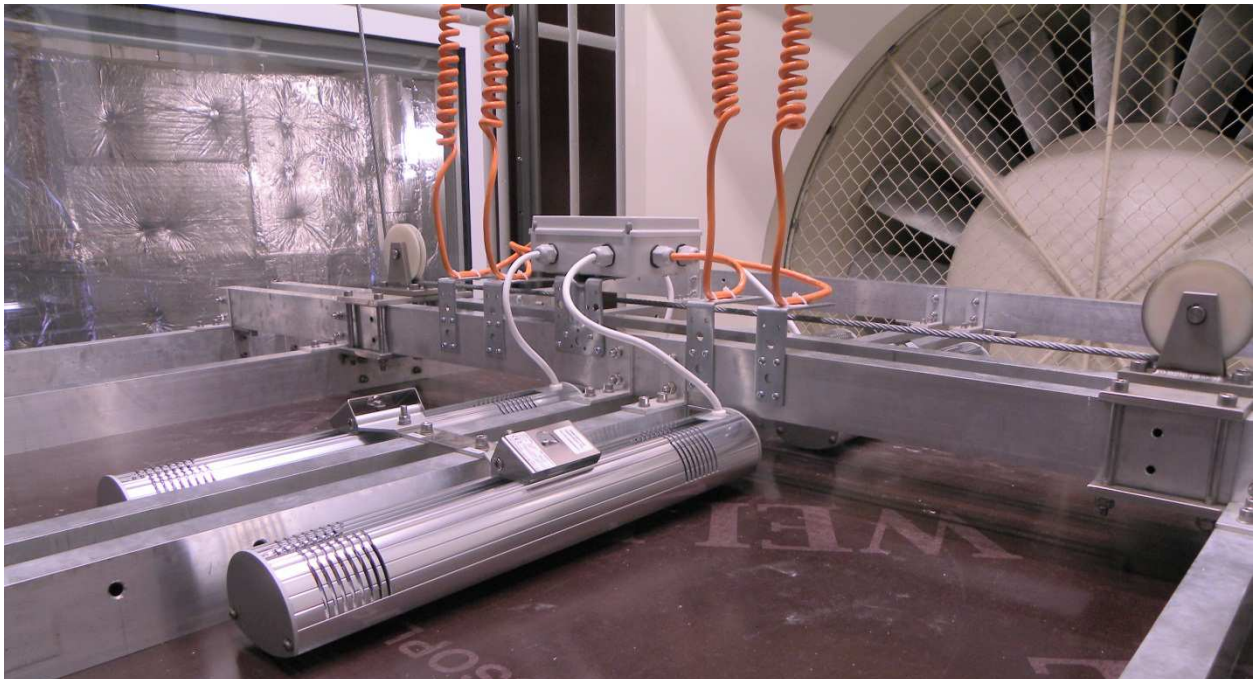

Figure 3.12 Climatic section with the Infra-Red Lamps

Figure 3.13 Climatic section with water sprinklers

3.3. Fan

The fan (Fig. 3.14) is made by ZVVZ Milevsko and it is equipped with a 200 kW motor. The flow rate through the tunnel is controlled by changing the rotation frequency of eighteen fan blades. The fan itself is a large axial variable revolution fan (diameter 2.0 m) that can create stationary wind flow. The fan is connected to the upstream and downstream diffusers with a flexible PVC joint so that static and dynamic loads cannot be transmitted from the fan to the duct. A highly porous safety screen is placed at the end of the contraction to prevent model parts entering the fan and damaging it in a case of model failure. The cooling system is placed outside of the tunnel. The fan is cooled by the fresh air from outside which is than exhausted into the tunnel.

Figure 3.14 Fan

3.4. Heat exchanger

After the fan exit section a large 3 m wide and 2.5 m high heat exchanger is mounted with the maximum heating power of 77 kW. The heat containers, as well as the pumps and power units are placed outside the wind-tunnel. When needed the heat exchanger can be operated from the main wind-tunnel control unit.

3.5. Traversing system

The tunnel is equipped with a DANTEC traversing mechanism (Fig. 3.15). The design is based upon the principles of traversing systems used for Laser Doppler Anemometry equipment. The mechanism can be controlled manually or remotely from the computer and is able to move 660 mm in lateral and 660 mm in vertical direction. It is currently a work in progress to improve the mechanism by mounting it on an external pair of rails inside the tunnel walls where it would be positioned manually.

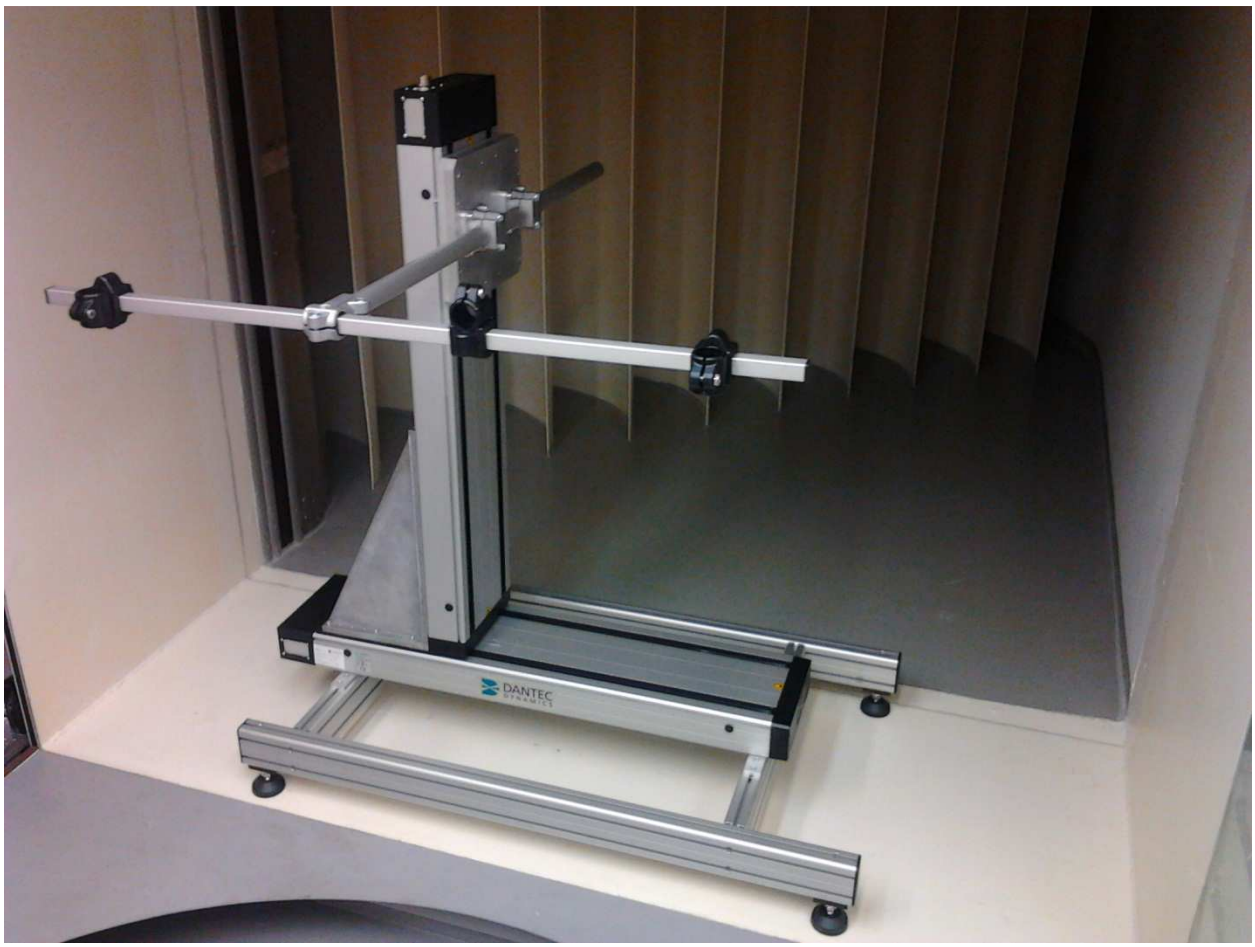

Figure 3.15 Traverse system

4. MEASUREMENT INSTRUMENTS

4.1. Manometer

The arrangement of the U-tube manometer is shown in Fig. 5.1. The manometer is acted upon by a pressure p_1 on the left and p_2 on the right. If $p_1 > p_2$, the fluid in the left leg of the manometer will be displaced to the right by a volume of $z_1 A_1$, resulting in an increase of volume of $z_2 A_2$ in the right leg. Application of equation (4.1) for equilibrium in the U-tube manometer results in the following:

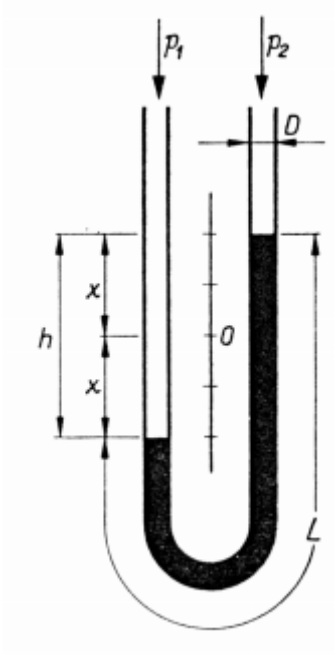

Figure 4.1 U-manometer scheme [19]

$$(p_1 - p_2) = \Delta p = \gamma_m h, \qquad (4.1)$$

$$p_1 + \gamma_f (z_1 + z_2) = p_2 + \gamma_m (z_1 + z_2)\,, \qquad (4.2)$$

which reduces to $$(p_1 - p_2) = (\gamma_m - \gamma_f)(z_1 + z_2) = \left(\gamma_m - \gamma_f\right) h\,. \qquad (4.3)$$

In these equations, γ_m is the specific weight of the manometer liquid and γ_f is the specific weight of the flow.

One of the disadvantages of the U-tube manometer is that unless $A_1 = A_2$, both legs must be observed simultaneously. The height difference should be calculated of both tubs change in these cases. A zero point of sliding scale needs to be set on the liquid level before every experiment.

The sensitivity of U-tube manometer is a ratio of a height difference increment to a pressure increment - $dh/d(p_1 - p_2)$. The sensitivity increases with decreasing density of a liquid. The absolute measurement error of liquid height is 0.5 – 1.0 mm.

The U-tube manometer is used as a primary device which does not need calibration from another device. The temperature correction is considered as well. The true liquid height is determined using the density at the temperature t_0 according to the following equation:

$$h_{true} = h_t \frac{\gamma_t}{\gamma_{t_0}}, \quad (4.4)$$

where subscript *t* implies measurements at temperature or in a different form:

$$h_{true} = h_t \frac{1}{1+\propto_V (t-t_0)}, \quad (4.5)$$

where α_V is volume expansion coefficient of liquid.

4.2. Pitot-static tube

The Pitot static tube is a primary and commonly used instrument in wind engineering applications which measures a fluid velocity by converting the kinetic energy of the flow into potential energy. The conversion takes place at the stagnation point, located at the Pitot tube inlet with the prevailing total pressure p_t. At a distance from the entrance, at a several equally spaced circumference holes the static pressure p_s is measured. According to the Bernoulli's equation the difference between the total and static pressure is the dynamic pressure p_d ,

$$p_t - p_s = p_d. \quad (4.6)$$

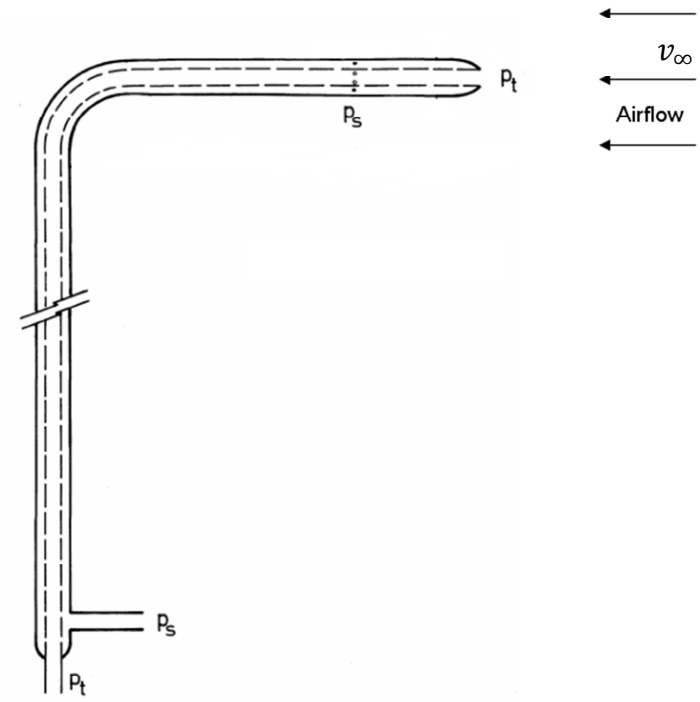

Figure 4.2 Schematic view of the static Pitot tube

Converting the resulting dynamic pressure measurement into a fluid velocity depends on the particular fluid flow regime the Pitot tube is measuring. Within the scope of this research the flow is considered to be incompressible. Evaluated at two different points along a streamline the Bernoulli equation yields,

$$\frac{v_\infty^2}{2g} + z_{1+}\frac{p_s}{\rho g} = \frac{v_2^2}{2g} + z_{2+}\frac{p_t}{\rho g}. \qquad (4.7)$$

If $z_1 = z_2$ and point 2 is a stagnation point, i.e., $v_2 = 0$, the above equation reduces to,

$$\frac{v_\infty^2}{2} + \frac{p_s}{\rho} = \frac{p_t}{\rho}. \qquad (4.8)$$

The freestream velocity v_∞ equals then,

$$v_\infty = \sqrt{\frac{2(p_t - p_s)}{\rho}}. \qquad (4.9)$$

The p_t and p_s are measured either via the differential manometer or a pressure transducer. As $\rho=f(\varphi, \upsilon)$ the needed air states φ – relative air humidity, υ – air temperature are also measured and used for corrections.

At the ceiling of the wind-tunnel, at the centreline a one reference static Pitot tube is installed. The pressures are measured by a Scanivalve pressure sensor and automatically recalculated into velocity shown at a wind-tunnel control unit as a part of a graphical user interface.

The sensor is calibrated by using the U-manometer. A certain pressure is set manually by a syringe. Then, the pressured lines are closed and tightly sealed and the pressure height on the manometer is read. The corresponding velocity shown on the monitor is then documented. The procedure is repeated. Finally, in correspondence with the air conditions, the temperature and humidity measured during the calibration, the calibration coefficients are then inputted in the system.

4.3. Pressure transducer

A transducer is a device that converts one type of a signal into another one. A pressure transducer, also called a pressure transmitter, is a transducer that converts pressure into an analog electrical signal.

At the wind-tunnel there are two Scanivalve DSA 3217 pressure transducers (Fig. 4.3). The DSA stands for Digital Sensor Array, which is a standalone temperature compensated electronic pressure scanner which can work with maximum 16 pneumatic inputs. Each Digital Sensor Array incorporates 16 individual, temperature compensated, piezoresistive pressure sensors with an A/D converter and a microprocessor to create an intelligent pressure scanner. Each pressure sensor is characterized for pressure and temperature from 0 to 69 ºC . This information is stored in EEPROM memory in the module. The DSA 3217 sensors are arranged in blocks of eight. Each block of eight sensors has its own individual calibration valve. The 16 channel module with individual references can work as an 8 channel “true differential” model, and a 16 channel absolute model.

All data acquisition, data conversion and communications tasks are handled by the integrated A/D converters and processor. Once processed, the DSA outputs the data in either ASCII or Binary format over the Ethernet network TCP/IP or UDP in this specific case to a router and then over WiFi to the Dewetron computer unit. Dewesoft X software is used for analyzing, processing and exporting data.

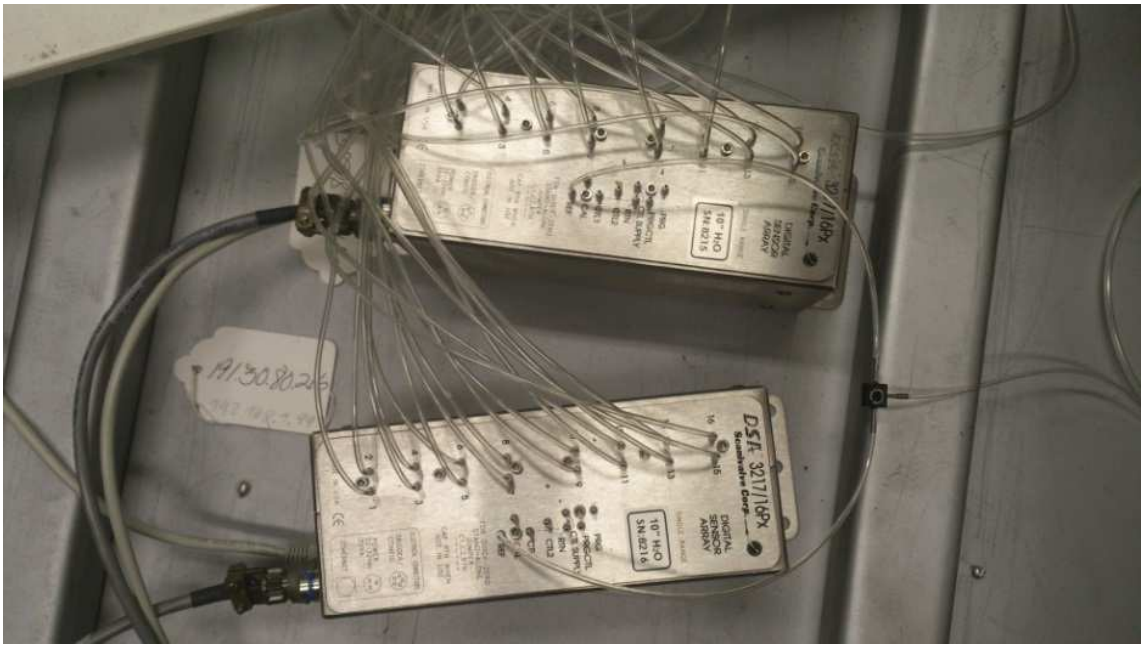

Figure 4.3 Scanivalve DSA 3217

4.4. Hot-wire anemometer

Hot-wire anemometry was used for velocity measurements in this study. In general it can be used for measuring a wide range of wind speeds from low subsonic to high supersonic flows. This method is capable of detecting turbulent perturbations with a large dynamic response because of the very small hot-wire thermal inertia and its correction in the anemometer.

The method relies on the changes in heat transfer from a small heated sensor exposed to the fluid in motion. The sensor is made with a material whose electric resistivity depends on the temperature. It usually has the shape of a small cylindrical wire or a thin film. Anemometer probes are available with four types of sensors: Miniature wires, Gold-plated wires, Fibre-film or Film-sensors (Fig. 4.4).

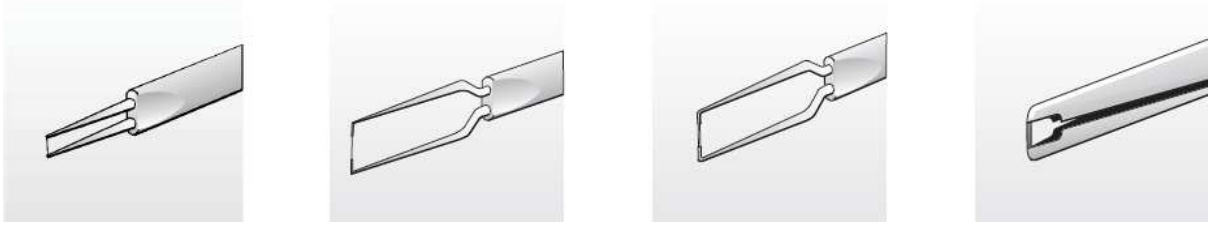

Figure 4.4 : Miniature wires, Gold-plated wires, Fibre-film or Film-sensors [20]

Wires are normally 5 µm in diameter and 1.2 mm long suspended between two needle-shaped prongs. Gold-plated wires have the same active length but are copper- and gold-plated at the ends to a total length of 3 mm in order to minimize prong interference. Fibre-sensors are quartz-fibers, normally 70 µm in diameter and with 1.2 mm active length, covered by a nickel thin-film, which again is protected by a quartz coating. Fibre-sensors are mounted on prongs in the same arrays as the wires. Film sensors consist of nickel thin-films deposited on the tip of aerodynamically shaped bodies, wedges or cones.

Depending on the designated number of velocity vector components, there are probes available in one-, two- and three-dimensional versions as single-, dual and triple sensor probes referring to the number of sensors (Fig 4.5) Since the sensors (wires or fibre-films) respond to both magnitude and direction of the velocity vector, information about both can be obtained, only when two or more sensors are placed under different angles to the flow vector.

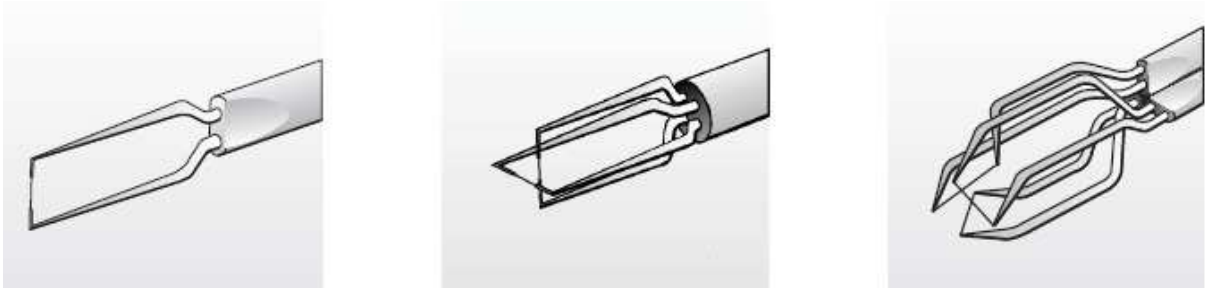

Figure 4.5 One-, two- and three-dimensional sensors [20]

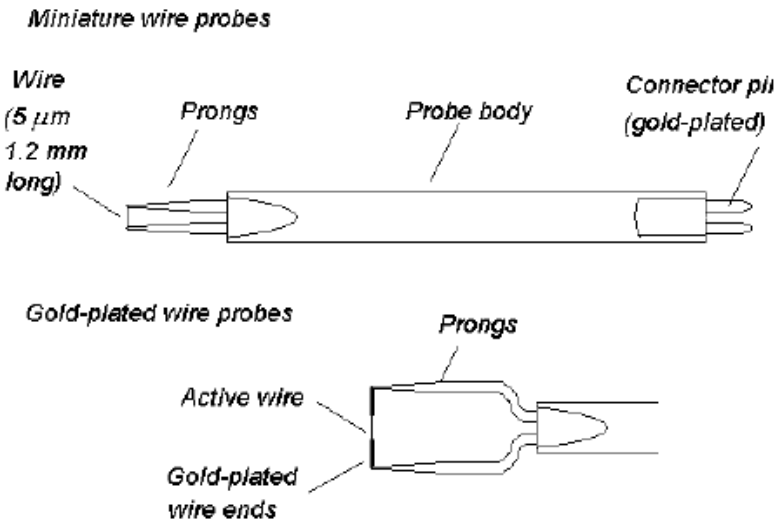

Figure 4.6 Hot-wire design [20]

Heat is introduced in the sensor by Joule heating, and is lost primarily by forced convection. The heating rate is $R_w I^2_w$, where I_w is the current intensity in the sensor and R_w the sensor resistance when heated. The cooling rate is of the form $(T_w - T_a)\phi_{conv}(U \ldots)$, where T_w is the temperature of the wire when heated, and T_a is the temperature of the wire at the same location when unheated. The heat convection function ϕ_{conv} $(U \ldots)$ mainly depends on the fluid velocity normal to the wire.

For a steady flow, the heat balance between the heating and the cooling rates has the simple form

$$R_w I^2_w = (T_w - T_a)\Phi conv(u), \qquad (4.10)$$

The velocity u can be deduced from the electrical quantities R_w and I_w, if T_w can be related to R_w and similarly T_a to R_a, where R_a is the resistance of the unheated sensor. Such relations exist for most sensors.

A significant parameter that controls the operation of the sensor is the relative difference in temperature, $(T_w - T_a)/T_a$, or the relative difference in resistance, $(R_w - R_a)/R_a$. It is simply denoted α_w and called the overheat ratio of the sensor,

$$\alpha_w = \frac{R_w - R_a}{R_a} \qquad (4.11)$$

For a turbulentflow, thermal energy is unsteadily stored in the sensor, and the instantaneous heat balance becomes:

$$m_w c_w \frac{dT_w}{dt} = R_w {I_w}^2 - (T_w - T_a)\Phi conv(U) \qquad (4.12)$$

where m_w is the mass of the sensor and c_w is the specific heat of the sensor material.

When the sensor is an element of an appropriate electrical system, the change in resistance can be used to generate a measurable signal. Three operating modes are possible:

a) The current intensity in the sensor is maintained constant, I_w = constant, as used in the constant current anemometer (CCA). Any change of U creates a change in R_w and the measurable signal is in accordance with this resistance change.

b) The resistance of the sensor is maintained constant, R_w = a constant, as used in the constant resistance anemometer, usually called a constant temperature anemometer (CTA). The measurable signal when a change in U occurs is then the change in current intensity I_w to be fed to the sensor to fulfill the imposed condition.

c) The voltage across the sensor is maintained constant, $V_w = R_w I_w$ = constant, as used in the constant voltage anemometer (CVA). The measurable signal is then the change in current intensity I_w to be fed to the sensor under that new imposed condition.

The main difference between these three operating modes is linked to the handling of thermal inertia of the sensor. In usual applications, the frequencies of the flow fluctuations to be measured are much higher than the natural frequency of the sensor, so that electronic compensation is needed. In a CCA and CVA, this is achieved by a first-order high-pass filter integrated in the amplifying unit. In a typical CCA application, the filter response is tuned to compensate exactly the thermal lag of the sensor. In that case the overall bandwidth is then only

limited by the amplifier characteristics, mainly its gain–bandwidth product. With a CVA, the thermal lag is partially compensated during measurements and is fully compensated when postprocessing the data. This permits high productivity for large-bandwidth applications because no adjustment is required when the experiment is running. In a CTA, the temperature of the sensor is maintained constant by a feedback loop, so that its thermal inertia is, in principle, automatically compensated. In this case, the maximum bandwidth is limited by the amplifier properties and some characteristics of the practical setup. In the scope of this research a CTA system was used.

In a constant temperature anemometer system the resistance of the sensor is maintained constant, R_w = constant. The measurable signal when a change in U occurs is then the change in current intensity I_w to be fed to the sensor to fulfill the imposed condition. The constant temperature anemometer is designed with the purpose of eliminating the influence of the thermal inertia of the wire in fluctuating flows, so that the frequency limit of the instrument is mainly determined by the electronic circuitry. This is achieved by supplying electrical energy to the wire at exactly the same rate as heat is lost to the surrounding fluid medium. Since the wire temperature is thus kept constant irrespective of the flow velocity, the importance of the heat capacitance of the wire is greatly diminished. The operation of the CTA anemometer can be explained as follows (Fig. 4.7):

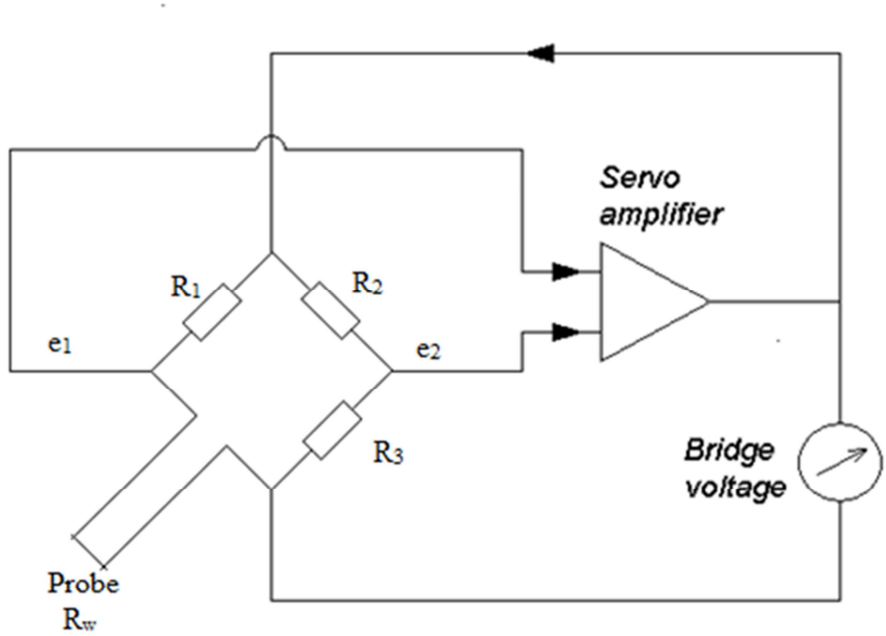

Figure 4.7 Schematic view of the constant temperature anemometry electric circle [20]

The hot-wire probe, R_w is placed in one arm of the Wheatstone bridge opposite a variable resistor R_2 which defines the operating resistance, and hence the operating temperature of the hot-wire. A servo amplifier keeps the bridge in balance by controlling the current to the sensor so that the resistance - and hence temperature - is kept constant, independent of the cooling imposed by the fluid. The bridge voltage, *U*, represents the heat transfer and is thus a direct measure of the velocity. As all resistances in the bridge are constant, the squared output voltage *E* directly represents the heat transfer from the wire and can replace *Q* in the heat transfer equation for the wire and is thus a direct measure of the velocity *u=f(E):*

$$u = \left(\frac{E^2}{B} - \frac{A(T_w - T_0)}{B}\right)^{\frac{1}{n}} \qquad (4.13)$$

The CTA is only one part of the whole measuring chain (Fig. 4.8):

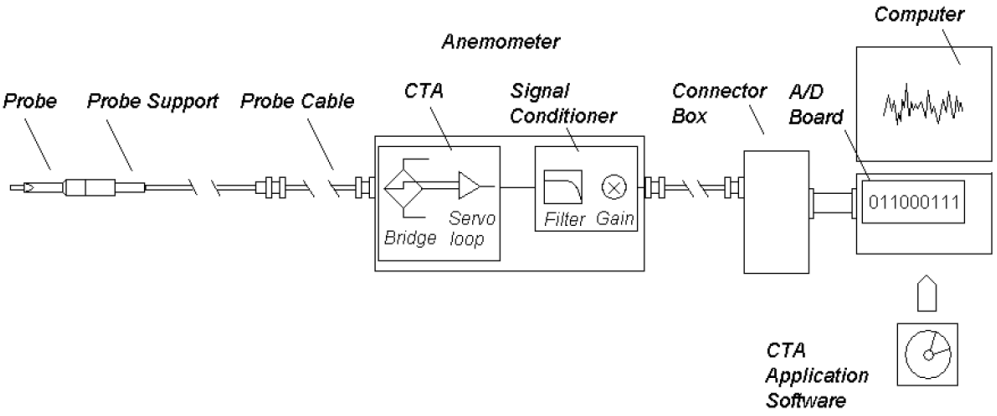

Figure 4.8 Measuring chain of the constant temperature anemometry [20]

The measuring chain consists of a probe with probe support and cabling, a CTA anemometer, a signal conditioner, an A/D converter, and a computer with pplication software for CTA set-up, data acquisition and data analysis. Signal Conditioner for high-pass and low-pass filtering and for amplification of the CTA signal is built in the CTA. The CTA signal is acquired via an A/D converter board and saved as data-series in a computer. Dedicated Stream Ware Pro software is used for time series acquisition and analysis.

As each of the probes has its unique resistance, calibration is needed for each probe. Calibration was carried out in the CET wind-tunnel. It was carried out twice, first for the probe cable length

of 5 m and later for 20 m long cables due to a need for longer cables. The procedure was, however, the same.

Two hot wire probes were placed in an empty test section, in the proximity of the Pitot static tube. However, the tip of all the probes was at least 2 cm apart in order to mitigate the influence of the flow around the Pitot static tube. The probes were installed at a distance x = 1.5 m from the turntable, in the middle of the tunnel y = 0 m, at z = 1.6m.

Then, the fan rotational frequency was increased in steps of 5% and the measured values recorded for each operating point. The voltage output values of the CTA system were recorded via the StreamWare Pro interface with the sampling frequency of 1000 Hz in 20 s long sampling intervals. The response of the Pitot tube was recorded via the DewetronDewesoft X software with sampling frequency of the pressure transducer 500 Hz and sampling time of 20 s. The corresponding calibration tables with acquired values were made and inputted in the CTA system (Figs. 4.9 and 4.10).

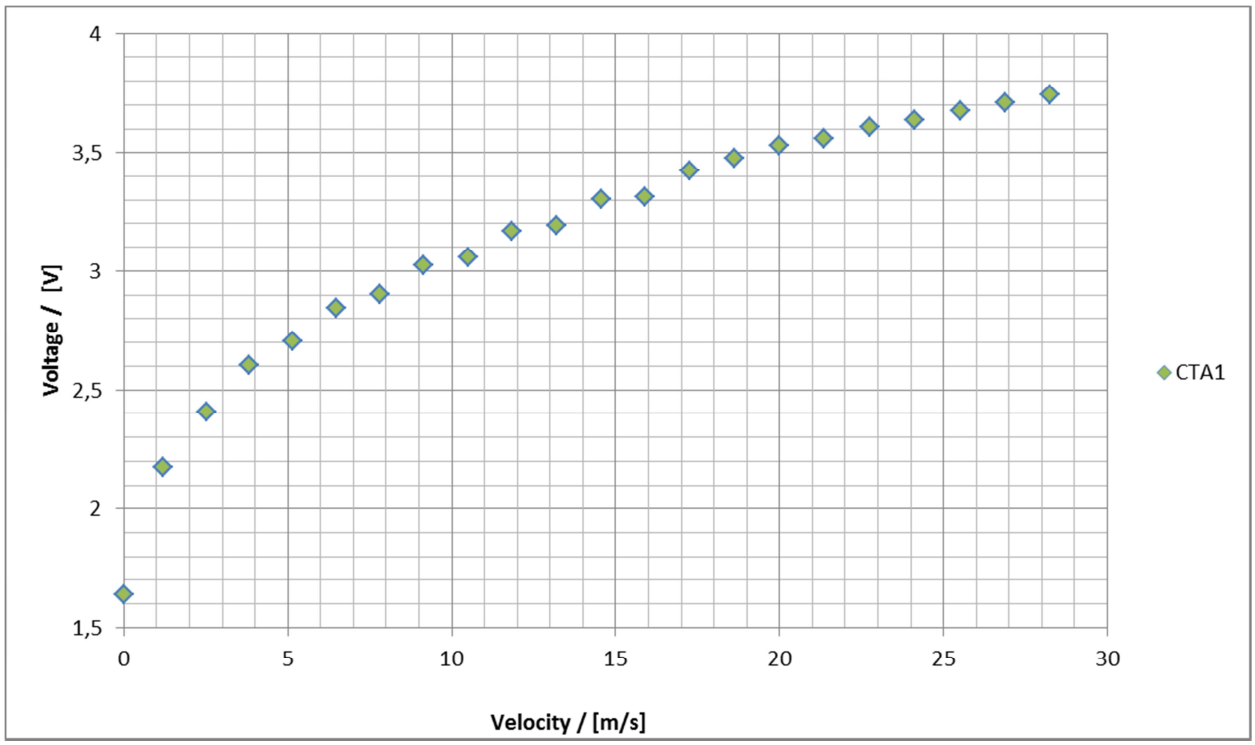

Figure 4.9 Calibration curve of the constant temperature anemometry probe 1

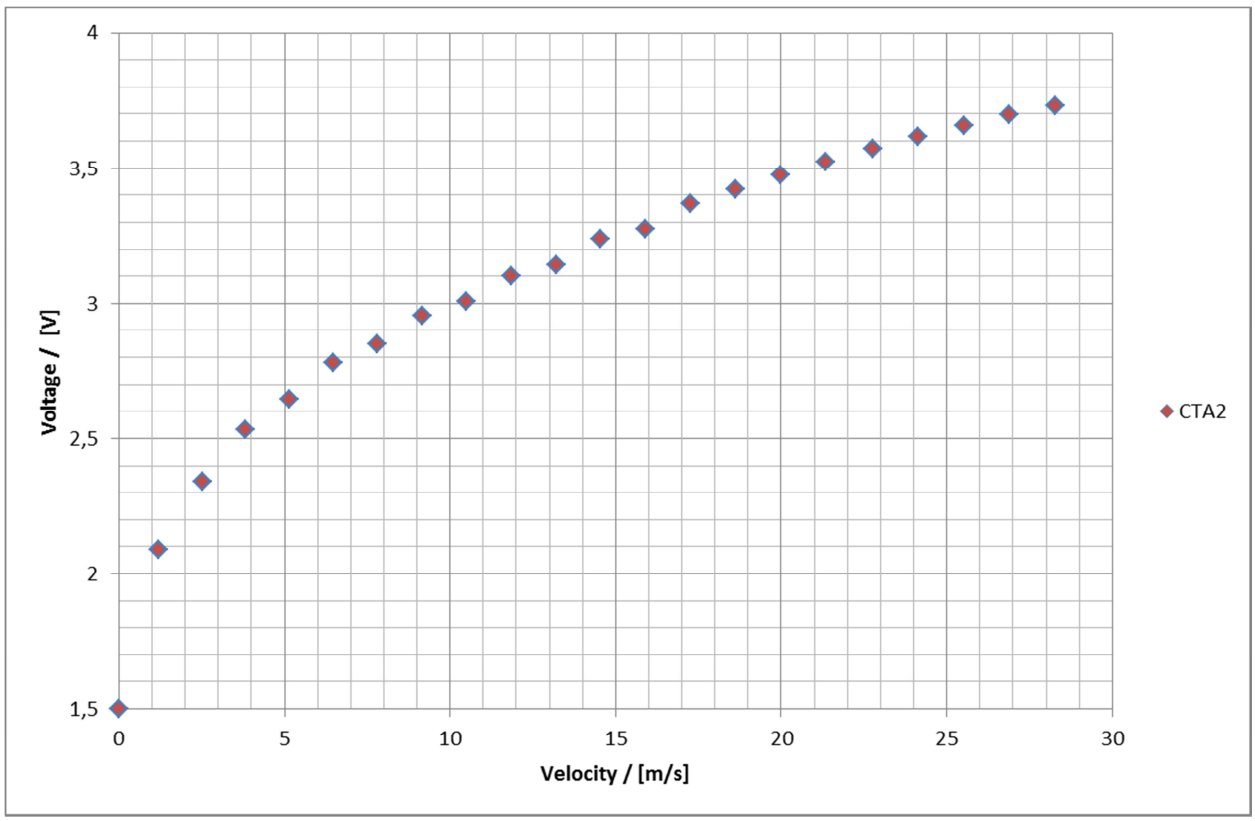

Figure 4.10 Calibration curve of the constant temperature anemometry probe 2

5. EXPERIMENTAL SETUP

5.1. Coordinate system

The aerodynamic section origin point is located at the center of the turntable. The longitudinal axis *x* is oriented downstream, axis *y* lateral to the left when the observer would be facing downstream and axis *z* perpendicular to *x* and *y* pointing up (Fig. 5.1).

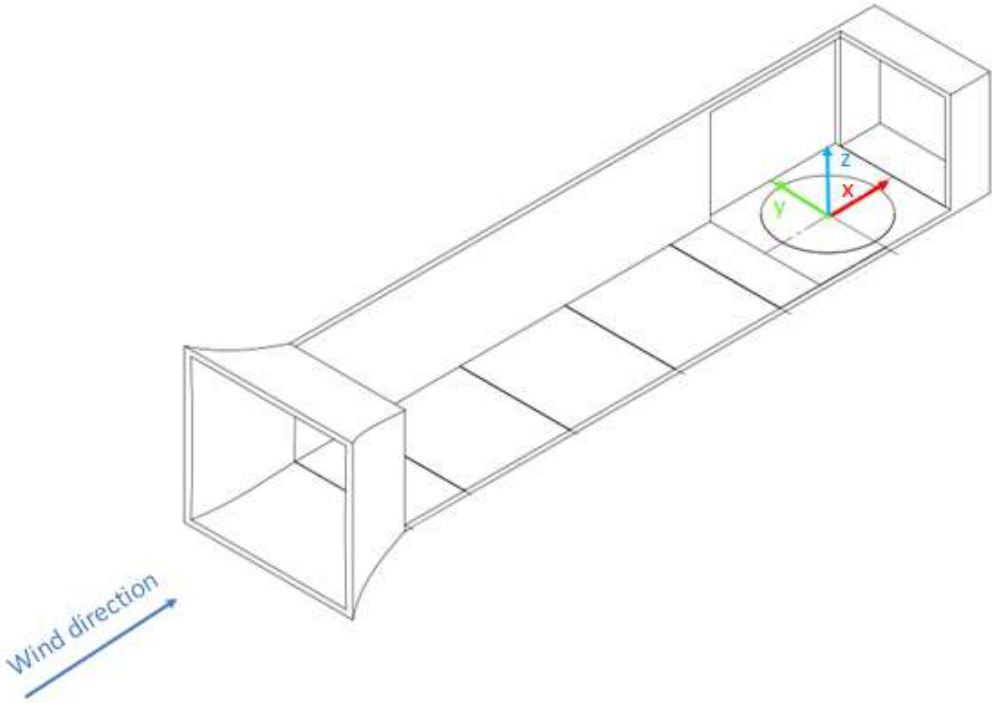

Figure 5.1 Aerodynamic section coordinate system

.

5.2. Velocity and turbulence measurements

Velocity, turbulence and profile measurements were carried out using the CTA measurement system. As 3D-probe was not available, the velocity and turbulence were measured only in the longitudinal *x* direction. At the arbitrary cross-section the hot-wire probe was installed on the traverse mounting point and connected to the CTA. A correcting temperature probe was also installed on the traverse and connected to the CTA system.

The reference probe was installed on the ceiling of the test section with the following coordinates: (*x*, *y*, *z*) = (1.5 m, 0 m, 1.6 m). Reference probe was needed for data normalization in order to provide a possibility to compare results obtained at different cross-sections. At each tested cross-section the CTA probe needed to be positioned manually due to the limited test volume of nine test planes as reported in Fig. 5.2. The traverse was then reset to a starting position at each corner of nine control planes. Two coordinate systems were used. In first the distances between the measured points were 100 mm in both *y* and *z* direction resulting in 36 points per one control plane. After nine experiments there were 324 points per cross-section. As there was overlapping and double measured points, the coordinate system was optimized. The second system incorporated 9 squares with 36 points each, in dimension 550mm by 500 mm, where the points were 110 mm apart in the *y* direction and 100mm in the *z* direction. The total number of points was also 324 but without overlapping and double measurements. The actuation of the traverse was controlled automatically via the Streamware Pro software.

Figure 5.2 Test matrix coordinate system, measures in mm

In experiments, the sampling frequency was 1000 Hz with sampling time 20 s which proved to give satisfactory results and repeatability while allowing for finishing experiments per one cross–section within one working day. The measurements were recorded via the Streamware Pro software.

The ABL simulations were carried out for different configurations of the experimental hardware i.e. vortex generators, castellated barrier wall and surface roughness. First the empty section was examined, then the ABL simulation configuration. And finally a test of a configuration using a metal fence grid. Due to the fact that the traverse is set on the floor only 2 sections were possible to be measured where the roughness elements are not present. All the configurations have 2 sections in common, a section at the turntable and a section 1.5 m upwind from the center of the turntable. An overview of the test configuration is given in table 5.1. A scheme of the placements of the examined sections for an empty section is shown in Fig. 5.3.

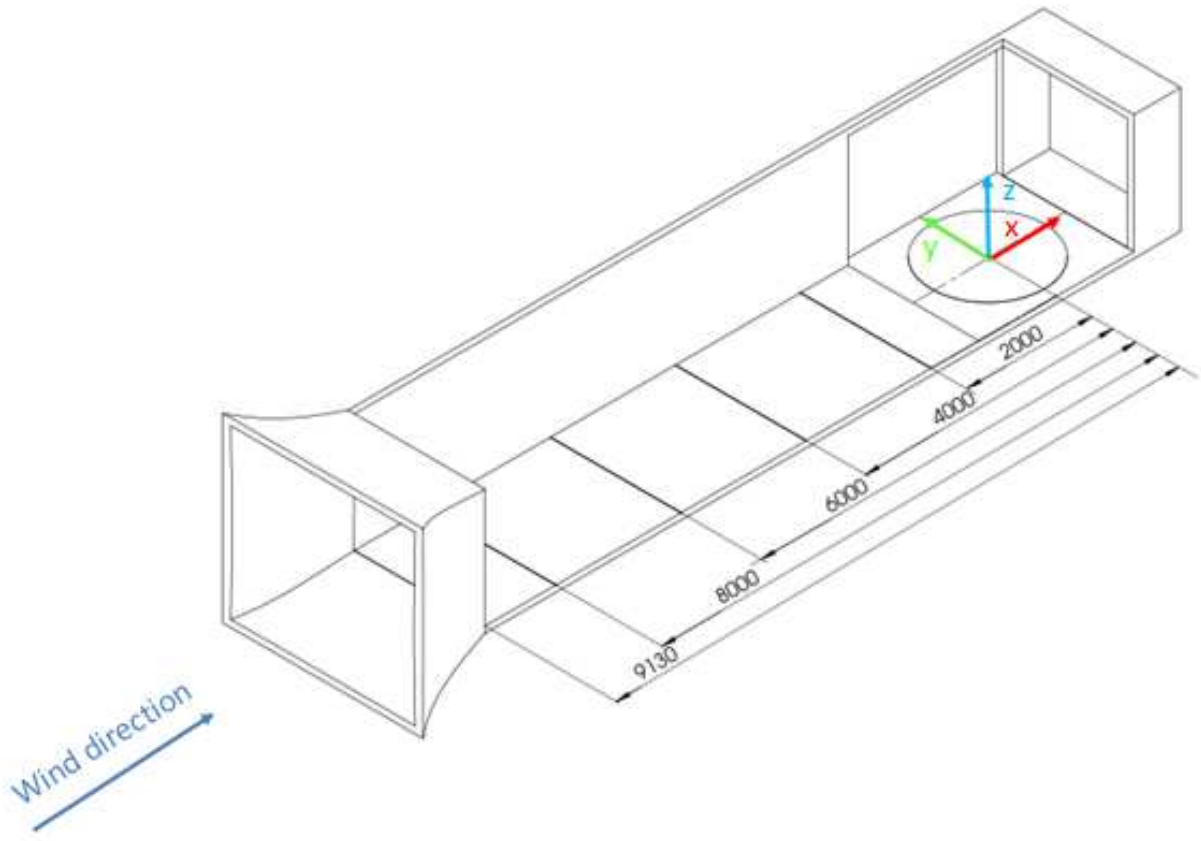

Figure 5.3 Positions of the examined crossections in a empty section

Table 5.1 Experimental setup configurations overview

Roughness	Description	Notes
R0	Empty test section	6 sections
R1	Roughness fetch elements	2 sections
Rn1	Grid height 1 cm	3 sections
Rn5	Grid height 5 cm	3 sections

6. RESULTS AND DISCUSSION

In this section the experimental results of the velocity measurements are reported in order to characterize flow and turbulence properties in the newly developed CET climatic wind-tunnel. Preliminary tests include results obtained for an empty wind-tunnel test section. Additional experiments were carried out in order to analyze characteristics of the atmospheric boundary layer simulation in this facility. The parameters used in the analysis of the experimental results are mean wind velocity and turbulence intensity.

6.1. Empty wind-tunnel test section

Results for flow and turbulence development along the test section (x-direction) are reported in Figs. 6.1 to 6.14. In particular, the u velocity mapping at different longitudinal positions of the test section are presented in Fig. 6.1, while all those diagrams are reported in a larger form in Figs. 6.3, 6.5, 6.7, 6.9, 6.11, 6.13. in order to allow for a more detailed analysis. Accordingly, obtained field values for I_u turbulence intensity at different longitudinal positions of the test section are presented cumulatively in Fig. 6.2, while those diagrams are reported in a larger form in Figs. 6.4, 6.6, 6.8, 6.10, 6.12, 6.14.

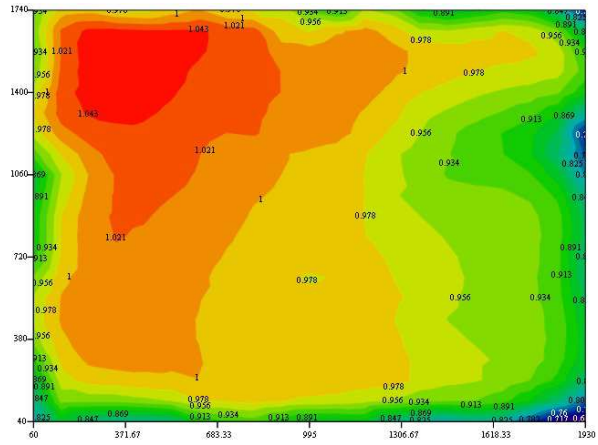

x = 0 m

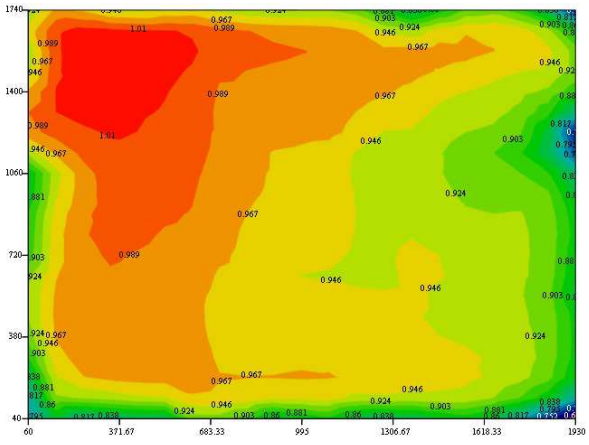

x = 2 m

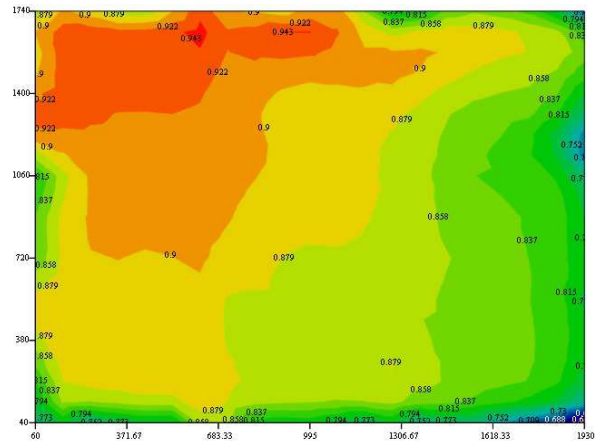

x = 4 m

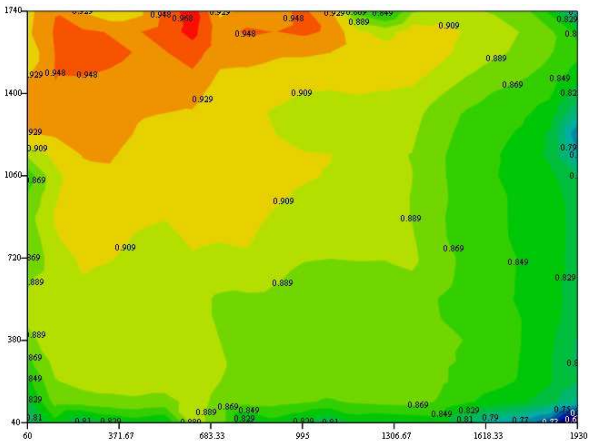

x = 6 m

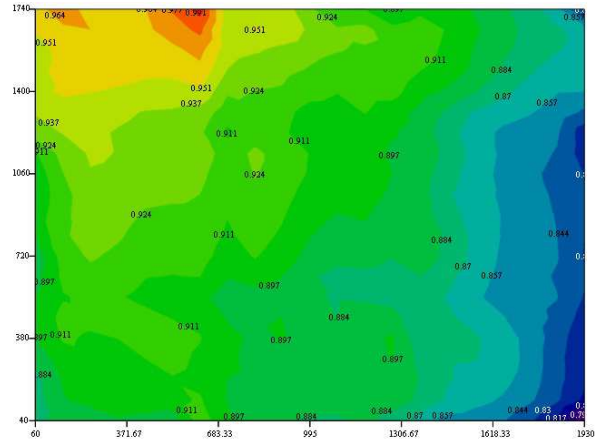

x = 8 m

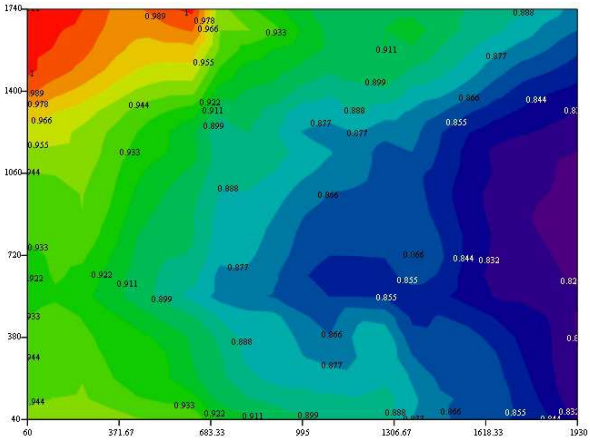

x = 9.3 m

Figure 6.1 Overview of the empty section velocity distribution

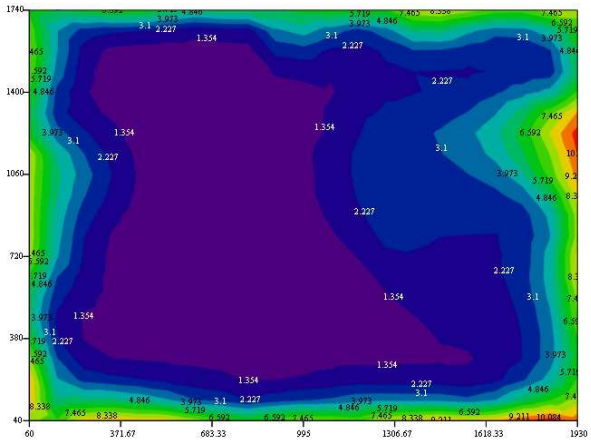

x = 0 m

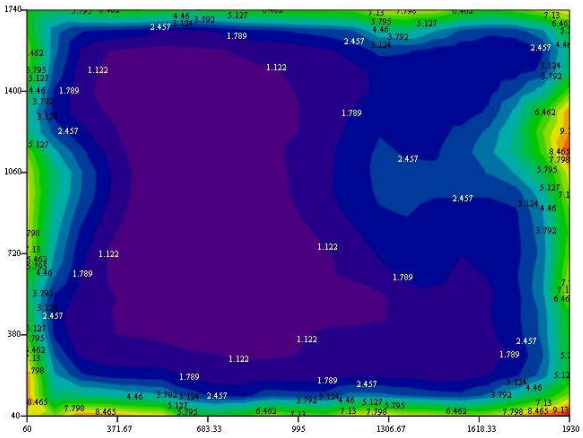

x = 2 m

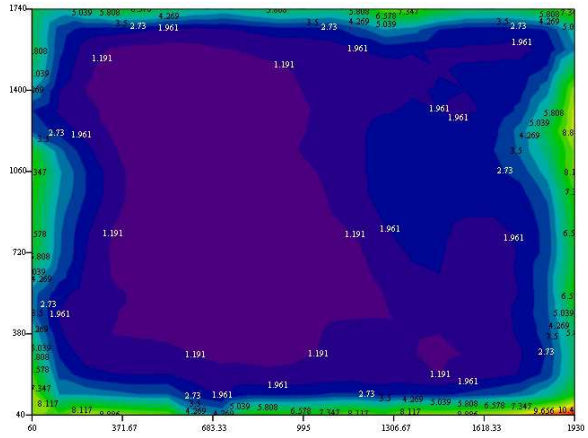

x = 4 m

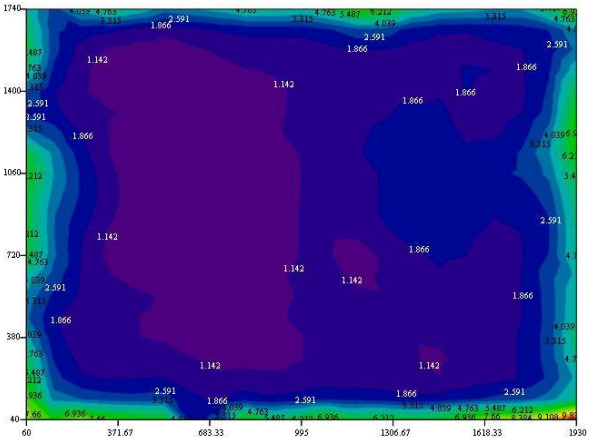

x = 6 m

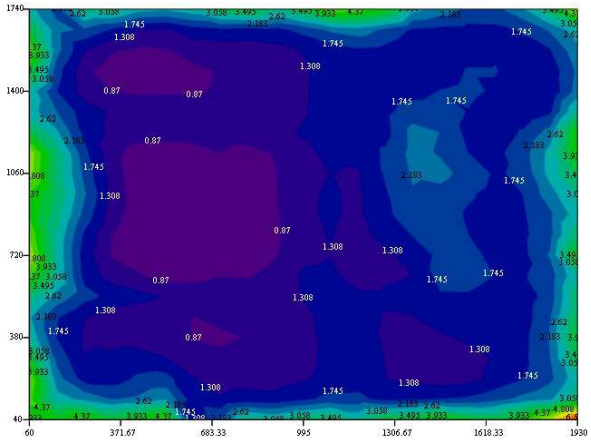

x = 8 m

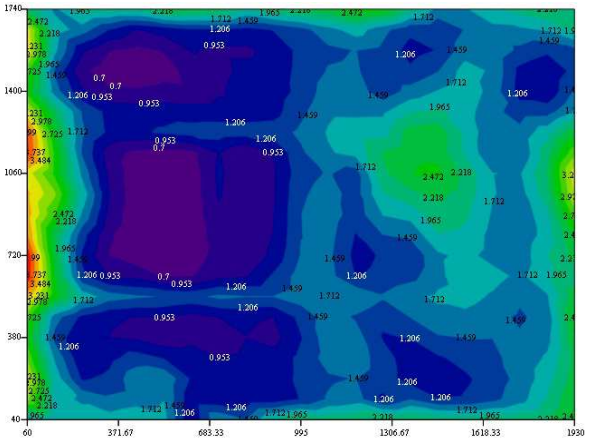

x = 9.3 m

Figure 6.2 Overview of the empty section turbulence intensity

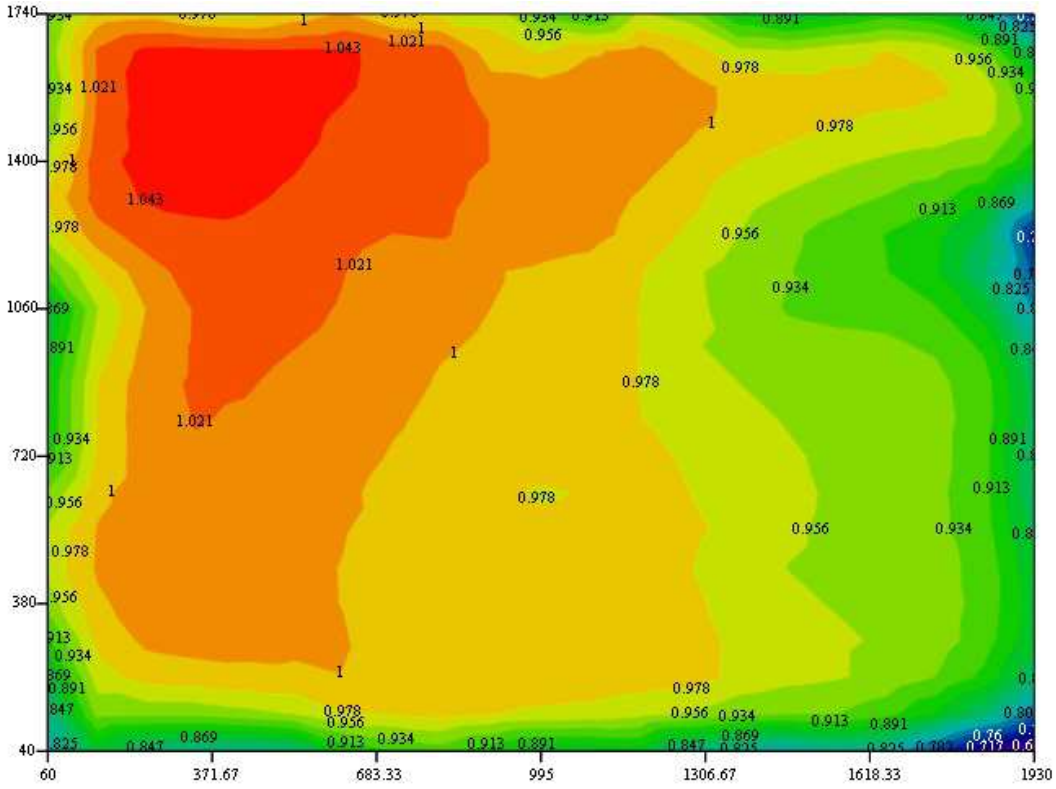

Figure 6.3 Velocity distribution for an empty section, position x = 0 m

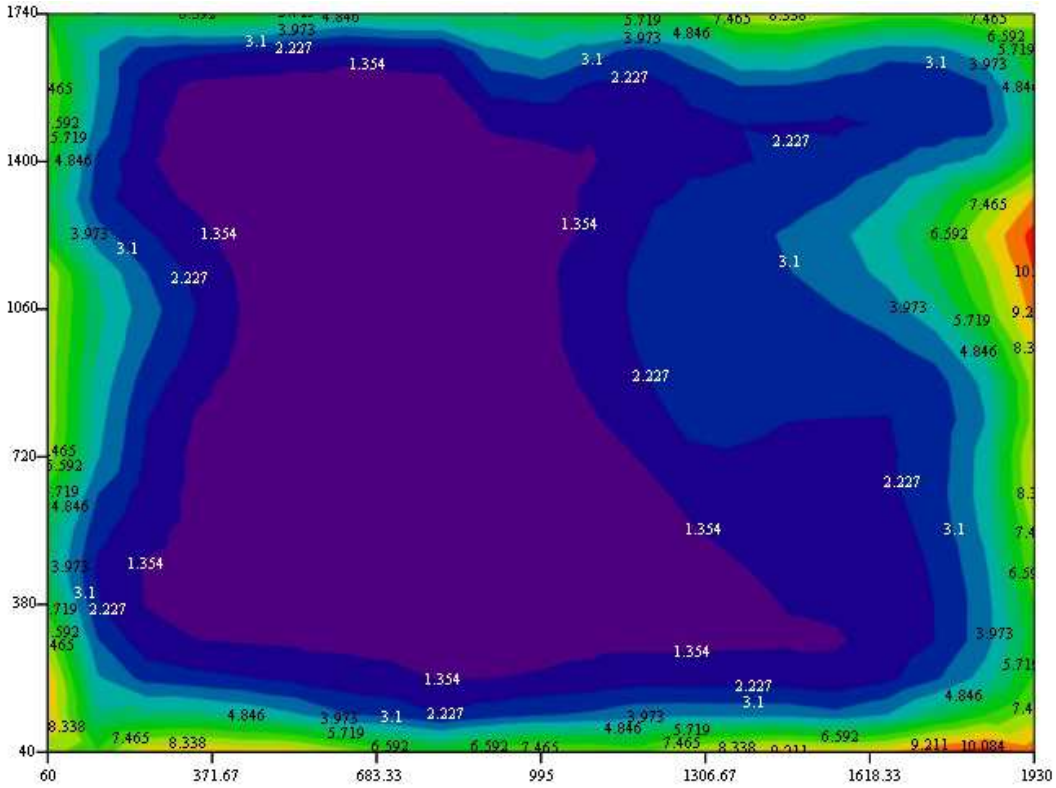

Figure 6.4 Turbulenc intensity distribution for an empty section, position x = 0 m

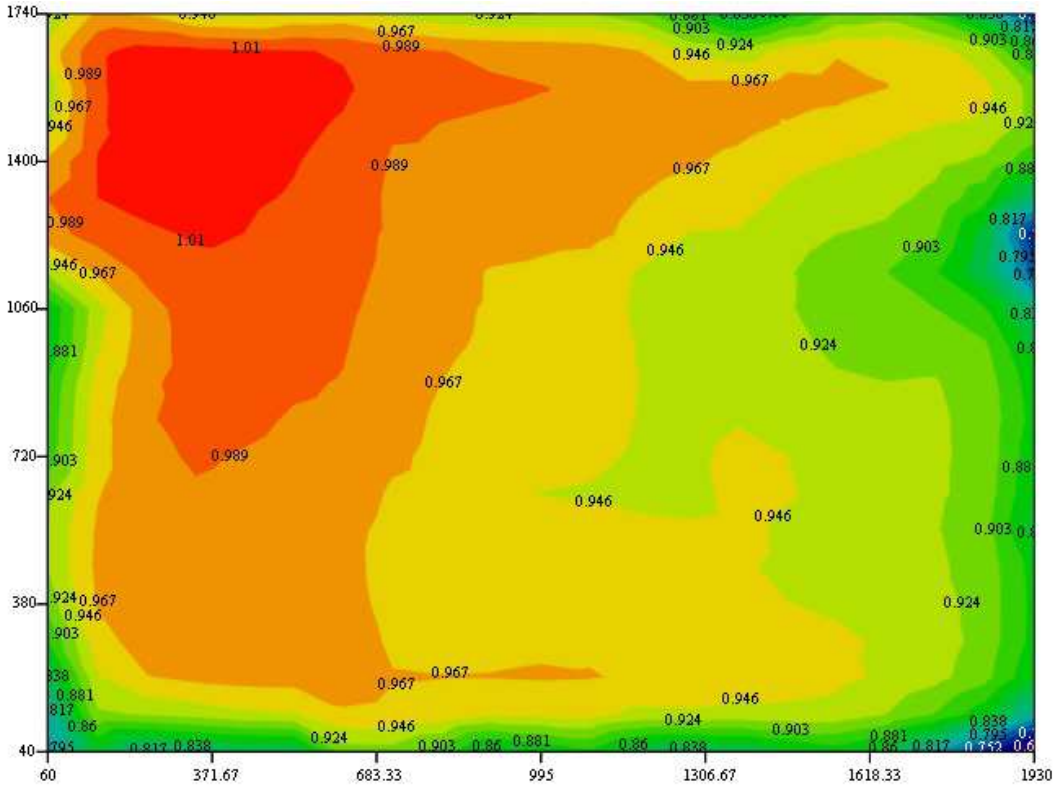

Figure 6.5 Velocity distribution for an empty section, position x = 2 m

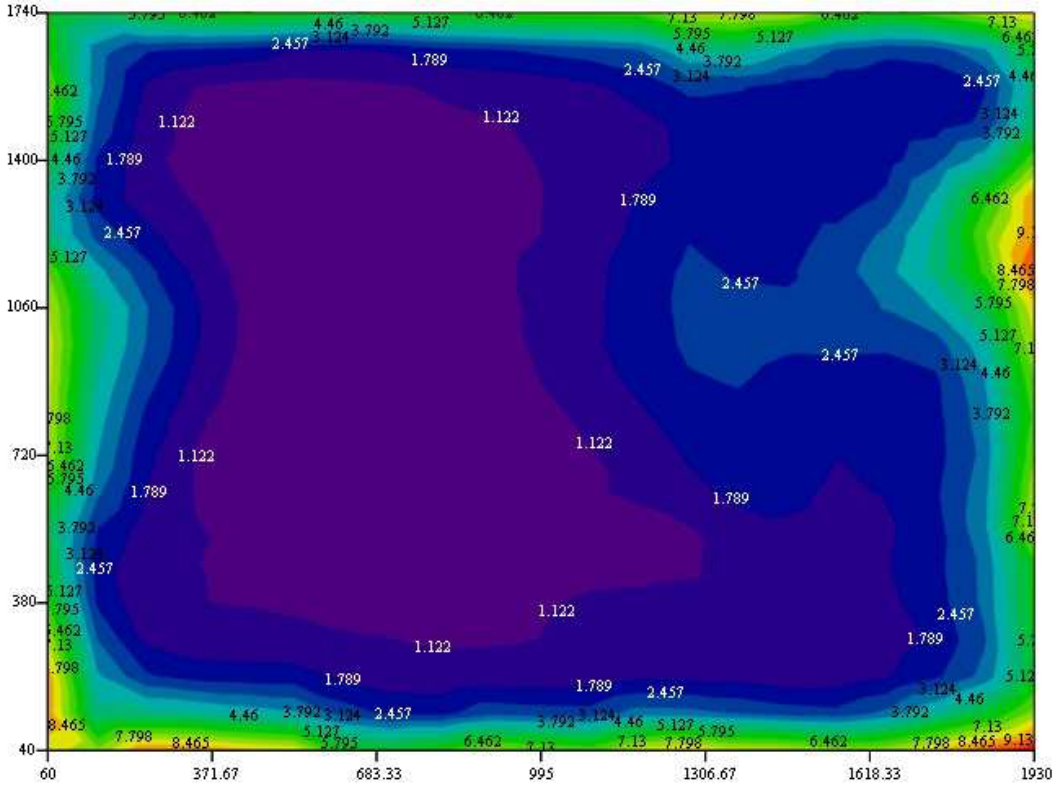

Figure 6.6 Turbulence intensity distribution for an empty section, position x = 2 m

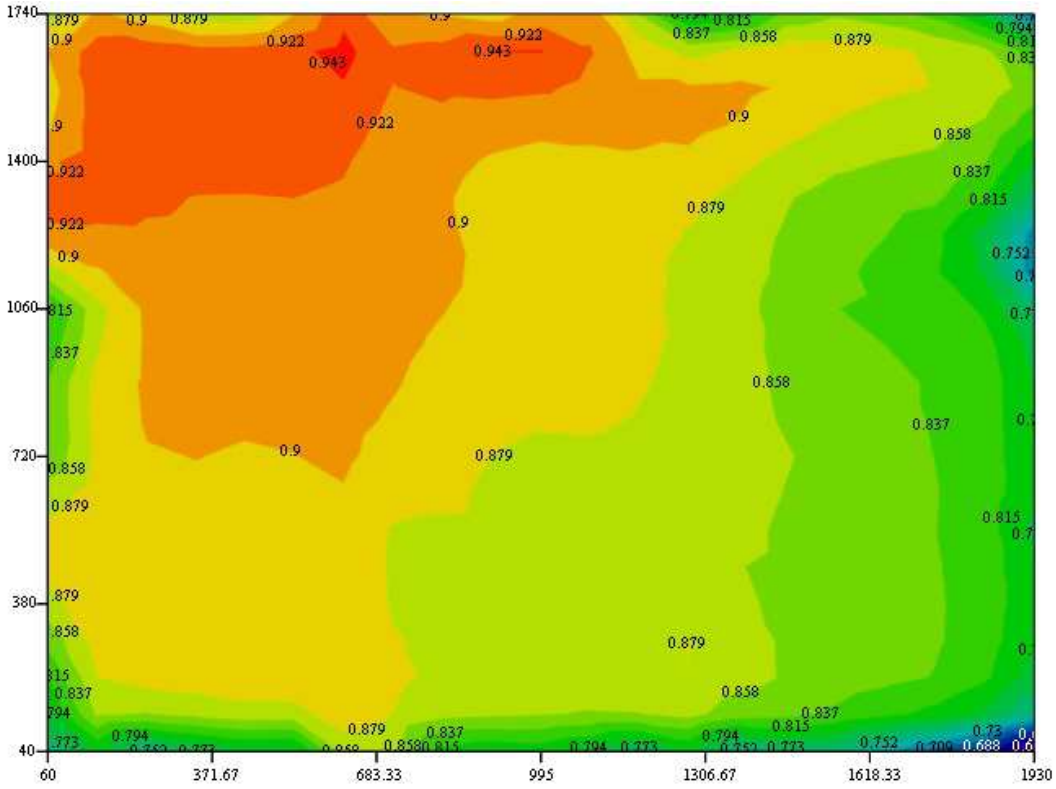

Figure 6.7 Velocity distribution for an empty section, position x = 4 m

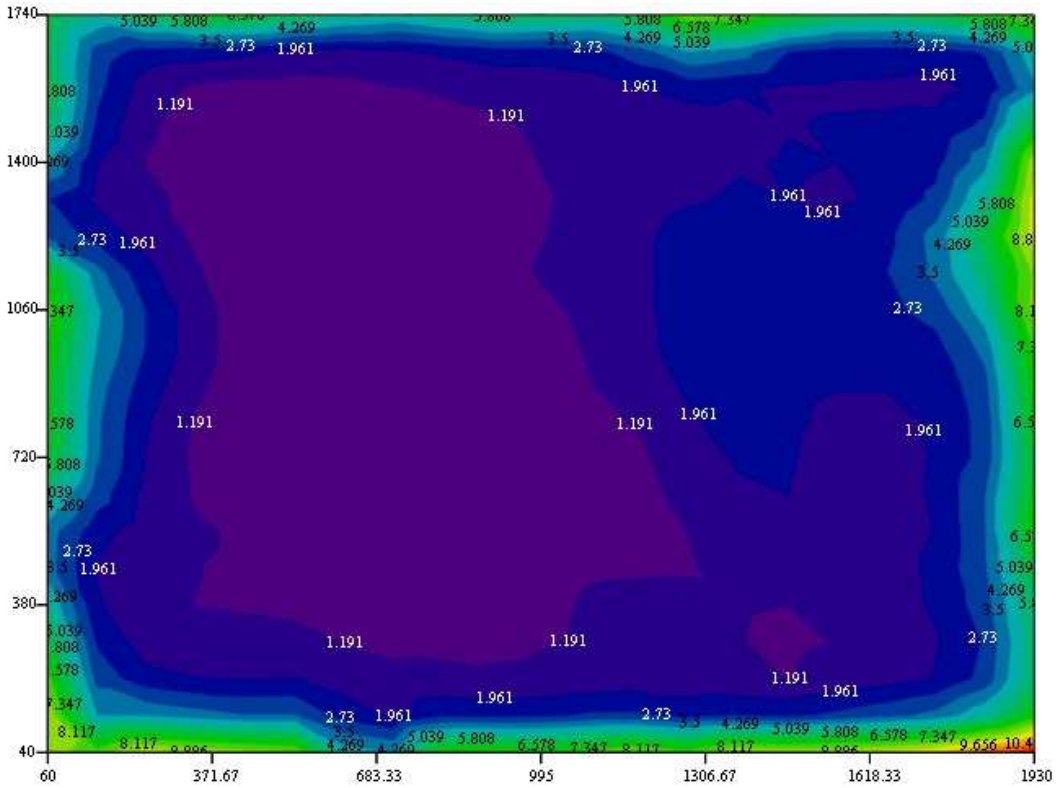

Figure 6.8 Turbulence intensity distribution for an empty section, position x = 4 m

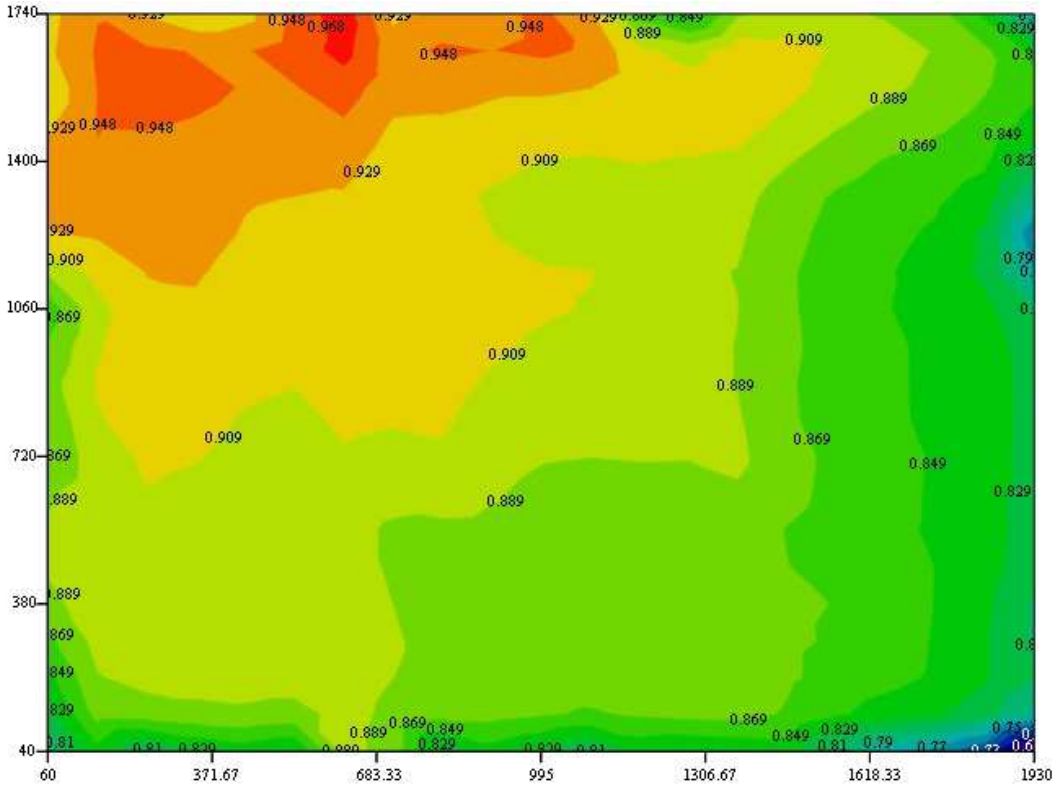

Figure 6.9 Velocity distribution for an empty section, position x = 6 m

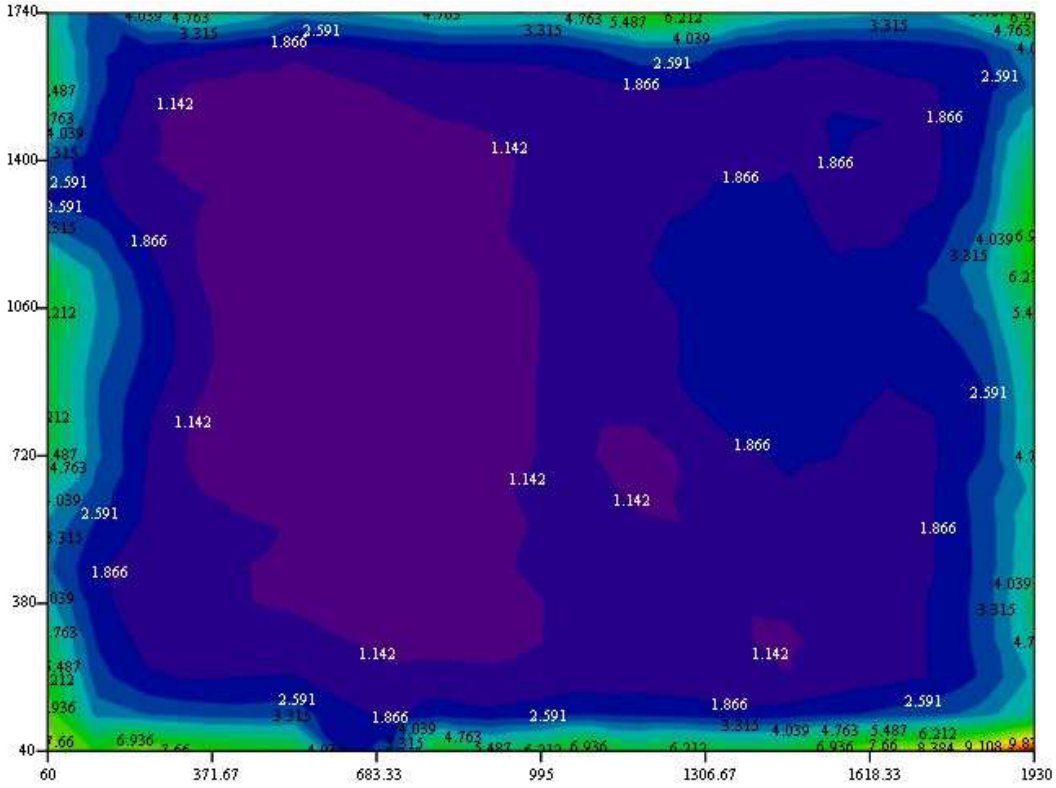

Figure 6.10 Turbulence intensity distribution for an empty section, position x = 6 m

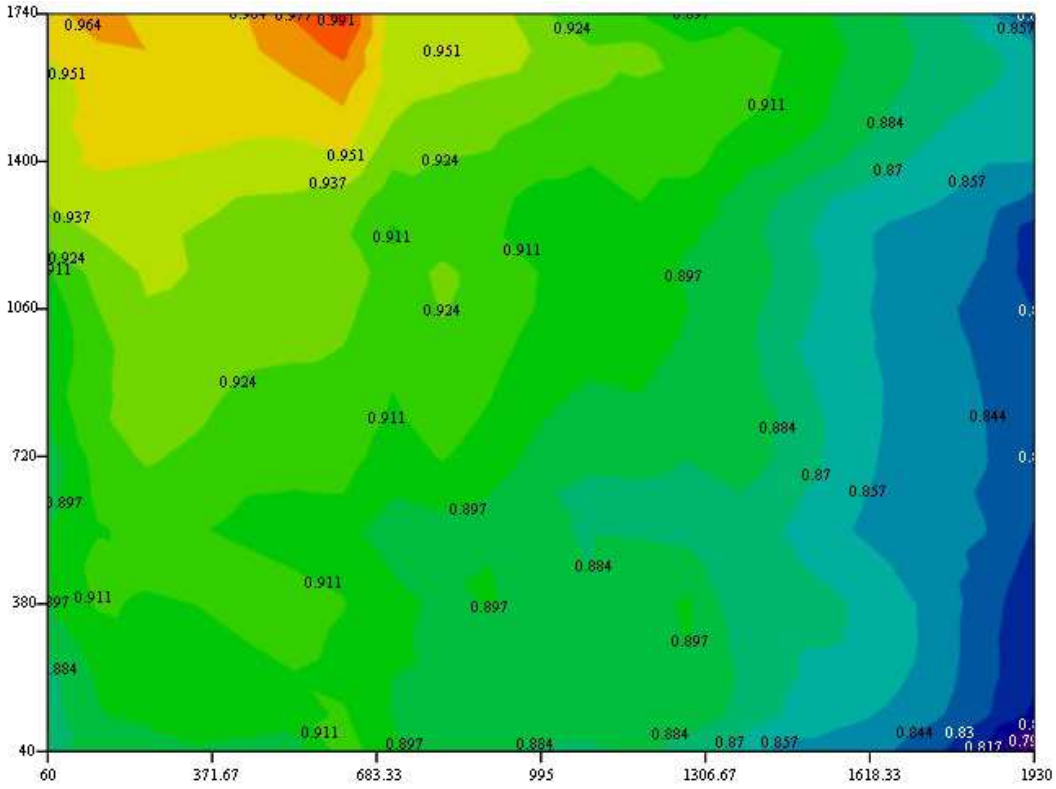

Figure 6.11 Velocity distribution for an empty section, position x = 8 m

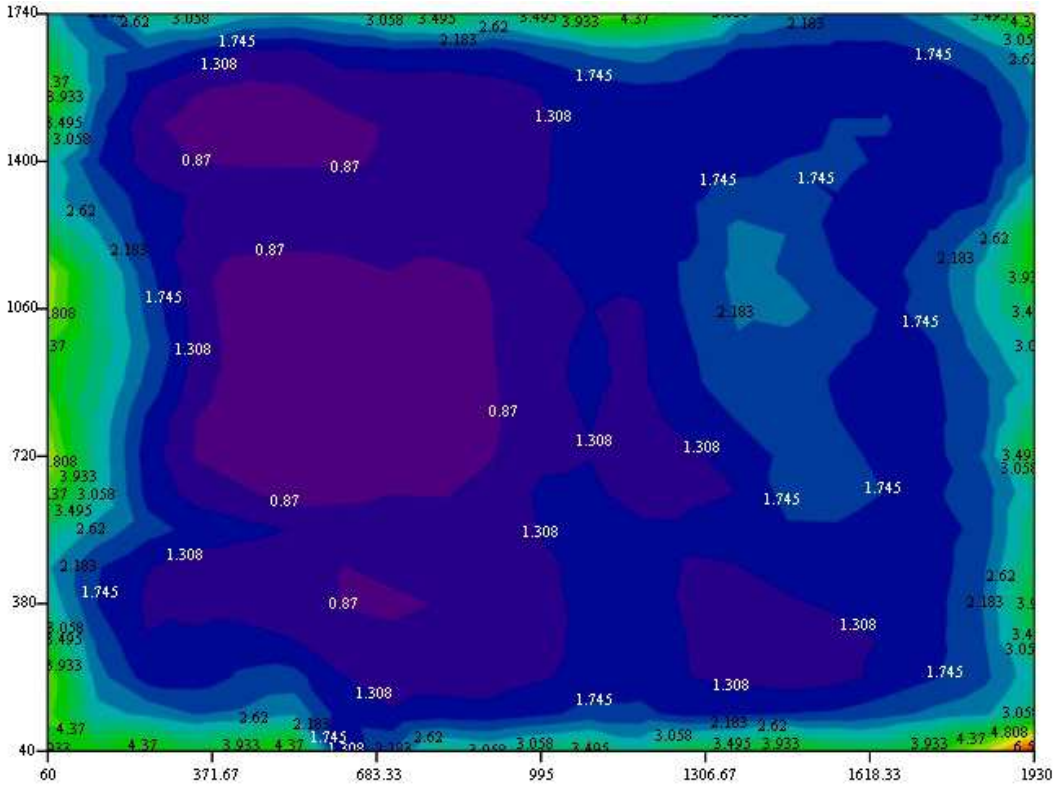

Figure 6.12 Turbulence intensity distribution for an empty section, position x = 8 m

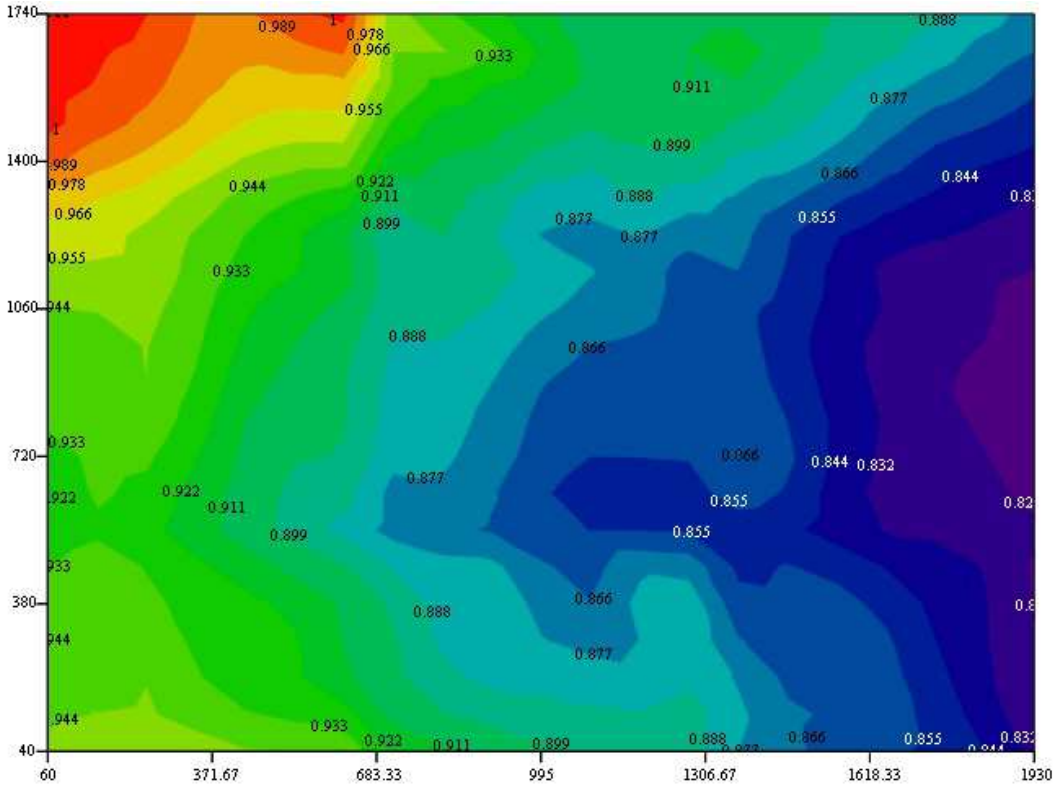

Figure 6.13 Velocity distribution for an empty section, position x = 9.3 m

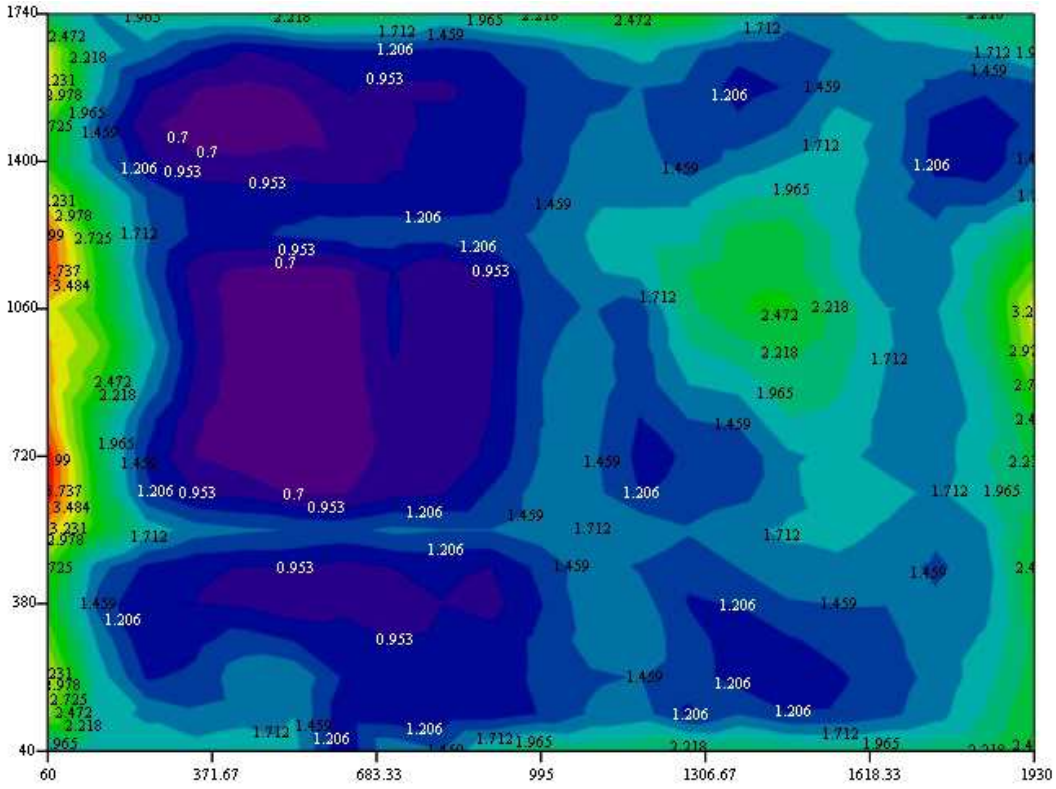

Figure 6.14 Turbulence intensity distribution for an empty section, position x = 9.3 m

The experimental results obtained for the *u* velocity field indicate a speed-up of the flow along the test section, i.e. as the air flows from the test section inlet toward the turntable, where the tests on structural models are commonly carried out. In particular, this increase in wind velocity can reach as much as 10% for the same lateral and vertical position at different longitudinal cross-sections. This is possibly due to the fact that at this moment the test section does not have diverging side walls or ceiling adjustable in height that would minimize pressure gradient development along the test section. Hence, due to a thickening of the boundary layers at the walls of the test section in the longitudinal direction, the flow speeds up in the central part of the test section. This phenomenon is additionally documented in Fig 6.15.

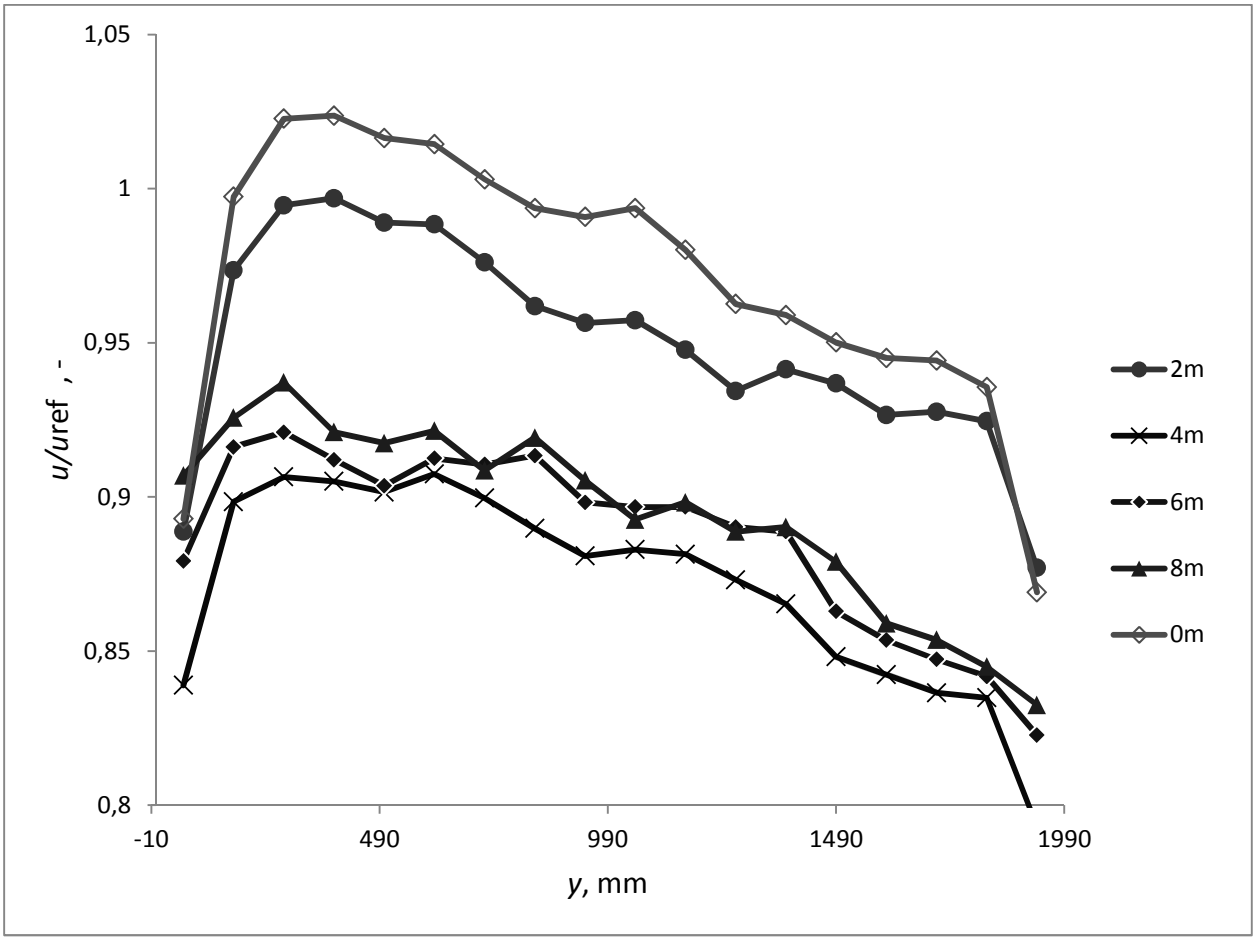

Figure 6.15 *u* velocity profile in the *y-z* plane along the test section

6.2. Wind-tunnel simulation of the atmospheric boundary layer flow

Experimental results for the ABL simulation are reported in Figs. 6.16 to 6.20, whereas mean wind velocity and turbulence intensity in longitudinal direction were analyzed in more detail at the turntable center (x = 0 m) and 1.5 m upwind from this position (x = 1.5 m). Mean wind velocities are normalized using a reference velocity u_{ref} measured in the freestream flow. Turbulence intensity I_u is normalized using a mean wind velocity at the corresponding measuring point. Velocity profile is compared against a commonly accepted power-law (Fig. 6.21), while turbulence intensity is compared to an international wind engineering standard ESDU74031 (Fig. 6.22) scaled-down at the simulation length scale factor 1:250. Both velocity and turbulence intensity profiles are reported for the central lateral position of the test section (y = 0). Taking into account a fact that the boundary layer thickness in the wind-tunnel is usually equal to the wind generators height [21] the created ABL simulation would be 375 m thick in the atmosphere that corresponds well with the full-scale conditions.

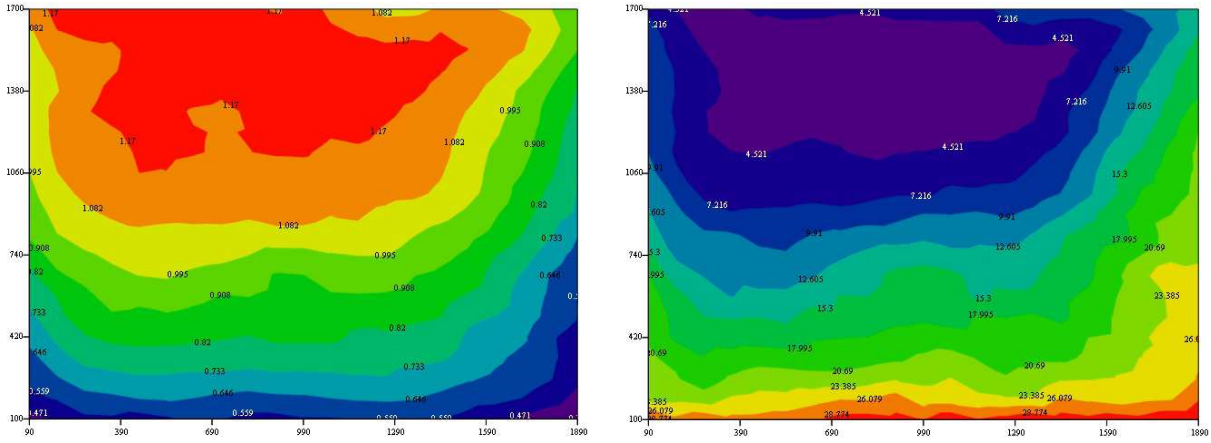

x = 0 m x = 0 m

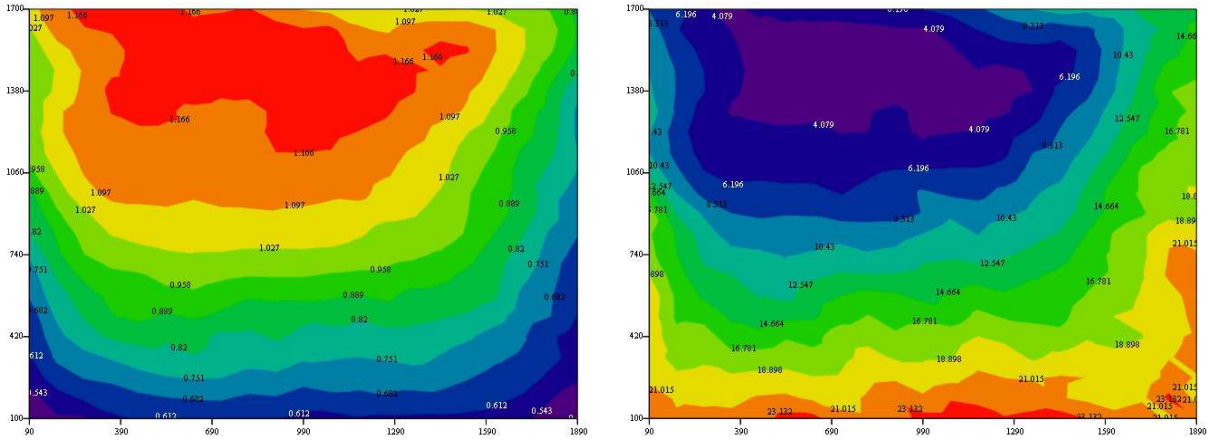

x = 1.5 m x = 1.5 m

Figure 6.16 Velocity (left) and turbulence distribution (right) ABL simulation

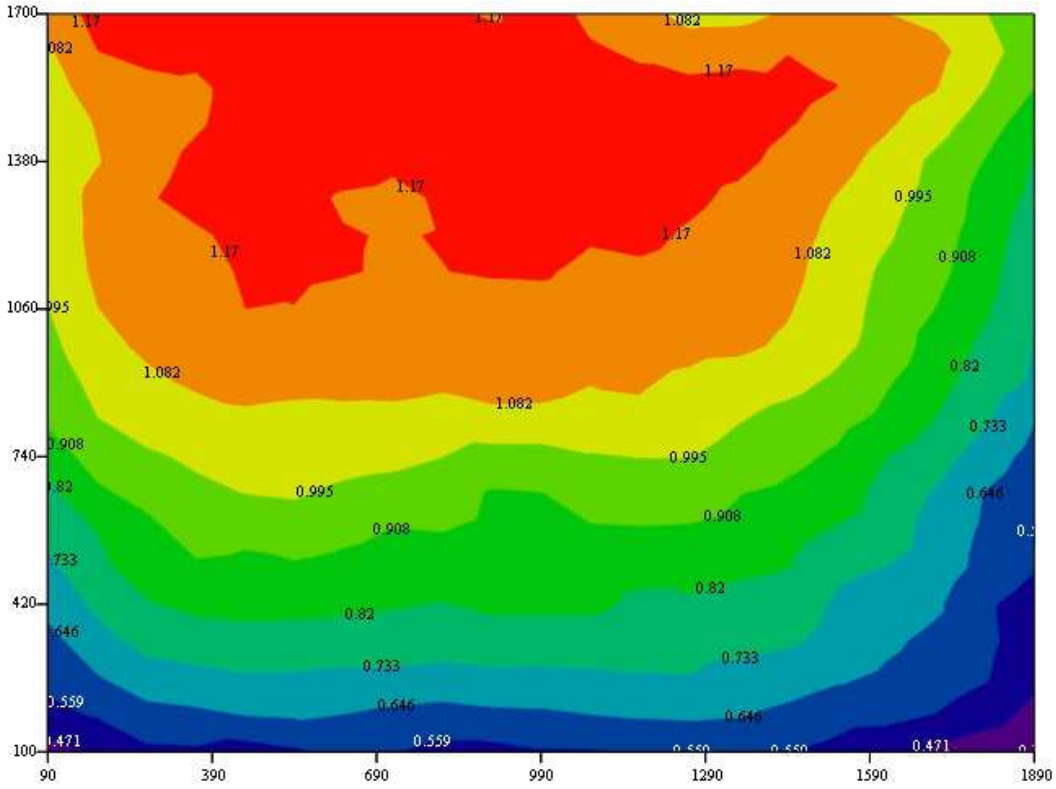

Figure 6.17 Velocity distribution in the ABL simulation, section x = 0 m

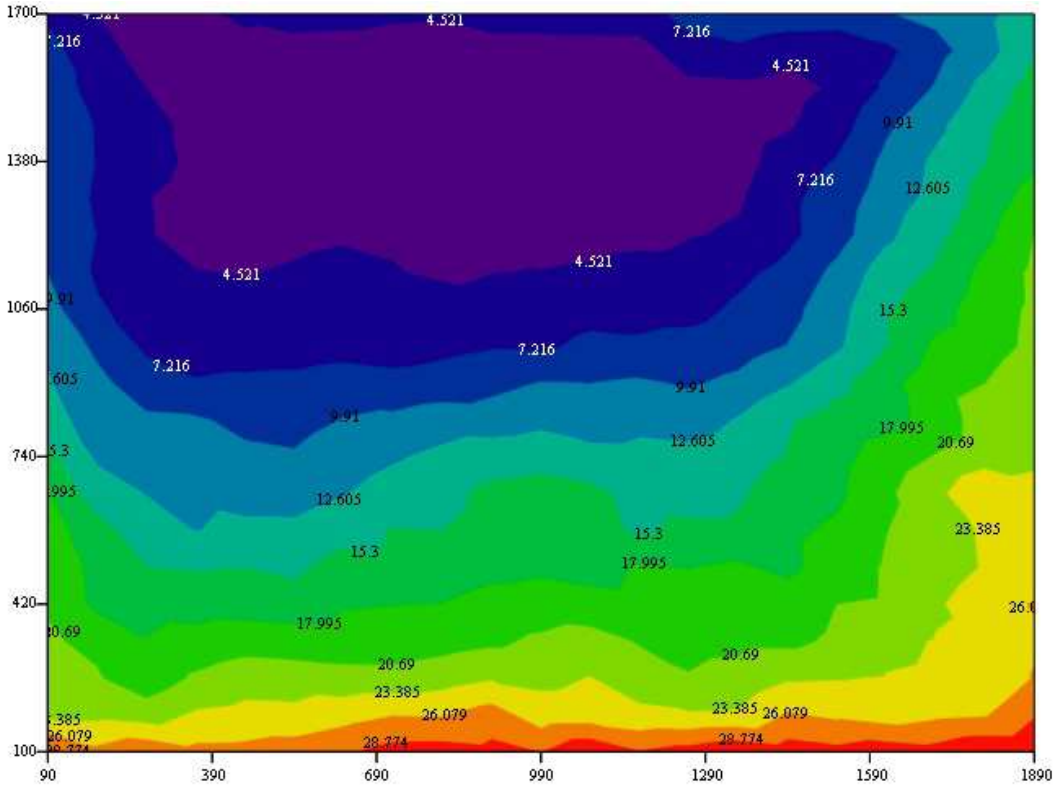

Figure 6.18 Turbulence intensity distribution in the ABL simulation, section x = 0 m

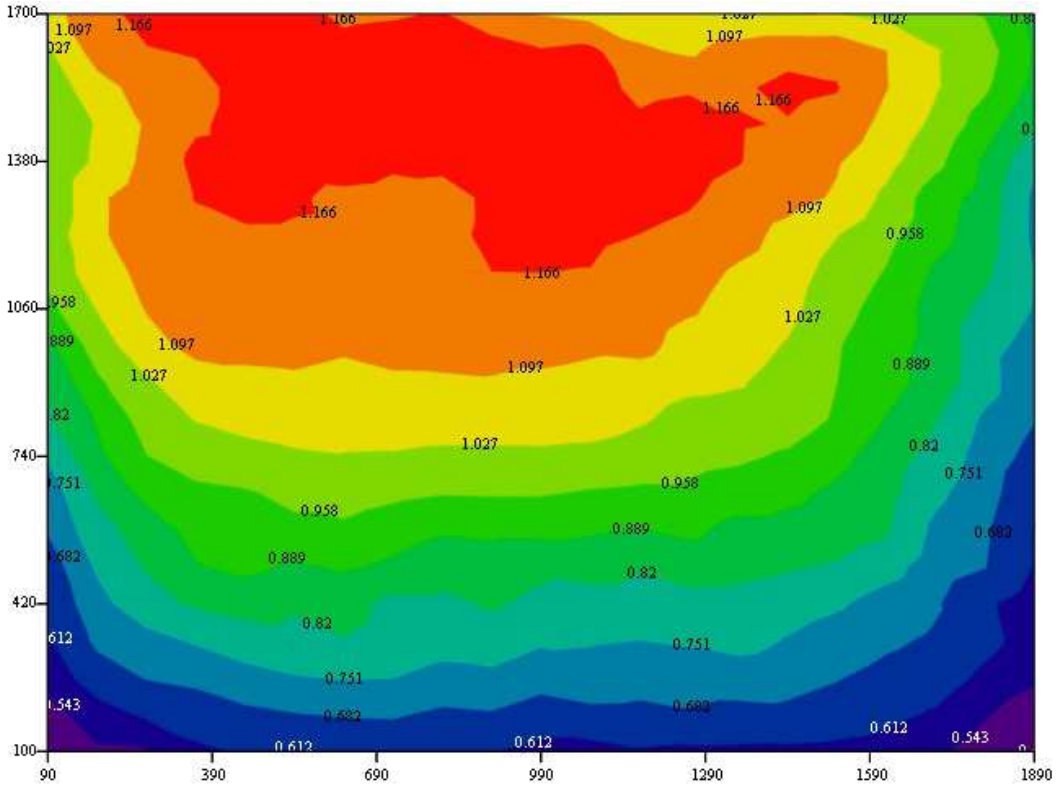

Figure 6.19 Velocity distribution in theABL simulation, x = 1.5 m upwind from the turntable center

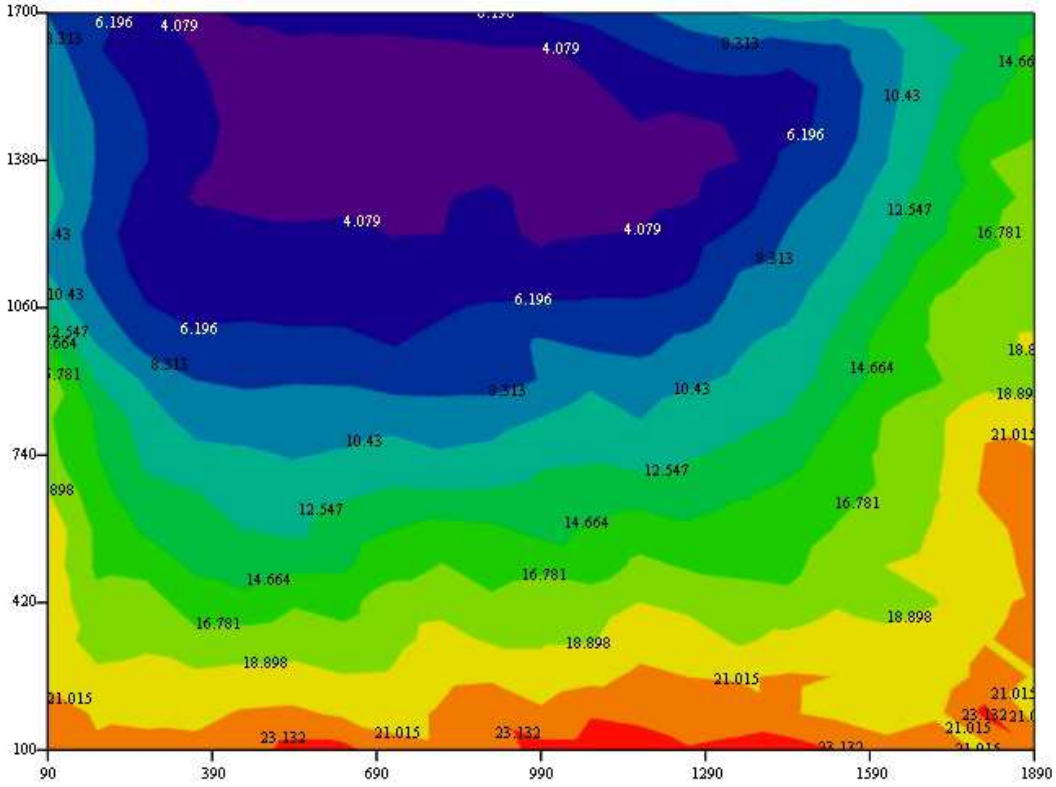

Figure 6.20 Turbulence intensity distribution in the ABL simulation, x = 1.5 m upwind from the turntable center

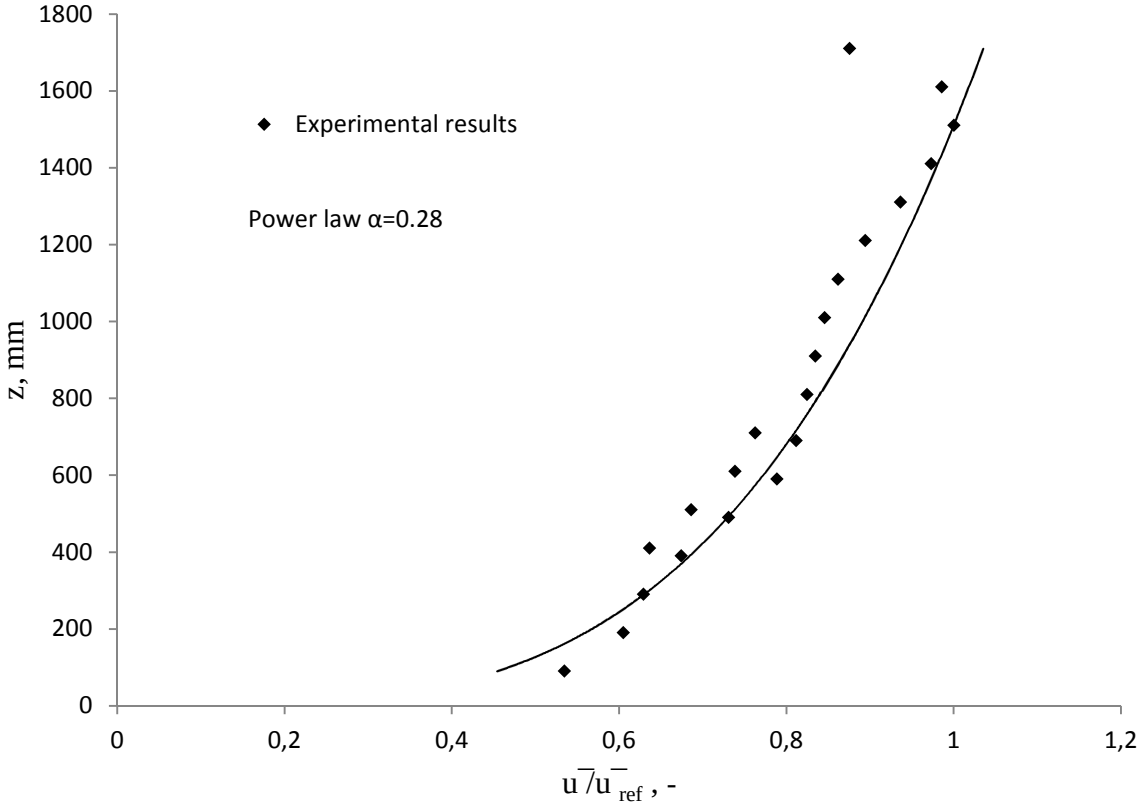

Figure 6.21 Velocity profile at $y = 0$

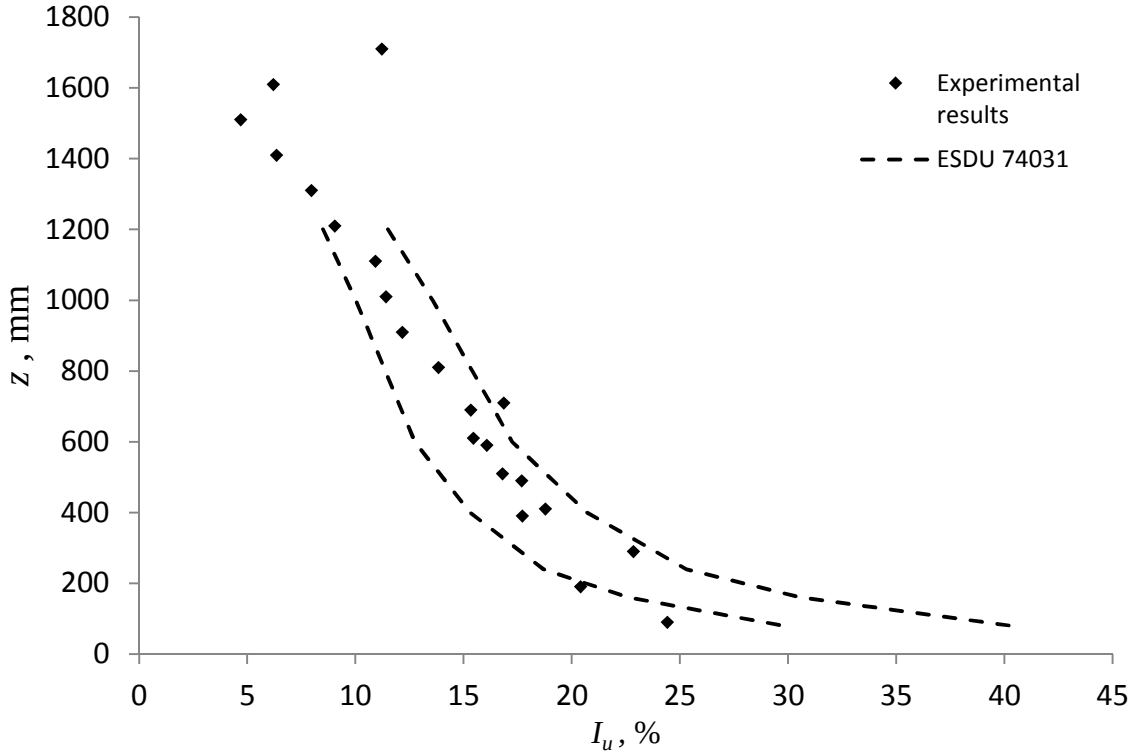

Figure 6.22 Turbulence intensity in longitudinal direction at $y = 0$

Experimental results show a good uniformity in lateral direction that indicates that the surface roughness can be successfully applied in creating and sustaining uniform turbulent flow conditions in the wind-tunnel test section. In this configuration flow and turbulence uniformity is significantly better compared to the results obtained in an empty test section. Velocity profile corresponds well to the power-law with an exponent α is 0.28, while the results for turbulence intensity are within $\pm$15% of the recommended ESDU74031 values for this terrain type that corresponds to an urban topography. In addition, it is believed that the ABL simulation could be additionally improved by widening the sidewalls of the test section in longitudinal direction and placing several grids and possibly an additional honeycomb in the nozzle at the test section inlet.

6.3. Boundary layer simulation using a surface grid

Additional tests were carried out in order to investigate further possibilities with improving the flow and turbulence conditions by using a grid placed at the test section floor. In this configuration two separate experiments were performed with two different heights of grid with respect to the test section floor, i.e. 1 cm and 5 cm. In those tests the castellated barrier wall and the vortex generators were not used. Experimental results are reported in Figs. 6.23 to 6.36, whereas mean wind velocity and turbulence intensity in longitudinal direction were studied at the turntable center (x = 0 m), 1 m upwind from this position (x = 1 m) and 1 m downwind from the turntable center (x = -1 m). Mean wind velocities are normalized using a reference velocity u_{ref} measured in the freestream flow. Turbulence intensity I_u is normalized using a mean wind velocity at the corresponding measuring point.

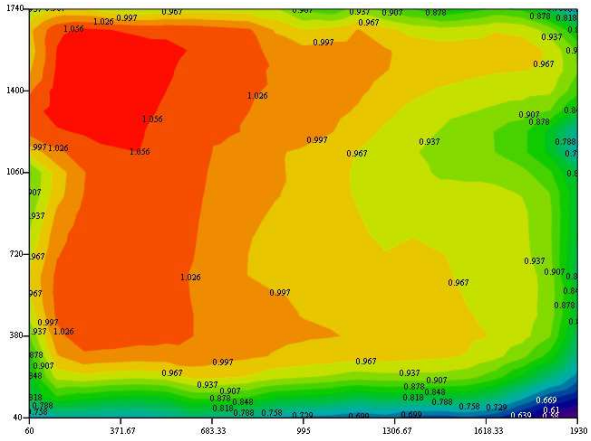

x = -1 m

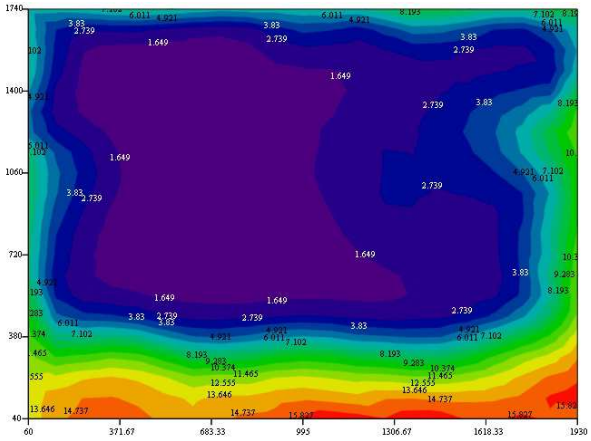

x = -1 m

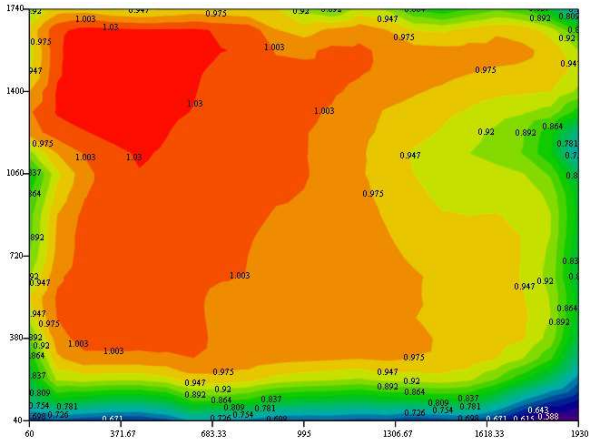

x = 0 m

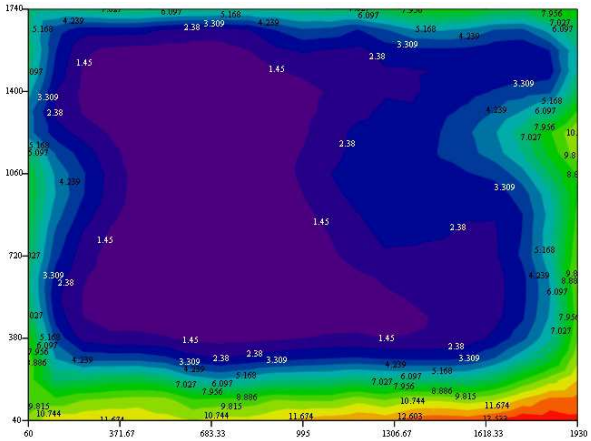

x = 0 m

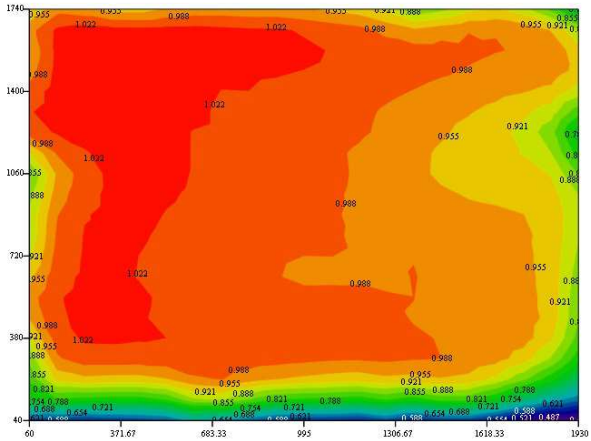

x = 1 m

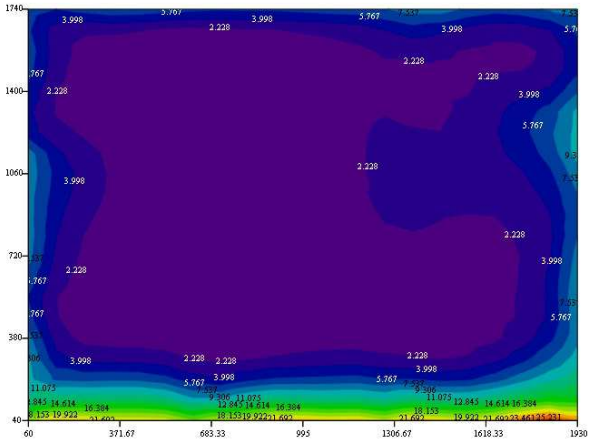

x = 1 m

Figure 6.23 Velocity (left) and turbulence distribution (right) for grid placed on the wind tunnel floor at height 1cm

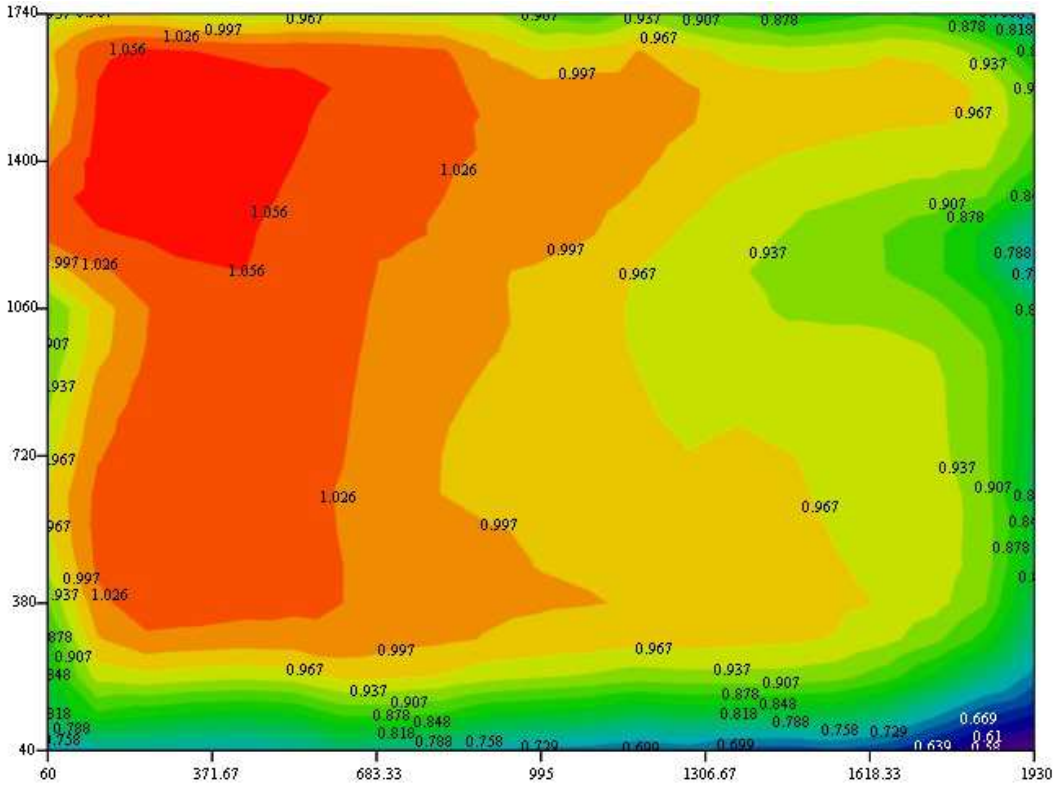

Figure 6.24 Velocity distribution, grid height 1 cm, x = 1 m downwind from turntable center

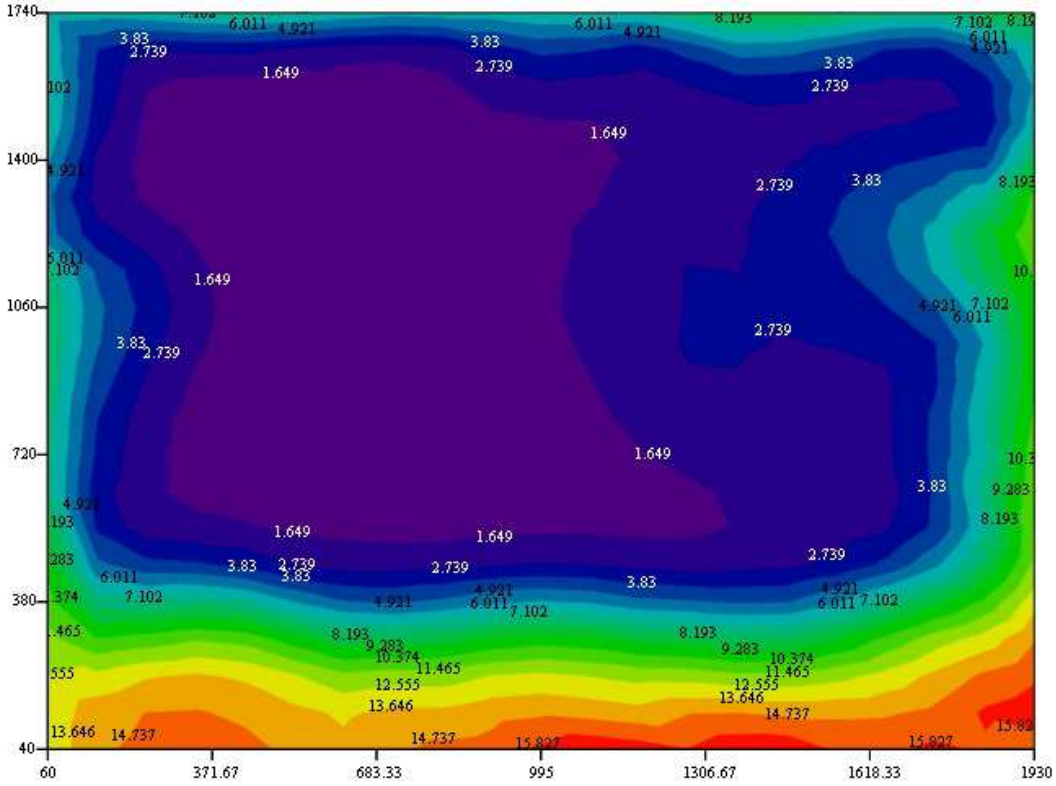

Figure 6.25 Turbulence intensity distribution, grid height 1 cm, x = 1 m downwind from turntable center

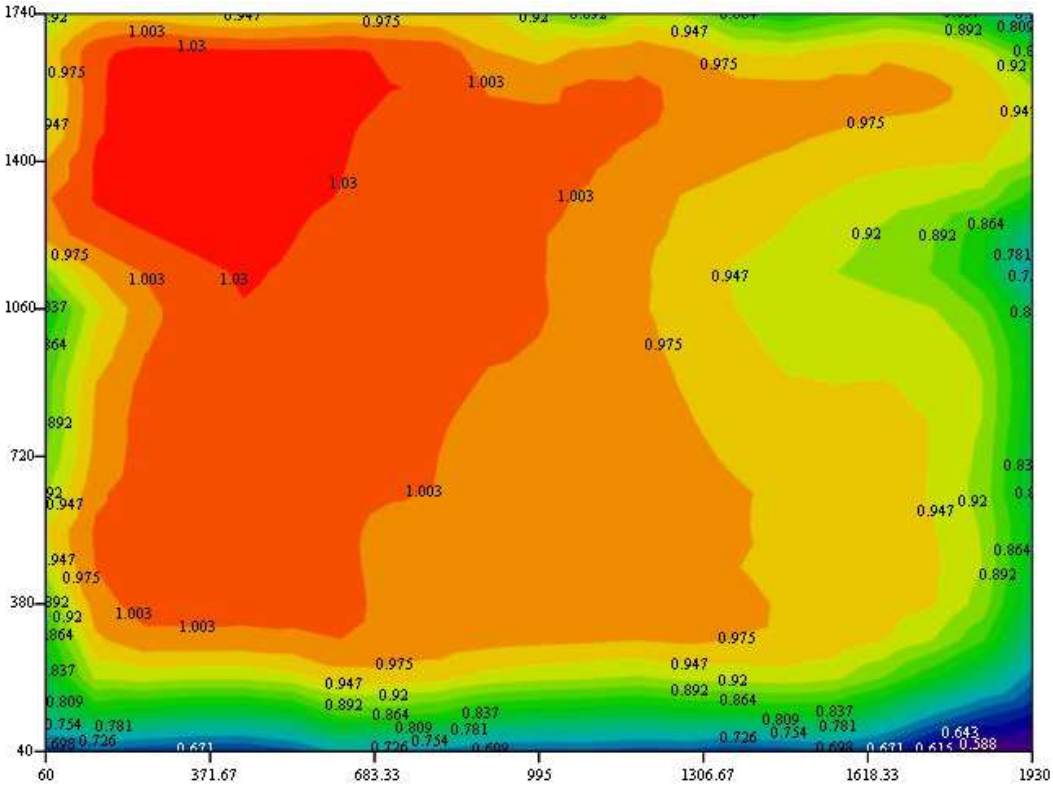

Figure 6.26 Velocity distribution, grid height 1 cm, x = 0 m at the turntable center

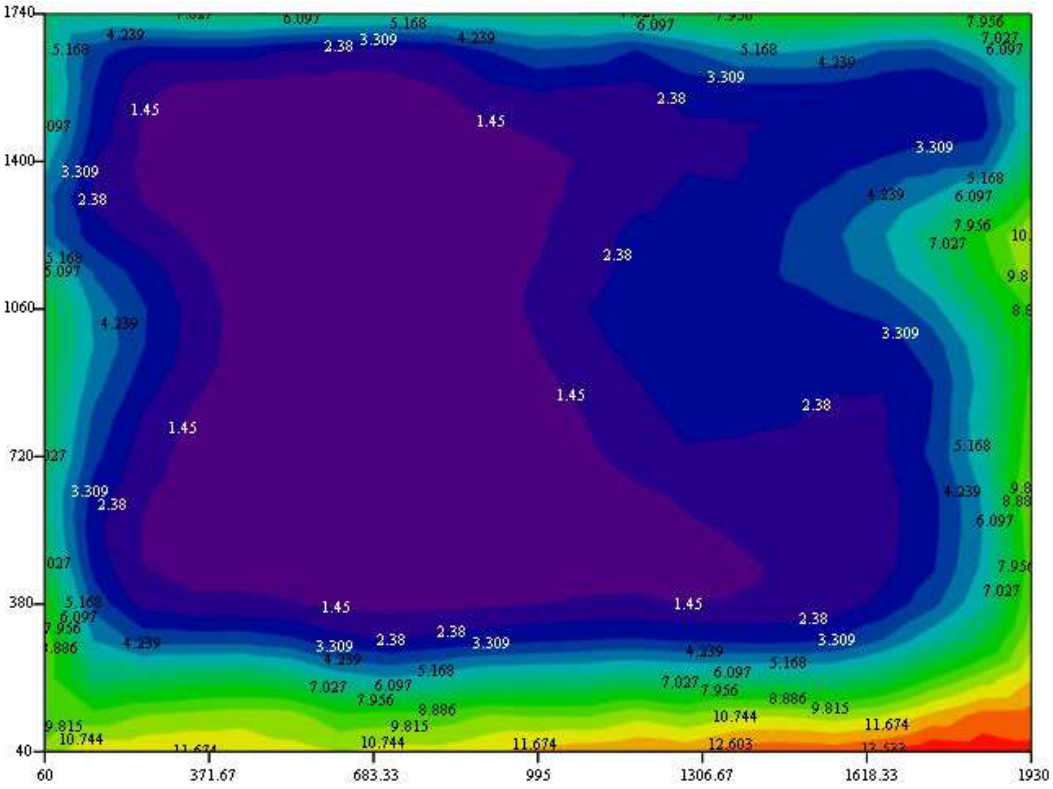

Figure 6.27 Turbulence intensity distribution, grid height 1 cm, x = 0 m at the turntable center

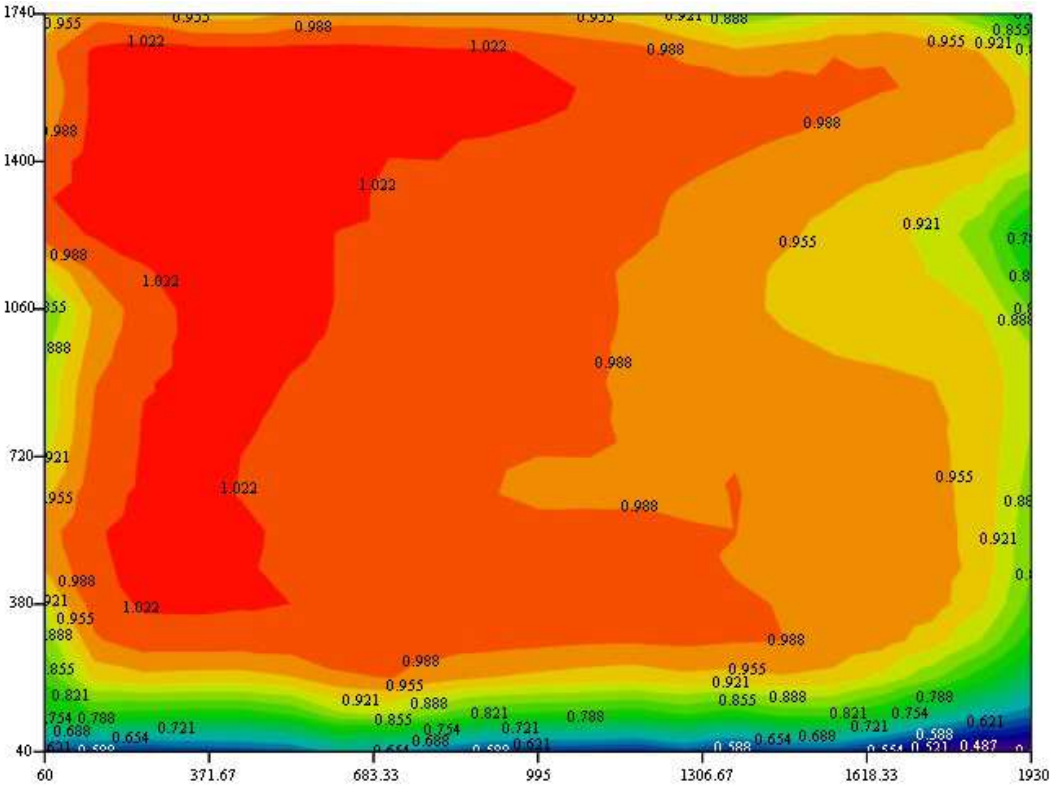

Figure 6.28 Velocity distribution, grid height 1 cm, x = 1 m upwind from the turntable center

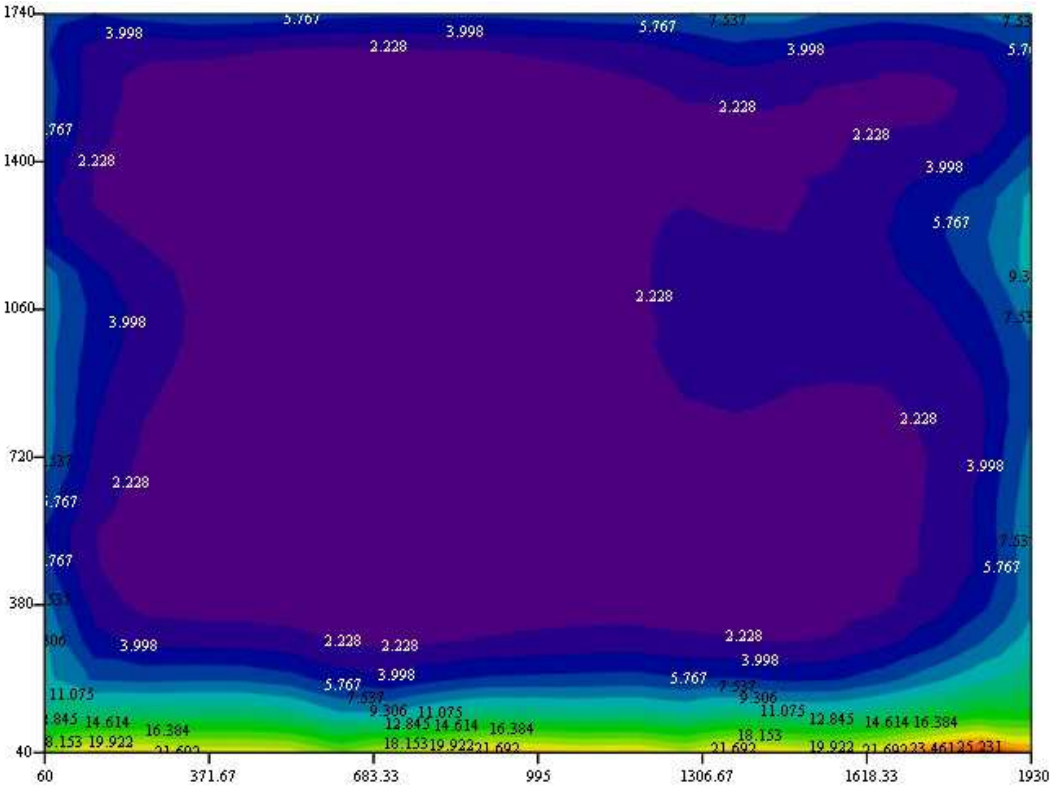

Figure 6.29 Turbulence intensity distribution, grid height 1 cm, x = 1 m upwind from the turntable center

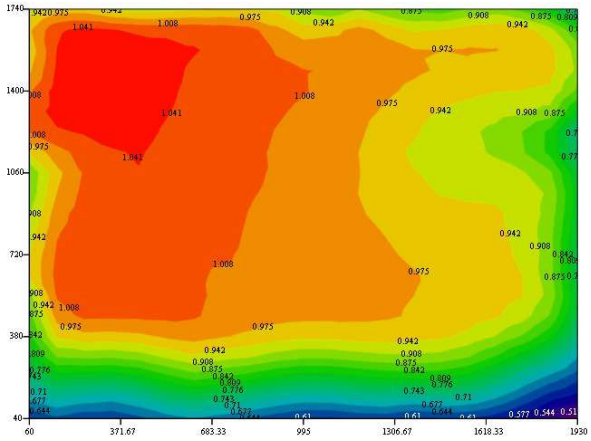

x = -1 m

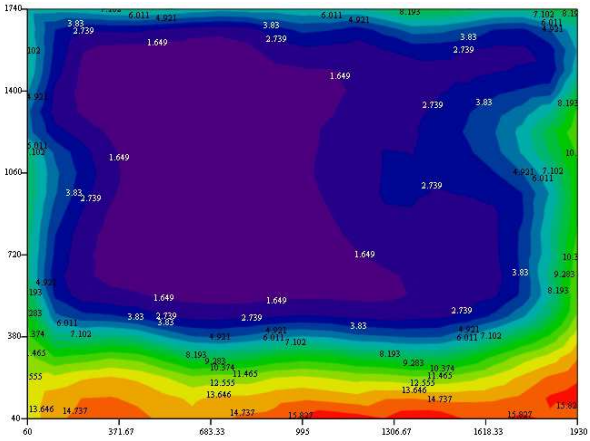

x = -1 m

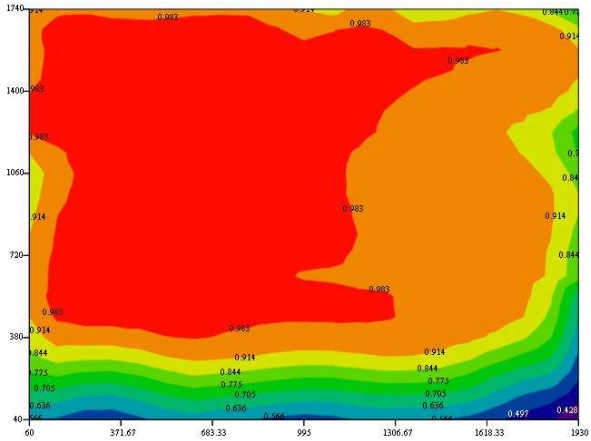

x = 0 m

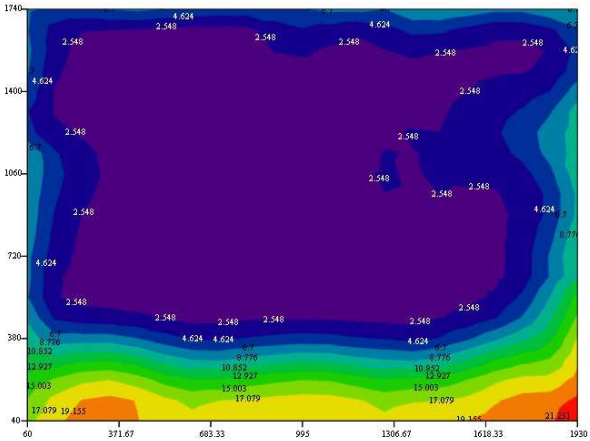

x = 0 m

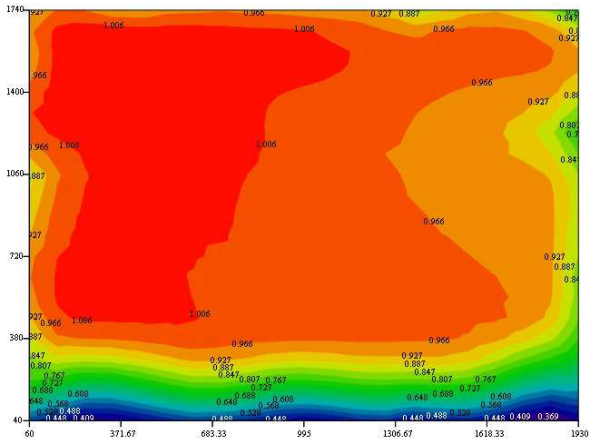

x =1m

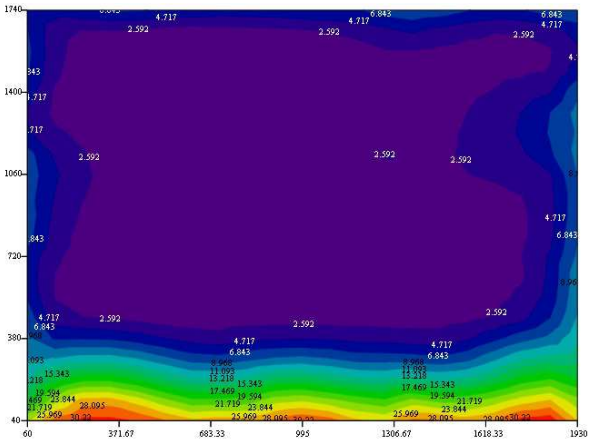

x=1 m

Figure 6.30 Velocity (left) and turbulence distribution (right) for grid placed on the wind tunnel floor at height 5 cm

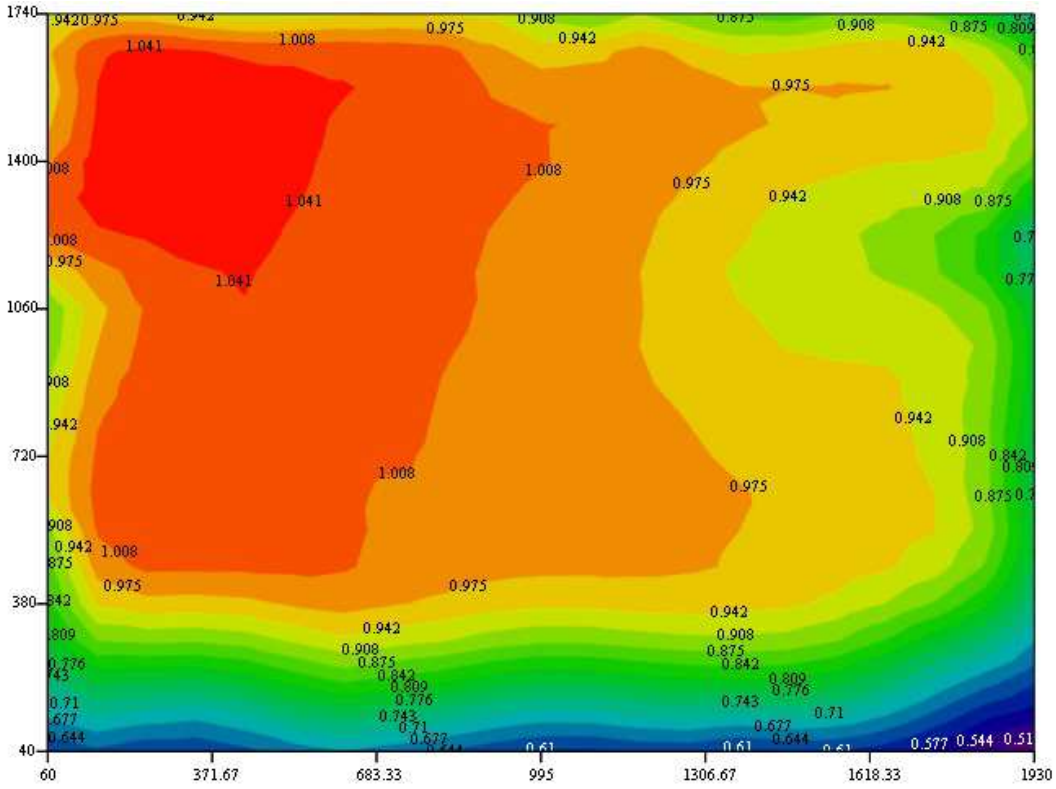

Figure 6.31 Velocity distribution, grid height 5 cm, x = 1 m downwind from the turntable center

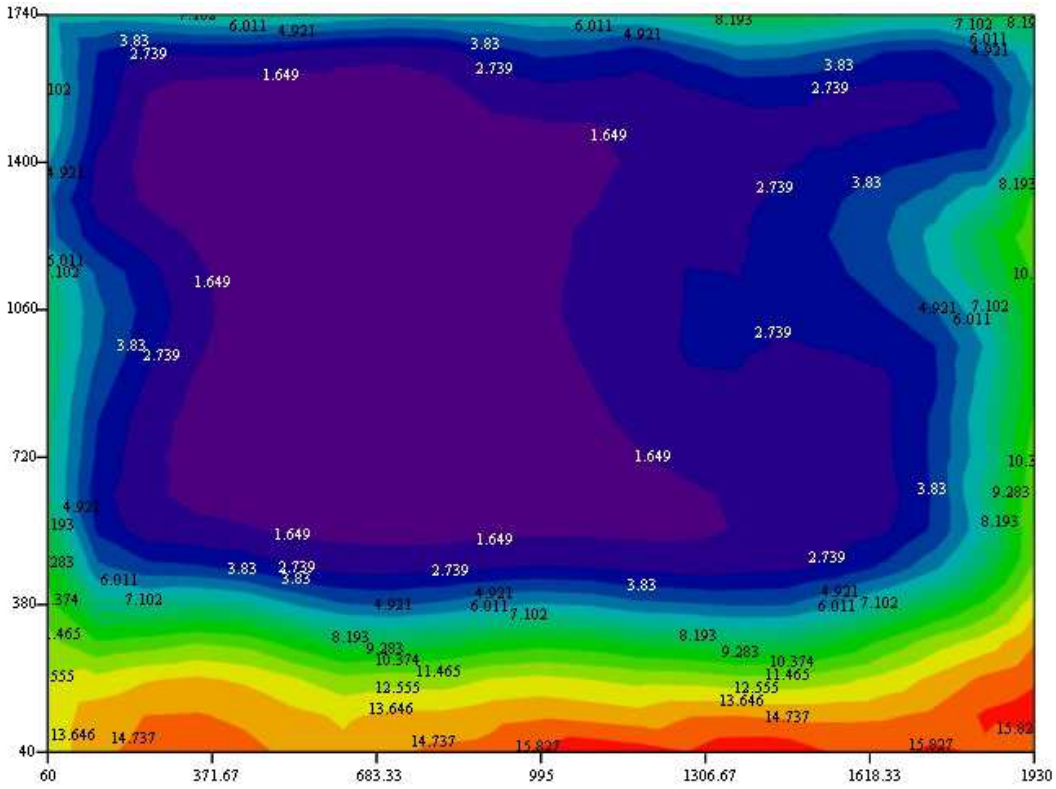

Figure 6.32 Turbulence intensity distribution, grid height 5 cm, section x = 1 m downwind from the turntable center

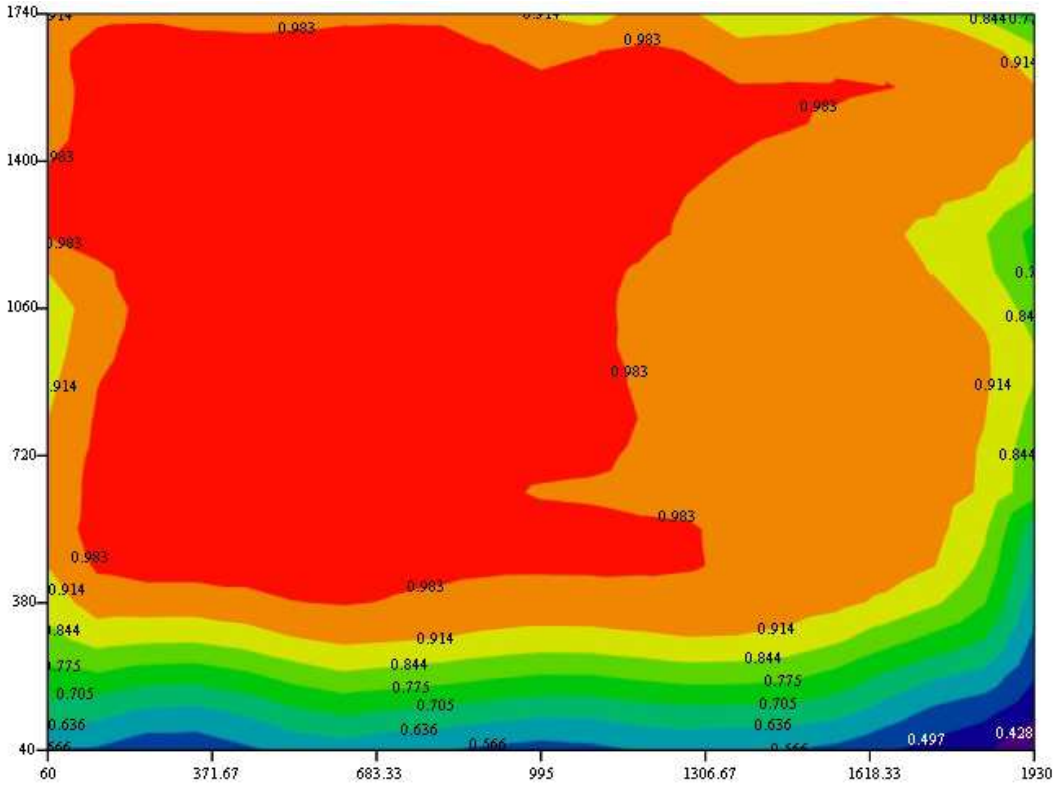

Figure 6.33 Velocity distribution, grid height 5 cm, x = 0 m at the turntable center

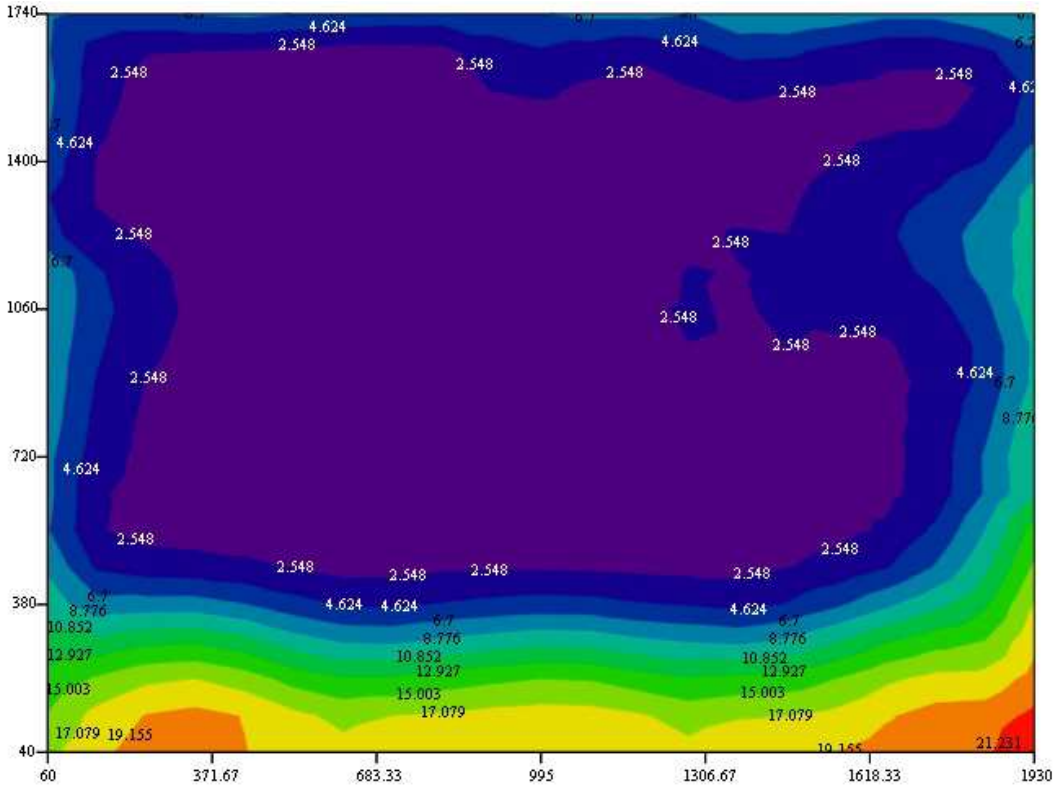

Figure 6.34 Turbulence intensity distribution, grid height 5cm, x = 0 m at the turntable center

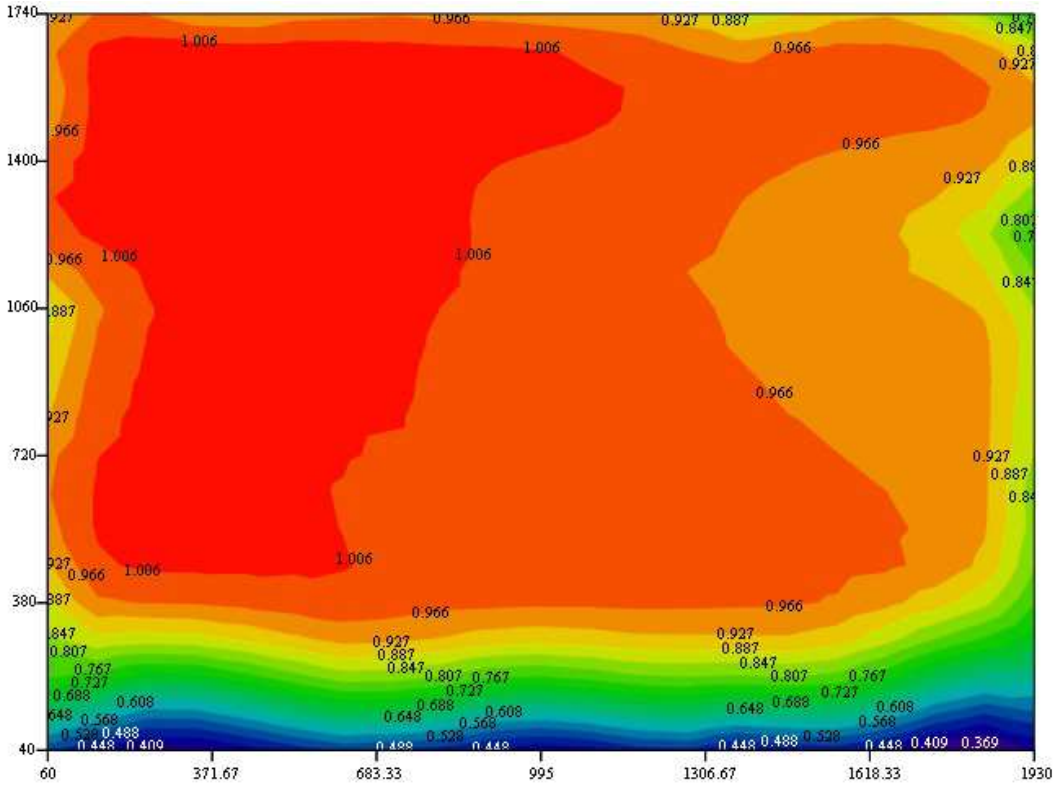

Figure 6.35 Velocity distribution, grid height 5 cm, x = 1 m upwind from turntable center

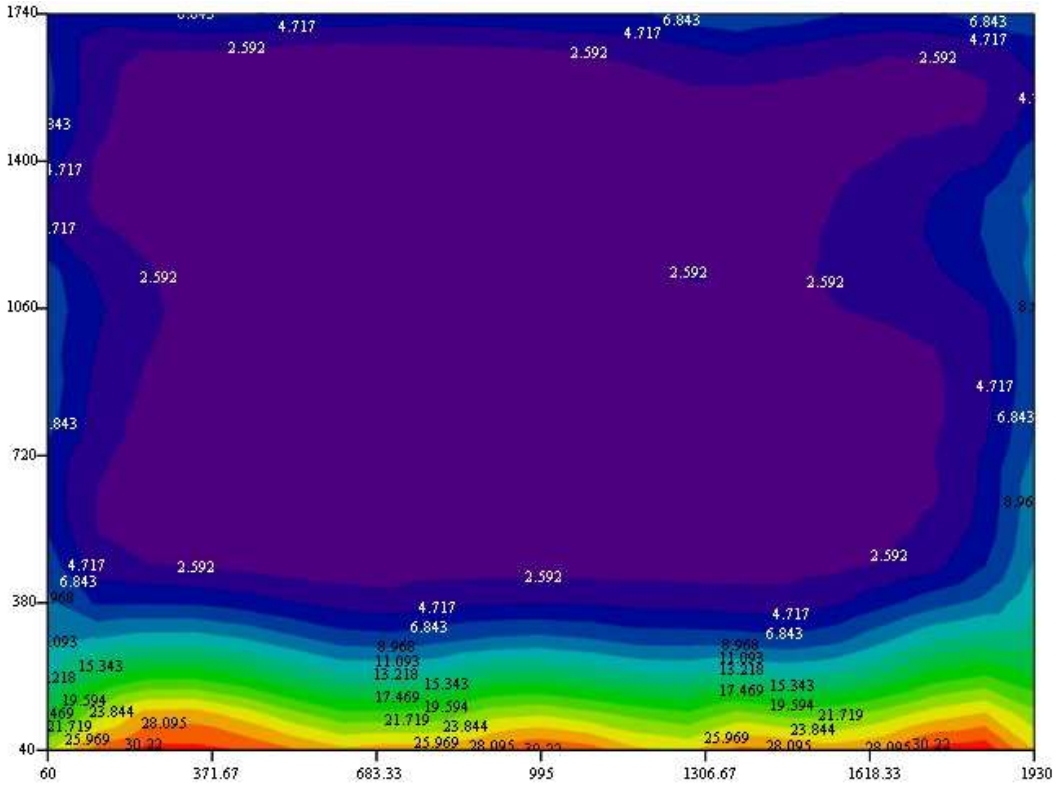

Figure 6.36 Turbulence intensity distribution, grid height 5 cm, x = 1 m upwind from turntable center

The results obtained for configuration with grid placed at the test section floor show a strong similarity with the results from an empty section. Therefore, this particular arrangement does not yield significant improvements in flow and turbulence uniformity.

7. CONCLUSION

An extensive set of experiments was carried out in the newly developed CET climatic wind- tunnel in order to characterize flow and turbulence in this facility. The tests performed in an empty wind-tunnel test section indicate a speed-up of the flow along the test section as the air flows from the test section inlet toward the turntable. This increase in wind velocity can reach as much as 10% for the same lateral and vertical position at different longitudinal cross-sections. This is possibly due to the fact that at this moment the test section does not have diverging side walls or ceiling adjustable in height that would minimize pressure gradient development along the test section. Experimental simulations of the atmospheric boundary layer flow show a good uniformity in lateral direction that indicates that the surface roughness can be successfully applied in creating and sustaining uniform turbulent flow conditions in the wind-tunnel test section. Velocity profile corresponds well to the power-law with an exponent α is 0.28, while the results for turbulence intensity are within the recommended ESDU74031 values for the simulated urban terrain type. The results for configuration with grid placed at the test section floor show a strong similarity with the results from an empty section. Therefore, this particular arrangement does not yield significant improvements in flow and turbulence uniformity. Future work would need to further address improving the flow and turbulence characteristics in this facility. A possibility in this direction could be widening of the sidewalls in the test section and placing several grids and an additional honeycomb in the nozzle at the test section inlet.

Bibliography

[1] J. Cermak, Wind tunnel for the study of turbulence in the atmospheric surface layer, Final Report.

[2] E. Simiu, Design of Buildings for Wind:A Guide for ASCE 7-10 Standard, New York,Wiley &Sons, (2011).

[3] C. Dyrbye, S. Hansen,., Wind loads on structures, John Wiley & Sons, Chichester,(1996).

[4] J. Counihan, A review and analysis of data from the period 1880-1972, Atmospheric Environment, 197,9, pp. 871-905.

[5] J. Garratt, The atmospheric boundary layer, Cambridge University Press, (1992).

[6] E. Simiu, R.H. Scanlan, Wind Effects on Structures, John Wiley & Sons, (1996).

[7] T. Stevenson, Report on the simultaneous observations of the force of the wind at different heights over the ground,Bulletin of the American Meteorological Society, *5, pp. 348-351.*

[8] G. Hellman, Uber die Bewegung der Luft in den untersten Schichten der Atmosphare, Vieweg, (1915).

[9] N. Cook, The Designer's Guide to Wind Loading of Building Structures, BRE, (1990).

[10] ESDU, Engineering Sciences Data Unit, 74031, Characteristics of atmospheric turbulence near the ground, Part II: single point data for strong winds (neutral atmosphere), 1975.

[11] O. Sutton, Atmospheric Turbulence. Methuen, (London, 1949).

[12] H. Kozmar, Utjecaj mjerila na strukturu modeliranog atmosferskog graničnog sloja, Phd. T, Zagreb, (2005).

[13] H. Sockell, Aerodynamik der Bauwerke, Vieweg & Sohn, (1984).

[14] A. Davenport, The buffeting of large superficial structures by atmospheric turbulence, v. Karman Institute for Fluid Dynamics, Lectures Series 45, Wind Effects on Buildings and Structures, (1972).

[15] H. Pröpper, Zur aerodynamischen Belastung großer Kühltürme, Institut für konstruktiven Ingenieurbau, Ruhr-Universität Bochum, Technischwissenschaftliche Mitteilungen, (1977).

[16] H. Schlichting, K.Gersten, Grenzschicht-Theorie, Springer Verlag, (1996).

[17] J. Cermak, Applications of fluid mechanics to wind engineering - A Freeman Scholar Lecture, (1975).

[18] J.Counihan, An improved method of simulating an atmospheric boundary layer in a wind tunnel, Atmospheric Environment, 3, 197-214, (1969).

[19] http://mak.ktf-split.hr/~stipisic/mjerenje.pdf, (10^{th} September 2013).

[20] http://www.dantecdynamics.com/Default.aspx?ID=750, (10^{th} September 2013).

[21] T. Balendra, D.A. Shah, K.L. Tey, and S.K Kong, Evaluation of flow characteristics in the NUS-HDB wind tunnel , Journal of Wind Engineering and Industrial Aerodynamics, 90,, pp. 675-688, (2002).